Sequestration of Cadmium Using Stabilized Iron-based Nanoparticles and Removal of Per- and Polyfluoroalkyl Substances Using Ion Exchange Resins and Photo-regenerable Adsorbent

by

Shuting Tian

A dissertation submitted to the Graduate Faculty of
Auburn University
in partial fulfillment of the
requirements for the Degree of
Doctor of Philosophy

Auburn, Alabama
December 11, 2021

Keywords: Iron Sulfide Nanoparticles, Active Carbon, Resin, Cadmium Immobilization, PFAS, Leachate

Approved by

Dr. Dongye Zhao, Chair, Engineering Alumni Council Endowed Professor of Civil and Environmental Engineering
Dr. Mark Barnett, Professor of Civil and Environmental Engineering
Dr. Xing Fang, Arthur H. Feagin Chair Professor of Civil and Environmental Engineering
Dr. Yucheng Feng, Professor of Crop, Soil and Environmental Sciences
Dr. Brendan Higgins, Assistant Professor of Biosystems Engineering

Abstract

Over years, I have been involved in several research projects that are highly cross-disciplinary. As such, the dissertation encompasses sequestration of cadmium (Cd) in contaminated water and soil using novel stabilized nanoparticles and enhanced adsorption and photodegradation of per- and polyfluoroalkyl substances (PFAS) from water and landfill leachate using a new photo-regenerable adsorbent.

Cd is one of the most detected toxic heavy metals in the environment. In this work, we prepared a class of stabilized ferrous sulfide (FeS) nanoparticles using sodium carboxymethyl cellulose (CMC), starch, or carboxymethyl starch (CMS), as a stabilizer. The CMC-stabilized FeS nanoparticles (CMC-FeS) showed a faster adsorption rate and higher adsorption affinity and capacity than CMS- or starch-stabilized FeS nanoparticles. CMC-FeS were able to rapidly remove 93% of 1 mg/L Cd from water within 4 h at a dosage of 100 mg/L, and the material showed a maximum Langmuir sorption capacity of 497.5 mg/g at pH 7.0. In addition, CMC-FeS can be delivered into contaminated soil to facilitate *in situ* immobilization of Cd in soil. When the 58.3 mg/kg Cd-laden soil was amended with 100 mg/L CMC-FeS, the equilibrium Cd leachability based on the toxicity characteristic leaching procedure (TCLP) was reduced by 88.4%. When a CMC-FeS suspension (100 mg/L) was passed through a Cd-laden soil column at an empty bed contact time of 52.7 min, the water-leachable Cd was reduced by 98.2% after 55 pore volumes (PVs) of the treatment.

PFAS have been widely detected in aquatic systems. Yet, cost-effective technologies have been lacking due to the unique molecular structures and chemical stability of PFAS. While ion exchange resins and activated carbon have been used to remove PFAS from water, they bear with

some key limitations, including 1) conventional adsorbents are less effective for short-chain PFAS, and 2) the regeneration of spent adsorbents is difficult and costly. To address these pressing issues, we tested the effectiveness of three commercial anion exchange resins and one polymeric ligand exchanger (DOW 3N-Cu) for removal of perfluorobutanoic acid (PFBA), as a model short-chain PFAS. While the commercial strong-base anion exchange resin (IRA900) showed the best removal rate and capacity for PFBA at 100 mg/L, the weak-base resin (DOW-66) and DOW 3N-Cu offered flexibility in regeneration. A mixture of 1% NaCl and 40% CH_3OH solution was found effective for regenerating all four materials (including IRA958), with ~90% of the capacity recovered. Moreover, we employed a new adsorptive photocatalyst (Fe/TNTs@AC) to treat multiple PFAS in landfill leachate. At a dosage of 10 g/L, Fe/TNTs@AC effectively removed >95% of 13 PFAS from a model municipal landfill leachate. The effective adsorption concentrates the PFAS on a small volume of Fe/TNTs@AC, and the concentrated PFAS were then photodegraded under UV, which also regenerates the material. Following the photo-regeneration, Fe/TNTs@AC can be reused. The "concentrate-&-destroy" strategy appears promising to treat low-concentrations of PFAS in landfill leachate which has a strong matrix.

Acknowledgments

It's my honor to get the help and support of my committee members, family, and friends to finish my Ph.D. dissertation.

First and foremost, I would like to express my sincerest gratitude to my major advisor, Dr. Dongye Zhao. He is a great scientist, who has rigorous attitude, genius ideas, and diligence. He is the mentor for me. Because of his excellent guidance, inspiration, caring, patience, motivation, and encouragement through the research, I learned to be an independent and creative experimentalist. Without his lenient and patient guidance, I couldn't have my current achievements. To be a scientist like him is the goal of my life. I thank him for everything he has done for me.

I gratefully acknowledge Drs. Mark Barnett, Xing Fang, and Yucheng Feng for their serving on my dissertation committee, for their valuable advice, enlightening guidance, encouraging words, and thoughtful criticism. It has been my pleasure working with them. Sincere appreciation is also extended to Dr. Brendan Higgins, who served as the outside reader. I would like to thank Dr. Melissa Boersma for her analytical assistance, Dr. Wen Liu, Dr. Tianyuan Xu, and Dr. Zongsu Wei for their inspiration and kind supports; and thank Auburn University for providing the learning opportunity and comfortable learning and living environment. Special thanks are extended to my fellow students for their great friendship, helps, and research advices.

Finally, I would like to thank my parents for their support and encouragement throughout my life.

Table of Contents

List of Tables

List of Figures

Chapter 1. General Introduction

1.1. Cadmium contamination and treatment

Cadmium occurs naturally in the environment from processes such as erosion and abrasion of rocks and natural deposits, and from singular events such as forest fires and volcanic eruptions. The best-known cadmium mineral is greenockite (CdS). Other minerals are otavite, cadmium carbonate ($CdCO_3$) and cadmoselite (CdSe). Cadmium can also get into the environment via anthropogenic activities, such as plastic manufacturing, polymer production, electroplating, corrosion of galvanized pipes, metal refineries, pesticides, fertilizers, and waste batteries and paints (Tian et al., 2020). Therefore, Cadmium is a wide-spread element in air, water, soils, and foodstuffs.

Cadmium is one of the most detected toxic heavy metals in the environment to human, animals, and plants. Human exposure to elevated levels of Cd may result in lung, kidney, and bone damages, cardiovascular disease, obstructive pulmonary disease, and even breast cancer. Cadmium can also cause children's brain damage (Tian et al., 2020). Another important reason that cadmium gains a special concern is its non-degradable and therefore persistent characteristic (Rao et al. 2010). A well-known disaster 'Itai-Itai' was due to cadmium contaminant discharged by mining companies in the Jintsu river of Japan.

To mitigate human exposure, various regulations have been introduced at the occupational, health, and environmental levels. In the U.S., permissible exposure limit has been set at 5 $\mu g/m^3$ (8-hour time-weight average) in the workplace (ATSDR, 2012), and the reference dose in food at 1×10^{-3} mg/kg/day and that in water at 5×10^{-4} mg/kg/day (ATSDR, 2012). For environmental

standards, The US Environmental Protection Agency (EPA) has set the maximum contaminant level (MCL) of Cd in drinking water at 0.005 mg/L (EPA, 2009b).

To mitigate human exposure, the treatment or purification of effluent and Cd-contaminated water and sediment has been one of the major areas of active research. There are various methods used to treat Cd contaminants in the aqueous and solid phases. These methods can be broadly divided into the following categories: chemical methods, ion exchange, membrane, solvent extraction, and adsorption.

Adsorption has been widely employed for removing cadmium from contaminated water and wastewater because of relatively low material and operational expense, and ease of operation. A variety of adsorbents have been investigated for the removal of Cd, including Fe, Mn and/or Al nano/non-nano oxides (Ghasemi et al., 2017), carbon nanotubes (Karim et al., 2019), natural organic materials (Mahmood-ul-Hassan et al., 2015), and ion exchange resins (Naushad et al., 2019; Naushad et al., 2015). However, the Cd sorption capacity is still limited and efficient methods of *in situ* immobilization of Cd are needed.

In order to address the limitation of Cd sorption capacity, various surface modified adsorbents have been developed to enhance the sorption capacity in this dissertation. Gong et al. (2014) successfully synthesized CMC-stabilized nano FeS and found it offered 1.25 time adsorption capacity for Hg than unmodified FeS. Based on the specific properties of stabilized iron nanoparticles, the effectiveness of CMC-$Fe_3(PO_4)_2$, CMC-FeS, CMS-FeS, and starch-FeS for immobilization of Cd at environmentally relevant levels and under various environmental conditions are explored. The demand for high Cd sorption capacity and long-term stability of immobilized Cd are addressed. In addition, stabilized nanoparticles can be delivered into contaminated soil and facilitate *in situ* remediation of contaminated soil and groundwater.

Moreover, surface modification of various adsorbents may facilitate overcoming the competing effects of organic and inorganic co-solutes and enhancing the pH resistance. In this dissertation, CMC-FeS and CMS-FeS nanoparticles are selected to efficiently immobilize Cd in soil.

1.2. Per- and polyfluoroalkyl substances contamination and treatment

PFAS are a class of man-made chemicals with part or all the hydrogen atoms on the carbon bone replaced by fluorine atoms (Buck et al., 2011) or a terminal functional group (Zaggia et al., 2016). The fluorination stiffens the alkyl chains and compacts the molecules leading to the formation of a "molecular-brush" structure, which has a dense layer of trifluoromethyl groups that repels both water and oil (*i.e.*, hydro- and oleophobicity) (Zaggia et al., 2016). PFAS can be divided into two sub-groups: non-polymeric and polymeric PFAS. Within the polymeric PFAS, there are three groups: fluoropolymers; side-chain fluorinated polymers; perfluoropolyethers. Four families are involved within the non-polymeric PFAS group; they are perfluoroalkyl acids (PFAA) including but not limited to perfluoroalkyl carboxylic acids (PFCA) and perfluoroalkane sulfonic acids (PFSA), compounds derived from perfluoroalkane sulfonyl fluorides (PASF), fluorotelomers (FT), and per- and polyfluoroalkyl ethers (PFPE) (Buck et al., 2011). Perfluorooctanoic acid (PFOA, one of the PFCA) and perfluorooctane sulfonate (PFOS, one of the PFSA) are the most commonly detected PFAS in the environment.

PFAS was widely used in our daily manufactured products such as food packaging, pesticide formulations, photographic films, firefighting foams, *etc*. (Jian et al., 2018; Rahman et al., 2014). Consequently, PFAS have been widely detected in ecosystems (particularly near a specific facility such as landfill, wastewater treatment plant, or firefighter training site, and other places like outdoor dust, food, and contaminated soil/sediment (Chen et al., 2018; Clarke et al., 2010; Domingo, 2012)). For example, PFCA were reported to range from 10 to 8900 ng/L, and PFSA

were from 50 to 3200 ng/L in the U.S. landfill leachate (Wei et al., 2019). PFAS in soil amended using PFAS-contaminated sludge have been measured at 500 to 6000 μg/kg dry weight (Ghisi et al., 2019).

PFAS have been recognized as global environmental contaminants as a result of their persistency, bioaccumulation potential, and toxicity (Pereira et al., 2018). Owing to their strong and stable carbon-fluorine bonds, the human body can hardly break down PFAS. As a result, PFAS can accumulate and remain in the human body (Jian et al., 2018) and lead to various adverse health effects, such as low infant birth weight, thyroid hormone disruption, impairment on the immune system, and even cancer (EPA, 2017).

To mitigate human exposure, the U.S. Environmental Protection Agency (EPA) has established an advisory level of 70 parts per trillion (ppt) for combined PFOA and PFOS (EPA, 2017), and is currently moving towards developing enforceable MCL for major PFAS. In the meanwhile, many U.S. states have established more stringent regulations to limit PFAS in drinking water.

Conventional biological wastewater treatment processes, such as activated sludge, anaerobic digestion, and trickling filtration, are not effective in removing or degrading PFAS. Other treatment technologies have been introduced to treat PFAS, including adsorption by activated carbon (AC) and ion exchange resins, membrane filtration, chemical and electrochemical oxidation/reduction, photochemical decomposition, sonolysis, and incineration (Hori et al., 2005; Ross et al., 2018; Vecitis et al., 2008).

Sorption has been one of the most cited methods to remove PFAS from aqueous media, and to this end, various adsorbents have been investigated, including activated carbon (AC) (Franke et al., 2019), carbon nanotubes (Deng et al., 2012), ion exchange resins (Deng et al., 2010), synthetic

magnetite nanoparticles (Gong et al., 2016), and biomaterials (Chen et al., 2011). AC and anion exchange resins are the most applied adsorbents. The adsorption behavior of PFAS is strongly dependent on the length of the carbon chain that is associated with the hydrophobicity/hydrophilicity of PFAS. Other factors, e.g., adsorbent characteristics, pH, and the presence of organic and inorganic ions, can also affect PFAS treatment (Li et al., 2020a). Powder activated carbon (PAC) showed better adsorption than granular activated carbon (GAC) for PFOA (267 mg/g vs. 155 mg/g) and PFOS (453 mg/g vs. 161 mg/g) (Yu et al., 2009). Maimaiti et al. tested single-solute PFAS adsorption by IRA910. The adsorption capacities of perfluorobutanoic acid (PFBA), PFOA, PFBS, and PFOS were 636, 1437, 1023, and 1395 mg/g, respectively (Maimaiti et al., 2018). Both electrostatic and hydrophobic interactions are important in the adsorption process. Since anionic PFAS are of the most concern, a positive surface potential is desired for effective adsorption. However, current adsorption technologies for PFAS removal are facing some major challenges, including 1) the regeneration of spent adsorbents such as AC or ion exchange resins is costly and often requires organic solvents, and 2) conventional adsorbents are much less effective for adsorption of short-chain PFAS. To fill these knowledge gaps, the removal behaviors of PFBA (a short-chain PFAS) by IRA900, IRA958, DOW 66, and DOW 3N-Cu are compared, and various environmental condition impacts and regeneration recipes are studied in this dissertation.

Besides sorption, photocatalytic degradation has also received increasing interest in recent years due to its high transformation efficiency of PFAS and easier and low-energy operation under mild conditions (Cambié et al., 2016; Schneider et al., 2014; Wang et al., 2017). Modified TiO_2-based materials and non-TiO_2 catalysts (e.g., In_2O_3 and Ga_2O_3) are promising photocatalytic for degradation of PFAS, while TiO_2 is less effective (Li et al., 2020a). PFOA was degraded into

shorter chain PFAS (e.g., PFHpA, PFHxA, and PFBA) using TiO_2-multiwall carbon nanotubes (MWCNT) as a photocatalyst. The concentration of short-chain increased with time indicating that short-chain PFAS were more resistant to photocatalytic degradation. Besides, the effectiveness of photodegradation was pH-dependent (Song et al., 2012). Among non-TiO_2 catalysts, In_2O_3 nanoplates showed the highest photocatalytic activity and were able to achieve complete decomposition of PFHpA within 180 min, whereas In_2O_3 nanocubes were much less effective, indicating the strong dependence on the material shape and microstructures, which may affect the accessibility and surface orientation of the adsorbed PFAS. The concentrations of the intermediates were found to be related to their carbon chain length: PFHpA > PFHxA > PFPeA > PFBA (Li et al., 2013).

However, because PFAS are usually present at trace concentrations (µg/L or ng/L levels) in contaminated waters or leachate, it's not energy-effective to directly treat large volumes of the liquid by photodegradation. To overcome this drawback, Li et al. (2020b) developed a "Concentrate-&-Destroy" technique, which can effectively adsorb and concentrate PFAS from water on to an adsorptive photocatalyst and then degrade the pre-sorbed PFAS by subjecting the PFAS-laden solids to UV irradiation (Li et al., 2020b). The key to this technology was a new type of iron-doped, carbon-modified composite (Fe/TNTs@AC) that serves as both an adsorbent and a photocatalyst. In this dissertation, the promising technology is applied to PFAS treatment in leachate. This is the first time that modified AC can effectively sorb PFAS from leachate and is regenerated successfully in an environment friendly way.

1.3. Objectives

The overarching goal of this research was to develop and test more cost-effective technologies for removal or sequestration of heavy metals in contaminated water and soil and for adsorption and destruction of PFAS in water and landfill leachate. The overall objectives were to:

1) Prepare various stabilized iron nanoparticles (CMC-$Fe_3(PO_4)_2$, CMC-FeS, CMS-FeS, and starch-FeS) and test their Cd sorption capacities under diverse environmental conditions,
2) Investigate the effectiveness of the stabilized FeS nanoparticles for Cd immobilization (defined as reduction in solubility and leachability) in an Alabama site soil sample,
3) Test and compare the removal rates and capacities of the resins (IRA900, IRA958, DOW 66, and DOW 3N-Cu) for removal of PFBA through batch and fixed-bed column tests,
4) Explore various regeneration strategies for the different resins by comparing various regenerants (brine, methanol, mixtures of brine and organic solvent, and oil dispersants), and
5) Examine the effectiveness of Fe/TNT@AC for adsorption and subsequent photocatalytic degradation of PFAS in the leachate and optimize the treatment conditions through bench- and pilot-scale experiments.

1.4. Organization

This dissertation includes seven chapters. Except for **Chapter 1** (General Introduction) and **Chapter 7** (Conclusions and Suggestions for Future Research), each chapter of this dissertation is formatted in the journal style of Water Research.

Chapter 1 gives a general introduction of the background and the overall objectives of this dissertation. **Chapter 2** describes the synthesis and testing of CMC-stabilized $Fe_3(PO_4)_2$ nanoparticles, and presents the results and discussion on the removal of aqueous Cd as a function

of material dosage, CMC concentration, reaction time, pH, and HA. **Chapter 3** describes the synthesis and testing of CMC-stabilized FeS nanoparticles, and presents results and discussion on the removal of aqueous Cd as a function of material dosage, CMC concentration, reaction time, pH, and HA. Besides, dissolved oxygen effect and long-term stability of immobilized Cd. This chapter is based on the information that has been published in *Science of the Total Environment* (Tian et al., 2020). **Chapter 4** investigates the effects of different stabilizers on the immobilization of Cd in aqueous and solid phases by stabilized FeS nanoparticles. **Chapter 5** compares various ion exchange resins (IRA900, IRA958, DOW 66, and DOW 3N-Cu) for the removal of PFBA contaminated water and informs the removal mechanisms and regeneration efficiency. **Chapter 6** presents a new "concentrate-&-destroy" strategy using a photo-regenerable adsorbent (Fe/TNTs@AC) for enhanced adsorption and photocatalytic degradation of PFAS in water and landfill leachate. This chapter is based on the information that has been published in *Science of the Total Environment* (Tian et al., 2021). **Chapter 7** gives a summary of major conclusions and some recommendations for future work.

Chapter 2. Enhanced Removal of Cadmium from Water by Stabilized Iron Phosphate Nanoparticles

Sodium carboxymethyl cellulose (CMC) stabilized iron phosphate ($Fe_3(PO_4)_2$) nanoparticles were prepared by modifying an aqueous precipitation approach and in the presence of CMC as a stabilizer. Effects of CMC concentration, initial Cd concentration, pH, co-existing ions, and humic acid (HA) were examined. Fully stabilized $Fe_3(PO_4)_2$ (426 mg/L) nanoparticles were obtained using 0.1 wt.% CMC. Batch kinetic test results showed that 0.1 wt.% CMC-stabilized nanoparticles removed 87.6% of Cd (C_0 = 1 mg/L) within 11 h at pH 7.0. The Cd removal efficiency was 11.6% higher than that of non-stabilized nanoparticles. Pseudo-second-order rate model can well describe the Cd adsorption kinetics with a rate constant of 12.25 $g \cdot mg^{-1} \cdot hr^{-1}$. Sorption isotherm was well simulated by the Langmuir isotherm model with a maximum Langmuir sorption capacity of 36.1 mg/g at pH 7.0. Increasing pH from 4.0 to 8.0 enhanced the Cd removal rate from 55.1% to 96.3%, while the presence of 10 mg/L HA (as total organic carbon) lowered the Cd adsorption by 5.7%. The addition of 10 mM $NaNO_3$ suppressed the Cd removal by 7.4%, while the addition of 10 mM NaCl and $NaHCO_3$ improved Cd uptake by 1.4% and 4.9%, respectively. Fourier transform infrared (FTIR) spectroscopy suggested surface complexation between Cd and $Fe_3(PO_4)_2$ was the predominant mechanism for Cd immobilization.

2.1. Introduction

Cadmium (Cd) is known to be a widespread environmental contaminant and toxic for living organisms even if it is present at low levels. It has been classified as a human carcinogen and teratogen impacting the lungs, liver, and kidney. The natural source of Cd is the erosion of rocks and natural deposits, e.g., greenockite and otavite. The anthropogenic sources are plastic

manufacturing, polymer production, electroplating, corrosion of galvanized pipes, metal refineries, pesticides, fertilizers, and waste batteries and paints (ATSDR, 2008). In order to protect human health and environment, regulations are set up and various methods are applied to treat Cd contaminants. For example, the maximum contaminant level (MCL) of Cd in drinking water is 0.005 mg/L (EPA, 2009b), the reference dose for human exposure in food is 1×10^{-3} mg/kg/day and in water is 5×10^{-4} mg/kg/day (ATSDR, 2012), and *etc*. Treatment methods are adsorption, precipitation, ion exchange, electrocoagulation, electrodialysis, solvent extraction, *etc.* (Bailey et al., 1999).

Among all the methods, adsorption draws the most attention because of low operation cost and easy handling. A variety of adsorbents have been investigated for removal of Cd, including metal oxides (e.g., Fe, Mn and/or Al oxides) (Dong et al., 2000), carbon nanotubes (Li et al., 2003), natural organic materials (e.g. algae (Yu et al., 2001) and carbonized coir pith (Kadirvelu and Namasivayam, 2003)), resins (Naushad et al., 2015; Naushad et al., 2019), and fly ash (Ayala et al., 1998). Considering the affinity of Fe to Cd and the high affinity and stability of the combination of phosphate and Cd (Xue et al., 2018a), as well as the extensive use of phosphate adsorbents in water treatment (Pan et al., 2007), $Fe_3(PO_4)_2$ was selected as a sorbent to remove Cd. However, natural or conventionally prepared $Fe_3(PO_4)_2$ particles tend to form large aggregates rapidly into the millimeter or larger scale, limiting their sorption capacity and soil deliverability. For instance, Zhang et al. (2021a) prepared iron phosphate-modified pollen microspheres (pollen@$FePO_4$) and had a maximum Cd adsorption capacity of 4.623 mg/g.

Stabilized materials are in nanoscale which are expected to offer much higher sorption capacity due to their larger specific surface area, more active sorption sites, and higher surface reactivity. Xiong et al. (2009) and Gong et al. (2014) developed a “green” technique for preparing

a new class of stabilized nanoparticles using sodium carboxymethyl cellulose (CMC) as a stabilizer. Gong et al. (2014) prepared both stabilized FeS nanoparticles (CMC-FeS) and bare FeS particles. The results showed that CMC-FeS enhanced the maximum sorption capacity for mercury by 20% compared to bare FeS particles. Furthermore, the stabilized nanoparticles can be delivered into soil/sediment in a controllable manner. Qiao et al. (2017) successfully synthesized biochar-supported iron phosphate nanoparticle stabilized by CMC and effectively immobilized Cd in soil. Therefore, CMC stabilized $Fe_3(PO_4)_2$ particles were synthesized and used to treat Cd contamination in aqueous phase.

The overall goal of this study is to evaluate the effectiveness of CMC-$Fe_3(PO_4)_2$ for Cd removal from aqueous solution and study the underlying mechanisms. The specific objectives are to: (1) prepare CMC-stabilized iron phosphate nanoparticles at various CMC-to-$Fe_3(PO_4)_2$ molar ratios and test their Cd sorption capacity; (2) examine the effects of the stabilizer concentration, initial Cd concentration, pH, co-existing ions and humic acid (HA) on the Cd removal through batch kinetic and equilibrium experiments, and (3) elucidate the underlying Cd removal mechanisms through material characterization such as Fourier transform infrared (FTIR) spectroscopy and X-ray powder diffraction (XRD) analyses.

2.2. Materials and methods

2.2.1. Chemicals

All chemicals used in this study were in the analytical grade or higher. Iron sulfate heptahydrate ($FeSO_4 \cdot 7H_2O$), cadmium chloride ($CdCl_2$), and CMC (MW = 90 000 in the sodium form, degree of substitute = 0.7) were purchased from Acros Organics (Pittsburgh, PA, USA). The Suwannee River Humic Acid was obtained from the International Humic Substances Society (IHSS, Georgia Tech, Atlanta, GA, USA). According to the supplier, the HA contained water

(8.15%), ash (7.0%), C (52.47%), H (4.19%), O (42.69%), N (1.10%), S (0.65%), and P (0.02%) (all by weight). Disodium hydrogen phosphate heptahydrate ($Na_2HPO_4 \cdot 7H_2O$), sodium hydroxide (NaOH), and hydrochloric acid (HCl) were obtained from VWR International (Radnor, PA, USA). Solutions were prepared with deionized (DI) water (18 MX cm) from the Milli-QTM Water System.

2.2.2. Preparation and characterization of CMC-$Fe_3(PO_4)_2$ nanoparticles

A 150 mL suspension of CMC-$Fe_3(PO_4)_2$ nanoparticles was prepared in a 250 mL glass bottle following the previously reported procedure (Tian et al., 2020; Xiong et al., 2009). The molar ratio of Fe^{2+} and PO_4^{3-} introduced to the solution was 3:2 based on the stoichiometry of **Eq. 2-1** (Liu and Zhao, 2007a).

$$3Fe^{2+} + 2PO_4^{3-} + 8H_2O \rightarrow Fe_3(PO_4)_2 \cdot 8H_2O \qquad \log K = 37.8 \qquad (\mathbf{2\text{-}1})$$

In brief, first, a 1 wt.% CMC stock solution was prepared. Then, 15 mL of the stock solution was added into 85 mL deionized (DI) water, and the mixture was purged with purified N_2 (>99%) for 15 min to remove dissolved oxygen (DO). Meanwhile, solutions of 26.8 mM $FeSO_4$ (20 mL) and 26.8 mM Na_2HPO_4 (30 mL) were prepared with N_2-purged DI water. Under N_2 purging, the $FeSO_4$ solution (20 mL) was added to the CMC solution to yield a solution with 3.6 mM of Fe^{2+} and 1.3×10^{-1} wt.% of CMC. The mixture was then purged with N_2 for 5 min to assure complete mixing and formation of Fe^{2+}–CMC complexes. Then, the Na_2HPO_4 (30 mL) was introduced into the solution with N_2 purged at an Fe-to-PO_4 molar ratio of 2:3. To ensure complete reaction, the system was continually purged N_2 for another 5 min. The resultant nanoparticle suspension contained 426 mg/L $Fe_3(PO_4)_2$ and 0.1 wt.% of CMC. For comparison, bare $Fe_3(PO_4)_2$ particles were prepared in the absence of CMC but under otherwise identical conditions. The particles were then sealed and aged for 24 h before use.

Transmission electron microscopy (TEM) analysis was carried out using a Zeiss EM10 transmission electron microscope (Zeiss, Thornwood, NJ, USA) operated at 60 kV. A 10 μL aqueous sample was placed on a formvar-carbon-coated copper grid (Electron Microscopy Sciences, Hatfield, PA, USA), allowing for full contact/spreading on the grid, followed by vacuum drying for 12 h. The particles attached to the grid were then imaged. The nanoparticles were collected by filtering the suspensions using a 25 nm membrane filter of mixed cellulose esters (Millipore Corp., Billerica, MA, USA), which was able to completely remove the nanoparticles but did not retain soluble Cd. The solids were then rinsed three times with N_2-purged DI water, and subsequently freeze-dried under vacuum at −50 °C using a VirTis freeze mobile freeze-dryer (Gardiner, NY, USA) for 48 h. Fourier transform infrared (FTIR) spectroscopy measurements of the freeze-dried samples were carried out using a SHIMADZU IR Prestige-21 spectrometer (Shimadzu Scientific Instruments, Columbia, MD, USA) to explore the interactions between $Fe_3(PO_4)_2$ and CMC, and between Cd and CMC-$Fe_3(PO_4)_2$. The freeze-dried Cd-laden CMC-$Fe_3(PO_4)_2$ samples were mixed with KBr powder to form thin KBr pellets consisting of 2 wt.% of the nanoparticles. A pure KBr pellet was used as a background to obtain the net FTIR spectra of the samples. For comparison, FTIR spectra for Cd-free CMC-$Fe_3(PO_4)_2$ particles and neat CMC were also acquired in the same manner. Dynamic light scattering (DLS) tests of the $Fe_3(PO_4)_2$ particles were performed with a Malvern Zetasizer Nano ZS (Malvern Instruments, Worcestershire, UK) to yield number-weighted particle size distributions and zeta potentials. Solution viscosities were measured with a Gilmont falling-ball viscometer (Barnant Company, Barrington, IL, USA) and then used to correct for the influence of viscosity on the DLS measurements. All measurements were conducted in duplicate, and data were reported as mean ± relative deviation from the mean.

2.2.3. Effects of CMC concentration on cadmium uptake by $Fe_3(PO_4)_2$

$Fe_3(PO_4)_2$ particles were prepared at a fixed $Fe_3(PO_4)_2$ concentration of 426 mg/L as $Fe_3(PO_4)_2$ and at various concentrations of CMC, namely, at CMC-to-$Fe_3(PO_4)_2$ molar ratios of 0, 2.8×10^{-4}, 7.8×10^{-4}, 1.6×10^{-3}, 3.1×10^{-3}, 7.8×10^{-3}, 9.3×10^{-3}, and 1.2×10^{-2}. The solution pH was kept at 7.00 ± 0.20 in all cases. To examine the effects of CMC on cadmium removal by $Fe_3(PO_4)_2$, sorption tests were carried out following the procedures as described in **Section 2.2.4** with a reaction time of 48 h. In order to get fully stabilized suspension, the physical stability of $Fe_3(PO_4)_2$ particles were examined. The $Fe_3(PO_4)_2$ suspensions were allowed to age for 24 h and settle under gravity, and then 1 mL of the top supernatant was sampled and mixed with 4 mL of 12 M HCl for 5 min to completely dissolve the nanoparticles, and then analyzed for total Fe. Both Fe and Cd were measured by ICP-OES 710-ES (Agilent Technologies, Santa Clara, CA, USA) with detection limits of 1 μg/L and 0.1 μg/L, respectively.

2.2.4. Cadmium sorption kinetic tests

Batch Cd sorption kinetic experiments were carried out in 50 mL Teflon vials under anoxic conditions. The reaction conditions were as follows: initial Cd concentration = 1 mg/L, $Fe_3(PO_4)_2$ = 426 mg/L, and pH = 7.00 ± 0.20 (maintained with HCl and/or NaOH). The mixtures were sealed and continuously mixed on an end-over-end rotator operated at 50 rpm at room temperature (20 ± 1 °C). The samples were taken at predetermined times and then filtered through the 25 nm membrane filters and analyzed for Cd concentration in the filtrates. Control tests showed that loss of cadmium during the sorption and sample filtration was <2% in all cases.

2.2.5. Cadmium sorption isotherms and effects of pH

Cd sorption isotherms by CMC-$Fe_3(PO_4)_2$ were constructed following similar procedures to the kinetic tests where the systems were equilibrated for 48 h. The experimental conditions were:

$Fe_3(PO_4)_2$ = 426 mg/L, CMC-to-$Fe_3(PO_4)_2$ molar ratio = 3.1×10^{-3}, initial Cd^{2+} = 0.6-25 mg/L, and pH = 7.00 ± 0.20. The equilibrium cadmium uptake was calculated based on differences between the initial and final concentrations of Cd in the aqueous phase. To test the pH effects on the Cd sorption, the sorption isotherms were also obtained at equilibrium pH values ranging from 4.0 to 8.0.

2.2.6. Effects of HA and co-existing ions

Batch Cd sorption equilibrium tests were conducted in 50 mL Teflon vials to investigate the effects of HA and co-existing ions. Each vial was loaded with 426 mg/L of CMC-$Fe_3(PO_4)_2$ and 1 mg/L of Cd^{2+}, and equilibrated for 48 h at a constant pH of 7.00 ± 0.20. To probe the HA effect, the tests were conducted in the presence of various concentrations of HA (1 to 10 mg/L as total organic carbon (TOC)). TOC was analyzed using a Tekmar Dohrmann Phoenix 8000 UV Persulfate TOC Analyzer (Mason, OH, USA) with a detection limit of 2 μg/L. To investigate effects of co-existing ions, the sorption tests were carried out in the presence of various concentrations of NaCl (0-10 mM), $NaNO_3$ (0-10 mM), or $NaHCO_3$ (0-10 mM).

2.3. Results and discussion

2.3.1. Characterization of CMC-stabilized $Fe_3(PO_4)_2$ nanoparticles

Fig. 2-1 shows the TEM image of CMC-stabilized $Fe_3(PO_4)_2$ nanoparticles prepared at a CMC-to-$Fe_3(PO_4)_2$ molar ratio of 3.1×10^{-3}. The particles were rather poly-dispersed with a size range from 90.54 nm to 203.12 nm and with a mean particle size of 167.46 ± 28.79 nm. At the experimental pH of 7.0, CMC was negatively charged (pK_a of CMC = 4.3), resulting in a zeta potential of -41.2 mV for CMC-$Fe_3(PO_4)_2$. CMC stabilized the nanoparticles through concurrent electrostatic repulsion and steric hinderance (He and Zhao, 2007). **Fig. 2-1** clearly shows that $Fe_3(PO_4)_2$ particles have a sphere structure and do not aggregate. Nanoscale particles have higher

surface area and more abundant adsorption sites, which can lead to higher cadmium adsorption efficiency (Zhang et al., 2021b).

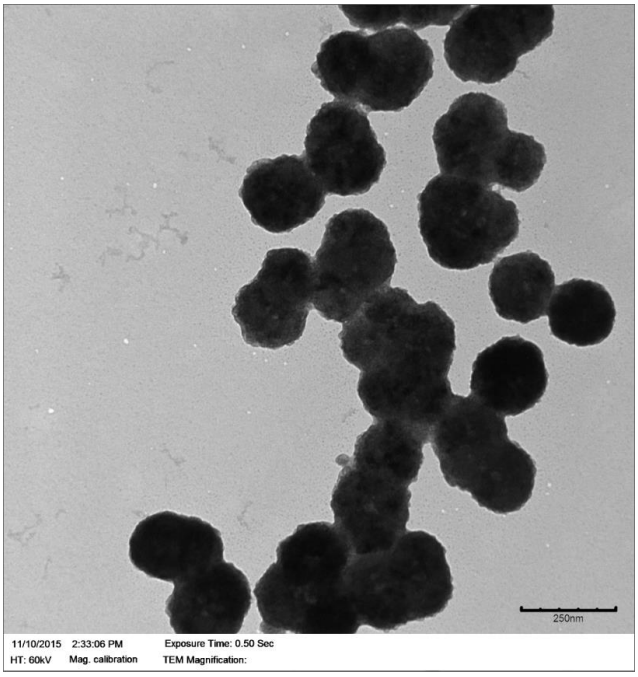

Fig. 2-1. TEM image of CMC-stabilized $Fe_3(PO_4)_2$ nanoparticles. $Fe_3(PO_4)_2$ = 426 mg/L, and CMC-to-$Fe_3(PO_4)_2$ molar ratio = 3.1×10^{-3}.

Liu et al. (2007a) synthesized CMC-stabilized $Fe_3(PO_4)_2$ nanoparticles in the same manner and the $Fe_3(PO_4)_2$ phase was confirmed by the X-ray diffractogram. It had XRD peak positions at 11.2° (d = 7.93 nm), 13.2° (d = 6.73 nm), 18.1° (d = 4.90 nm), 21.8° (d = 4.08 nm), 27.8° (d = 3.21 nm), 29.9° (d = 29.9 nm), 30.2° (d = 2.96 nm) and 32.8° (d = 2.73 nm), which were consistent with the standard XRD pattern for $Fe_3(PO_4)_2$ (Mindat).

Fig. 2-2 presents the FTIR spectra of neat CMC, CMC-$Fe_3(PO_4)_2$, and Cd-laden CMC-$Fe_3(PO_4)_2$. Four strong peaks were observed for CMC-$Fe_3(PO_4)_2$ at the wavenumbers of 3423, 1638, 1053, and 592 cm^{-1}, which are attributed to interactions between Fe^{2+} and COO^- (1638 cm^{-1})

or −OH groups (3423 and 1053 cm^{-1}) (He et al., 2007), and Fe−O vibration (592 cm^{-1}) (Ahangaran et al., 2013). The much stronger COO^- and −OH stretching band for CMC-$Fe_3(PO_4)_2$ compared to neat CMC indicates that CMC-$Fe_3(PO_4)_2$ has larger dipole moment which is due to the surface complexation between CMC and $Fe_3(PO_4)_2$ (Academy). The band observed at 2884 cm^{-1} for neat CMC indicates the C−H stretching vibration from the CH_2 groups of the stabilizer (Maity and Agrawal, 2007). The bands at 1587, 1412, and 1018 cm^{-1} for neat CMC are ascribed to asymmetric and symmetric vibrations of COO^- groups and C−O stretching (RCH_2OH) (Brown et al., 1988). For CMC-$Fe_3(PO_4)_2$, the wavenumber separation (Δ) between the asymmetric $\upsilon_{as}(COO^-)$ (1638 cm^{-1}) and symmetric $\upsilon_s(COO^-)$ (1385 cm^{-1}) stretches is 253 cm^{-1}, suggesting that the primary mechanism for binding CMC to $Fe_3(PO_4)_2$ is bidentate bridging (He et al., 2007). Upon Cd^{2+} uptake, the FTIR spectra showed similar absorption band characteristics, namely, −OH group (3396 cm^{-1}), asymmetric and symmetric stretches of COO^- groups (1632 and 1384 cm^{-1}), C−O stretching (RCH_2OH) (1057 cm^{-1}), and Fe−O bond (598 cm^{-1}). Yet, the −OH stretching band shifted from 3423 cm^{-1} for CMC-$Fe_3(PO_4)_2$ to 3396 cm^{-1} for Cd-laden CMC-$Fe_3(PO_4)_2$ and the asymmetric and symmetric stretches of COO^- shifted from 1638 and 1632 cm^{-1} to 1385 and 1384 cm^{-1}, respectively. It indicates that the bonding is enhanced upon Cd^{2+} uptake (Sylvestre et al., 2004). All these changes suggest that surface complexation between CMC-$Fe_3(PO_4)_2$ and Cd was involved, where Cd acts as the Lewis acid.

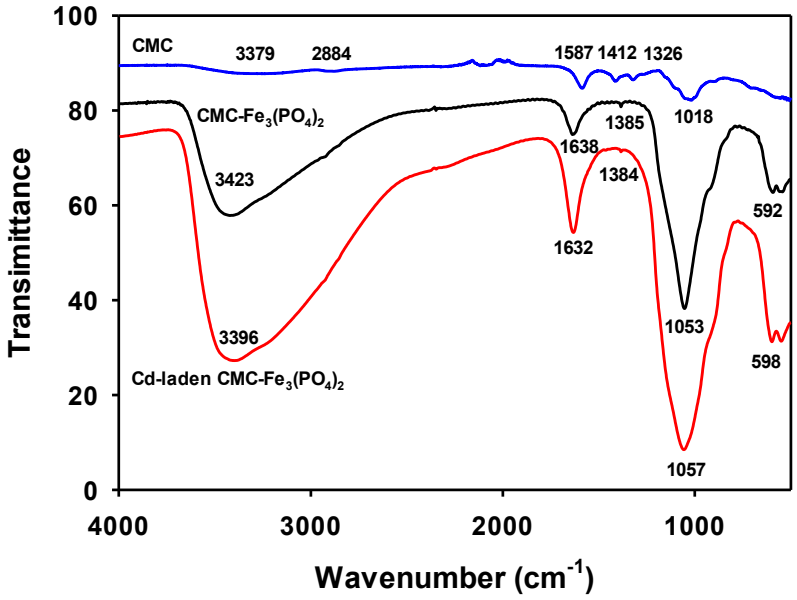

Fig. 2-2. FTIR spectra of neat CMC powder, CMC-$Fe_3(PO_4)_2$ nanoparticles, and Cd-laden CMC-$Fe_3(PO_4)_2$. CMC-$Fe_3(PO_4)_2$ preparation: $Fe_3(PO_4)_2$ = 1 g/L, CMC-to-$Fe_3(PO_4)_2$ molar ratio = 3.1×10^{-3}, and solution pH = 7.00 ± 0.20; Cd-laden CMC-$Fe_3(PO_4)_2$ was prepared by equilibrating the same CMC-$Fe_3(PO_4)_2$ with 25 mg/L of Cd^{2+}.

2.3.2. Effects of CMC concentration on cadmium uptake by $Fe_3(PO_4)_2$

Fig. 2-3 shows the effect of the stabilizer concentration on the equilibrium uptake of Cd^{2+} by $Fe_3(PO_4)_2$ particles. The Cd^{2+} removal increased from 69.1% to 90.8% when the CMC-to-$Fe_3(PO_4)_2$ molar ratio was increased from 0 to 7.8×10^{-3}, with the maximum removal occurred at CMC-to-$Fe_3(PO_4)_2$ molar ratios of 3.1×10^{-3}–9.3×10^{-3}. Evidently, increasing CMC concentration resulted in smaller $Fe_3(PO_4)_2$ particles (**Fig. 2-1** and the DLS size decreased from 1423 nm to 241 nm), and therefore, greater surface area and more sorption sites. However, further increasing the CMC-to-$Fe_3(PO_4)_2$ molar ratio above 1.2×10^{-2} resulted in a slight but significant decrease in Cd

removal (Based on the *t*-tests, the *p* value was 2.4×10^{-5} which was statistically significant at $p < 0.05$). For instance, Cd^{2+} uptake was reduced by 9.2% when the CMC-$Fe_3(PO_4)_2$ ratio was elevated from 7.8×10^{-3} to 1.2×10^{-2}. The inhibition can be attributed to the excessive uptake of CMC molecules on the particle surface, resulting in a denser CMC coating on the nanoparticles, which may inhibit access of Cd to the particles' surface sites due to elevated mass transfer resistance and/or blockage of the sorption sites (He and Zhao, 2008); on the other hand, complexation of soluble CMC with Cd^{2+} may prevent sorption of Cd^{2+} on the particle surface.

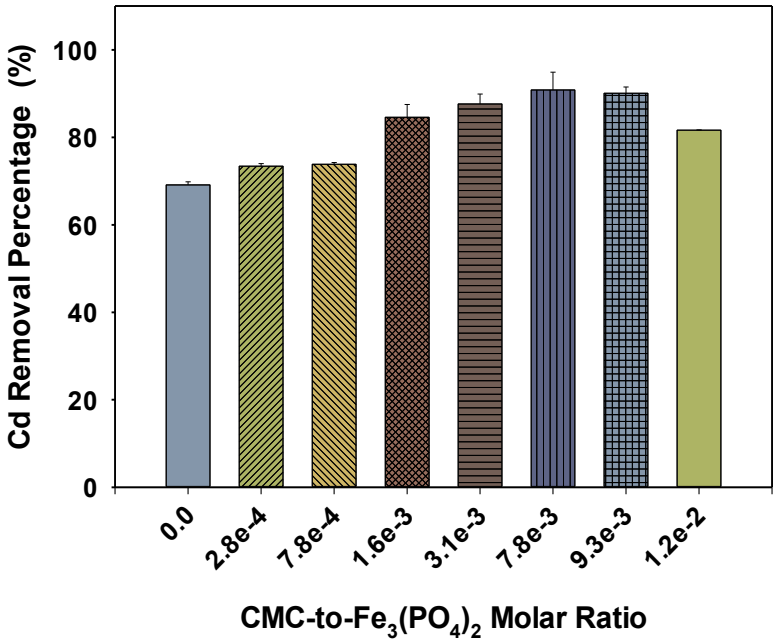

Fig. 2-3. Equilibrium cadmium removal by $Fe_3(PO_4)_2$ particles prepared at various CMC-to-$Fe_3(PO_4)_2$ molar ratios. Initial Cd^{2+} = 1 mg/L, $Fe_3(PO_4)_2$ = 426 mg/L, equilibrium pH = 7.00 ± 0.20, and equilibration time = 48 h.

Particle stability measurements indicated that complete particle stabilization was achieved at a CMC-to-$Fe_3(PO_4)_2$ molar ratio of 3.1×10^{-3}, i.e., 100% of CMC-$Fe_3(PO_4)_2$ nanoparticles

remained suspended after 24 h gravity settling. In contrast, only 1.6% of non-stabilized $Fe_3(PO_4)_2$ particles were detected in the top supernatant.

Considering Cd uptake capacity, physical stability, and the goal of this study was to find a cheaper, more efficient and environment friendly adsorbent to treat Cd contamination, CMC-$Fe_3(PO_4)_2$ prepared at the CMC-to-$Fe_3(PO_4)_2$ molar ratio of 3.1×10^{-3} was considered optimal, and thus, was further tested in the subsequent experiments.

2.3.3. Sorption kinetics of Cd by CMC-$Fe_3(PO_4)_2$

Fig. 2-4a shows Cd^{2+} removal kinetics by bare $Fe_3(PO_4)_2$ and CMC-$Fe_3(PO_4)_2$. 82.2% and 70.4% of equilibrium capacity was achieved in the first 1.3 h by CMC-$Fe_3(PO_4)_2$ and bare $Fe_3(PO_4)_2$ particles, respectively. Both have rapid initial rate. A gradual phase is followed till equilibrium at ~11 h for both CMC-$Fe_3(PO_4)_2$ and bare $Fe_3(PO_4)_2$, which is consistent with the common notion that more accessible sites are occupied first (Axe and Anderson, 1995). At equilibrium, 87.6% of Cd was removed by CMC-$Fe_3(PO_4)_2$, compared to 76.0% for bare $Fe_3(PO_4)_2$. The faster removal rate and higher removal capacity of CMC-$Fe_3(PO_4)_2$ can be attributed to the smaller particle size and larger specific surface area of the nanoparticles. The commonly used pseudo-second-order kinetic model was able to simulate the kinetic data (**Fig. 2-4b**):

$$\frac{dq_t}{dt} = k_2(q_e - q_t)^2 \quad (\mathbf{2\text{-}2})$$

Integrate **Eq. 2-2** for the boundary conditions (t = 0, q_t = 0 and t = t, q_e = q_t) gives the **Eq. 2-3** below:

$$q_t = \frac{q_e t}{\frac{1}{k_2 q_e} + t} \quad (\mathbf{2\text{-}3})$$

where q_e and q_t are the amount of adsorbed Cd on the $Fe_3(PO_4)_2$ particles (mg/g) at equilibrium and time t (h), respectively, and k_2 is the rate constant. For comparison, the pseudo-

first-order model was also teste-fitted (not shown in figure). The expression of the pseudo-first-order model is:

$$\frac{dq_t}{dt} = k_1(q_e - q_t) \quad \textbf{(2-4)}$$

Integrating **Eq. 2-4** for the boundary conditions (t = 0, q_t = 0 and t = t, q_e = q_t) leads to the formula below (Moussout et al., 2018):

$$q_t = q_e[1 - \exp(-k_1 t)] \quad \textbf{(2-5)}$$

where q_e and q_t are the amount of adsorbed Cd on the $Fe_3(PO_4)_2$ particles (mg/g) at equilibrium and time t (h), respectively, and k_1 is the rate constant. **Table 2-1** gives the best-fitted kinetic model parameters. For both bare $Fe_3(PO_4)_2$ and CMC-$Fe_3(PO_4)_2$, the pseudo-second-order kinetic model provided better data fitting (R^2 = 0.9954 for bare $Fe_3(PO_4)_2$ and 0.9866 for CMC-$Fe_3(PO_4)_2$) than the pseudo-first-order model (R^2 = 0.9778 and 0.9593, respectively). The k_2 values were 2.67 g·mg^{-1}·hr^{-1} for bare $Fe_3(PO_4)_2$ and 12.25 g·mg^{-1}·hr^{-1} for CMC-$Fe_3(PO_4)_2$, confirming the much faster Cd removal rate of CMC-$Fe_3(PO_4)_2$.

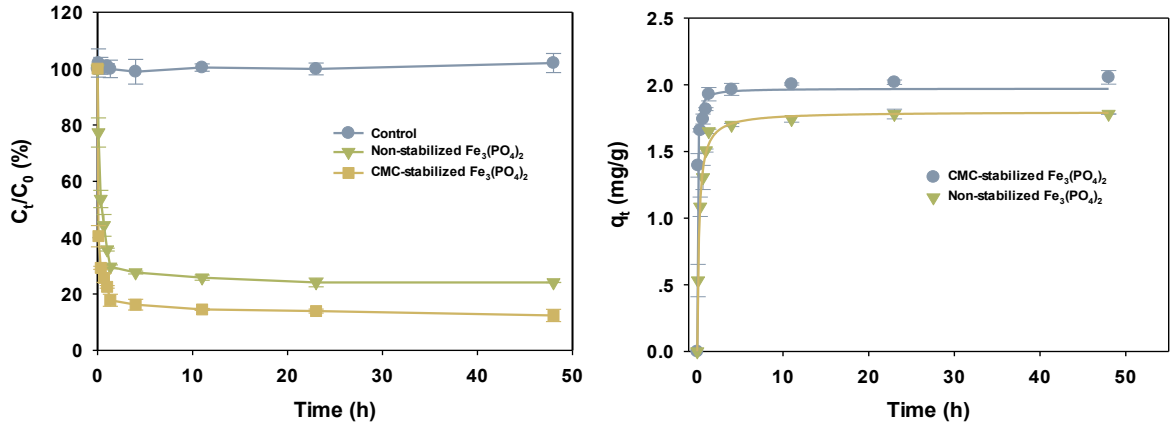

(a) (b)

Fig. 2-4. (a) Cd^{2+} sorption kinetics using bare and CMC-stabilized $Fe_3(PO_4)_2$ particles and (b) pseudo-second-order kinetic fittings of Cd^{2+} sorption. Initial Cd^{2+} = 1 mg/L, $Fe_3(PO_4)_2$ = 426 mg/L, CMC-to-$Fe_3(PO_4)_2$ = 3.1×10^{-3} for CMC-$Fe_3(PO_4)_2$ particles, and pH = 7.00 ± 0.20.

Table 2-1. Best fitted kinetic parameters with various kinetic models applied for simulating the sorption kinetics of cadmium removal by bare or CMC-stabilized $Fe_3(PO_4)_2$ particles (errors given as standard deviation).

Kinetic Models	**Governing Equation**	**Parameters**		
			Non-stabilized $Fe_3(PO_4)_2$	**CMC-$Fe_3(PO_4)_2$**
Pseudo-first-order kinetic model	$q_t = q_e[1 - \exp(-k_1 t)]$	q_e (mg/g)	1.72 ± 0.04	1.90 ± 0.05
		k_1 (hr^{-1})	2.71 ± 0.33	15.40 ± 3.12
		R^2	0.9778	0.9593
Pseudo-second-order kinetic model	$q_t = \frac{q_e t}{\frac{1}{k_2 q_e} + t}$	q_e (mg/g)	1.80 ± 0.02	1.97 ± 0.03
		k_2 ($g \cdot mg^{-1} \cdot hr^{-1}$)	0.21 ± 0.02	0.04 ± 0.01
		R^2	0.9954	0.9866

Note: q_e is the amount of sorbed Cd (mg/g) at equilibrium.

q_e and q_t are the calculated amount of sorbed Cd (mg/g) at equilibrium and time t (h), respectively.

k_1 and k_2 are the rate constants of pseudo-first-order and pseudo-second-order kinetic models.

R^2: correlation coefficient, which is calculated per the equation $R^2 = 1 - \frac{\sum_i (y_i - y_{i(predict)})^2}{\sum_i (y_i - \bar{y})^2}$,

where y_i and $y_{i(predict)}$ are the original data values and model values, respectively, and $\bar{y}$ is the mean of the observed data.

2.3.4. Sorption isotherms

Sorption isotherms of Cd onto CMC-$Fe_3(PO_4)_2$ were carried out in the pH range of 4-8 (**Fig. 2-5**). It was evident that the Cd uptake was enhanced with increasing solution pH. The classical Langmuir and Freundlich models (**Eq. 2-6** and **2-7**) were employed to fit the isotherm data (**Fig. 2-5**):

$$\text{Langmuir model: } q_e = \frac{bQC_e}{1+bC_e} \quad (\mathbf{2\text{-}6})$$

$$\text{Freundlich model: } q_e = KC_e^{\frac{1}{n}} \quad (\mathbf{2\text{-}7})$$

where q_e represents the cadmium uptake (mg/g), C_e is the equilibrium concentration of cadmium in the solution phase (mg/L), Q is the Langmuir maximum sorption capacity (mg/g), b is the Langmuir affinity constant (L/mg) related to the adsorption energy, K is the Freundlich constant related to adsorption capacity, n is the heterogeneity factor indicating the adsorption intensity of the adsorbate. **Table 2-2** summarizes the resulting fitting results. Clearly, the Langmuir model fit the data better with $R^2 = 0.9968$ than the Freundlich model with $R^2 = 0.9793$. In this case, the Langmuir model suggests that it is the mono-layer adsorption which because of surface complexation or ionic binding (Gong et al., 2014). The maximum adsorption capacities of Cd by CMC-$Fe_3(PO_4)_2$ were 3.6 mg/g, 8.8 mg/g, 29.5 mg/g, 36.1 mg/g, and 33.2 mg/g at pH of 4.0, 5.0, 6.0, 7.0, and 8.0, respectively. These capacity values are much higher than bare $Fe_3(PO_4)_2$ and other $Fe_3(PO_4)_2$ work, e.g. iron phosphate-modified pollen microspheres (pollen@$FePO_4$) which had a maximum Cd adsorption capacity of 4.623 mg/g (Zhang et al., 2021a). As pH increased from 4.0 to 7.0, the maximum sorption capacity rosed sharply from 3.6 to 36.1 mg/g. The predominant cadmium species in the pH range is Cd^{2+} (K_{sp} of $Cd(OH)_2$ is 2×10^{-14}). The declined Cd removal at lower pH can be attributed to several factors. First, more of the CMC-$Fe_3(PO_4)_2$ nanoparticles

were dissolved at lower pH, and thus partial loss of the binding sites. 53.5% of $Fe_3(PO_4)_2$ was dissolved at pH 4.0, and the percentage was decreased to ≤1.7% at pH ≥ 7. Second, higher pH was favorable for foramtion of $Cd_3(PO_4)_2OH$ precipitation (K_{sp} = $10^{-42.5}$). At alkaline, both chemical precipitation and surface adsorption became important mechanisms, where more $Cd_3(PO_4)_2OH$(s) was formed at higher pH. Third, the increase of pH rendered more negatively charged surface of CMC-$Fe_3(PO_4)_2$, resulting in smaller paticles, larger specific area, and more favorable interactions with the Cd^{2+} cations (Jain et al., 2018). In fact, as pH increased from 4.0 to 8.0, the zeta potential of CMC-$Fe_3(PO_4)_2$ was more negative charged from -27 to -41.5 mV, and the DLS-based particle size decreased from 300.2 to 228.0 nm. In addition, the Ostwald ripening process was more likely operative at lower pH, namely, smaller particles dissolved and redeposited onto larger particles, resulting in fewer but larger particles.

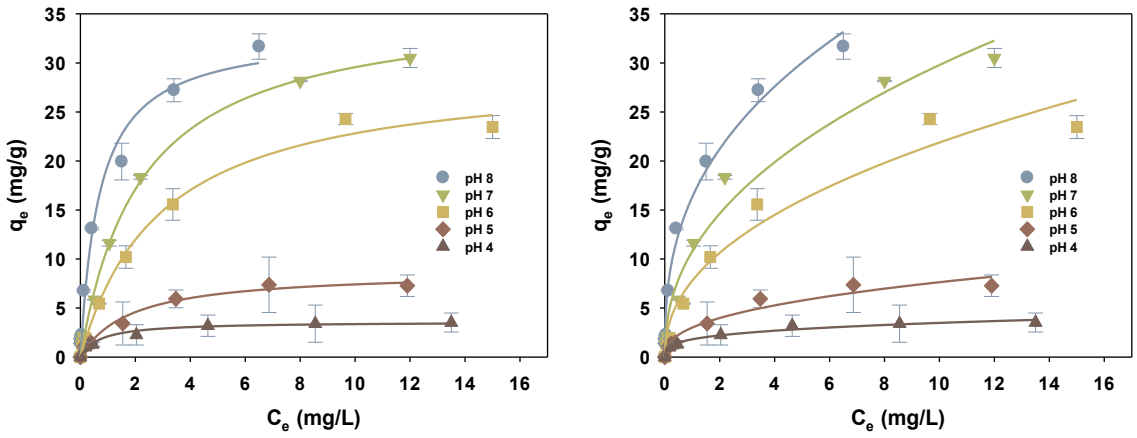

(a) (b)

Fig. 2-5. Cadmium sorption isotherms fitted with (a) Langmuir model and (b) Freundlich model for CMC-$Fe_3(PO_4)_2$ nanoparticles. $Fe_3(PO_4)_2$ = 426 mg/L, CMC-to-$Fe_3(PO_4)_2$ = 3.1 × 10^{-3}, initial Cd concentration = 0.06-25 mg/L, pH = 4.0-8.0 (final), and equilibration time = 48 h.

Table 2-2. Langmuir and Freundlich isotherm model parameters for the sorption of cadmium by CMC-stabilized $Fe_3(PO_4)_2$ nanoparticles at pH 4 to 8 (errors given as standard deviation).

Sorption Isotherm Model	Governing Equation	Parameters					
		pH	**4**	**5**	**6**	**7**	**8**
Langmuir	$q_e = \frac{bQC_e}{1+bC_e}$	Q (mg/g)	3.60 ± 0.18	8.76 ± 0.55	29.50 ± 1.30	36.13 ± 1.02	33.19 ± 1.92
		b (L/mg)	1.42 ± 0.25	0.55 ± 0.09	0.34 ± 0.04	0.45 ± 0.04	1.44 ± 0.26
		R^2	0.9726	0.9838	0.9928	0.9968	0.9833
Freundlich	$q_e = KC_e^{\frac{1}{n}}$	K	1.81 ± 0.10	3.01 ± 0.34	7.79 ± 0.94	10.79 ± 0.91	16.34 ± 0.69
		n	3.53 ± 0.31	2.47 ± 0.30	2.23 ± 0.23	2.27 ± 0.19	2.64 ± 0.18
		R^2	0.9772	0.9531	0.9640	0.9793	0.9879

Note: q_e represents the total cadmium uptake (mg/g).

C_e is the equilibrium concentration of cadmium in the solution phase (mg/L).

Q is the Langmuir maximum sorption capacity (mg/g).

b is the Langmuir constant (L/mg) related to the adsorption energy.

K is the Freundlich constant related to adsorption capacity.

n is the heterogeneity factor indicating the adsorption intensity of the adsorbate.

2.3.5. Effects of HA and co-existing ions

Fig. 2-6 shows equilibrium Cd removal by CMC-$Fe_3(PO_4)_2$ in the presence of various concentrations of HA (0-10 mg/L as TOC). The Cd removal was inhibited by 5.7 % when the HA concentration was increased from 0 to 10 mg/L as TOC (p value of 1.37×10^{-4} at the 0.05 level of significance). HA could affect the Cd sorption in several ways: (1) HA contained various functional groups such as amino and carboxylic groups (Yates III and von Wandruszka, 1999), which could complex with Fe^{2+} and Cd^{2+}; (2) HA may compete with CMC molecules on the surface of CMC-$Fe_3(PO_4)_2$ nanoparticles, altering the physical stability of the nanoparticles and resulting in larger particles and less negative zeta potential; (3) The attachment of HA molecules on the CMC-$Fe_3(PO_4)_2$ surface may increase the mass transfer barrier for Cd uptake; and (4) Adsorbed HA may facilitate adsorption of Cd^{2+} through surface complexation. The combination of all the mechanisms resulted in a slight decrease in Cd uptake when HA concentration was <10 mg/L as TOC.

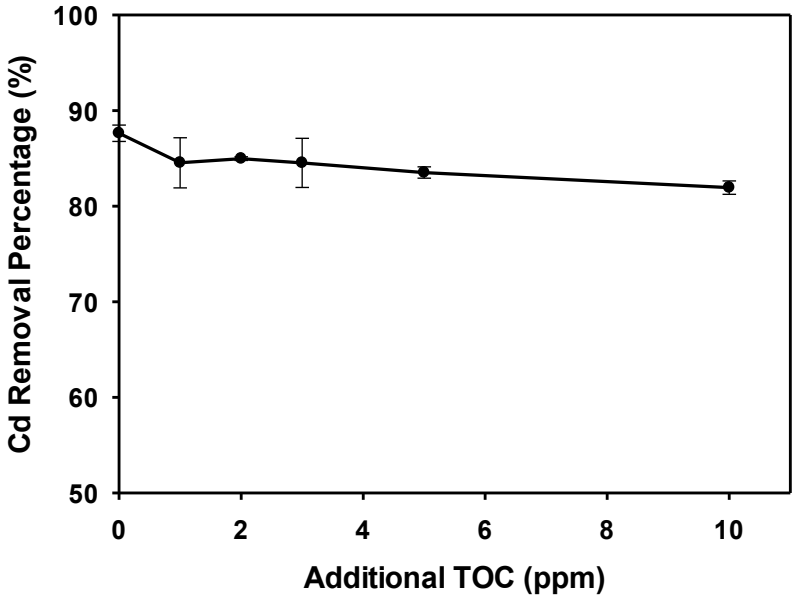

Fig. 2-6. Effects of humic acid on equilibrium cadmium removal by CMC-$Fe_3(PO_4)_2$. $Fe_3(PO_4)_2$ = 426 mg/L, CMC-to-$Fe_3(PO_4)_2$ molar ratio = 3.1×10^{-3}, initial Cd^{2+} = 1 mg/L, the TOC of CMC = 340.7 mg/L, and pH = 7.00 ± 0.20.

Fig. 2-7 shows the equilibrium uptake of Cd by CMC-$Fe_3(PO_4)_2$ in the presence of a range of NaCl, $NaNO_3$, or $NaHCO_3$ (0-10 mM). Increasing the $NaNO_3$ concentration from 0 to 10 mM inhibited the Cd removal from 87.6% to 80.2%, a 7.4% reduction; whereas increasing the NaCl and $NaHCO_3$ concentration from 0 to 10 mM raised the Cd removal from 87.6% to 89.0% and 92.5%, respectively. The co-existing ions can affect Cd uptake in several ways: First, elevated concentrations of ions can compress the electrical double layer and suppress the negative surface potential of CMC-$Fe_3(PO_4)_2$ nanoparticles, leading to aggregation and thus increased particle size. Meanwhile, the less negative surface potential is less favorable to interacting with the positively charged Cd^{2+}. Second, Na^+ ions can directly compete with Cd^{2+} for the sorption sites. Third, addition of HCO_3^- can slightly increase the pH which results in the increasing of Cd uptake. The reasons were discussed in **Section 2.3.4**. Fourth, Cl^- can react with Cd^{2+} and PO_4^{3-} to form precipitation (**Eq. 2-8**), which has a K_{sp} value of $10^{-49.66}$ (Wan et al., 2018). However, Cl^- in fresh groundwater barely exceeds 2.8 mM, and thus, no detrimental inhibitive effect would be expected when used for *in situ* remediation of Cd-contaminated groundwater.

$$5Cd^{2+} + 3PO_4^{3+} + Cl^- \rightarrow Cd_5(PO_4)_3Cl\,(s) \qquad \textbf{(2-8)}$$

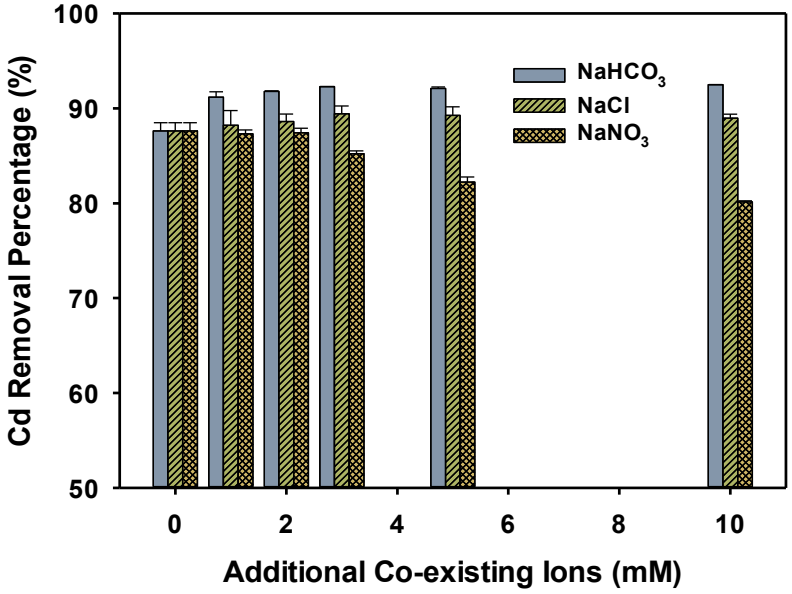

Fig. 2-7. Effects of co-existing ions $NaHCO_3$, NaCl, and $NaNO_3$ on Cd equilibrium uptake by CMC-$Fe_3(PO_4)_2$. $Fe_3(PO_4)_2$ = 426 mg/L, CMC-to-$Fe_3(PO_4)_2$ molar ratio = 3.1×10^{-3}, initial Cd^{2+} = 1 mg/L, initial ionic strength = 11.6 mM, and pH = 7.00 ± 0.20.

2.4. Conclusions

This study demonstrated potential and viability of CMC-stabilized $Fe_3(PO_4)_2$ nanoparticles for enhanced immobilization of Cd from contaminated water or groundwater. The primary findings are summarized as follows:

(1) Fully stabilized $Fe_3(PO_4)_2$ nanoparticles were prepared at 426 mg/L using 0.1 wt.% CMC, which showed much smaller size than bare $Fe_3(PO_4)_2$ particles. FTIR analysis revealed that CMC molecules were attached to the surface of $Fe_3(PO_4)_2$ nanoparticles by interactions between hydroxyl or carboxyl functional groups and Fe.

(2) The particle stabilization greatly enhanced equilibrium Cd removal from 69.1% to 90.8% when the CMC-to-$Fe_3(PO_4)_2$ molar ratio was increased from 0 to 7.8×10^{-3}. However, further increasing the ratio from 7.8×10^{-3} to 1.2×10^{-2} diminished the Cd uptake by 9.2%.

(3) Sorption kinetic tests indicated a faster Cd removal rate of CMC-$Fe_3(PO_4)_2$ compared with bare $Fe_3(PO_4)_2$. More than 87.6% Cd removal was achieved using 100 mg/L CMC-$Fe_3(PO_4)_2$ (initial Cd = 1 mg/L, pH = 7.0) within 11 h. The kinetic data were adequately interpreted by a pseudo-second-order kinetic model. The rate constants for Cd removal by CMC-$Fe_3(PO_4)_2$ and bare $Fe_3(PO_4)_2$ were 12.25 and 2.67 $g \cdot mg^{-1} \cdot hr^{-1}$, respectively.

(4) FTIR analyses showed that surface complexation between Cd and $Fe_3(PO_4)_2$ were the key immobilization mechanisms. A Langmuir isotherm model was able to adequately interpret the equilibrium sorption data. The maximum Cd sorption capacity by CMC-$Fe_3(PO_4)_2$ was determined to be 36.1 mg/g at pH 7.0.

(5) Cd uptake via CMC-$Fe_3(PO_4)_2$ was enhanced with increasing pH from 4.0 to 8.0. HA slightly inhibit Cd removal when HA concentration was increased from 0 to 10 mg/L as TOC. The addition of 10 mM $NaNO_3$ suppressed the Cd removal, while the addition of 10 mM NaCl or $NaHCO_3$ could improve Cd uptake.

CMC-stabilized $Fe_3(PO_4)_2$ nanoparticles offer some unique advantages, including considerable sorption capacity and reaction rate. The nanoparticles hold the potential to serve as an effective and environmentally friendly sorbent for *in situ* immobilization of Cd in contaminated water and soil.

Chapter 3. Efficient Removal and Long-term Sequestration of Cadmium from Aqueous Solution Using Ferrous Sulfide Nanoparticles: Performance, Mechanisms, and Long-term Stability

Cadmium (Cd) is one of the most commonly detected toxic heavy metals in the environment. Ferrous sulfide (FeS) nanoparticles were prepared using sodium carboxymethyl cellulose (CMC) as a stabilizer and tested for removal of Cd from aqueous solutions. Effects of CMC concentration, initial Cd concentration, pH, humic acid (HA) and dissolved oxygen were examined. Fully stabilized FeS (100 mg/L) nanoparticles were obtained using 0.01 wt.% CMC. Batch kinetic tests showed that the nanoparticles at 100 mg/L as FeS rapidly removed 93% of 1 mg/L Cd within 4 h at pH 7.0, and the kinetic data were well interpreted by a pseudo-second-order rate model with a rate constant of 6.68 $g \cdot mg^{-1} \cdot hr^{-1}$. Sorption isotherm was well simulated by a dual-mode isotherm model with a maximum Langmuir sorption capacity of 497.5 mg/g at pH 7.0. Fourier transform infrared (FTIR) spectroscopy and X-ray powder diffraction (XRD) analyses suggested chemical precipitation and surface complexation between Cd and FeS were dominant immobilization mechanisms. Increasing pH from 4.0 to 8.0 enhanced Cd removal rate from 73.0% to 98.8%, whereas addition of 10 mg/L HA (as total organic matter) inhibited the removal rate from 93.9% to 92.8% and the presence of molecular oxygen had negligible effect. Increasing NaCl or $CaCl_2$ from 0 to 10 mM suppressed Cd removal by 10.1% and 27.7%, respectively. The immobilized Cd remains insoluble when aged for 717 days under anoxic or oxic conditions. This study demonstrated that CMC-stabilized FeS nanoparticles can facilitate long-term immobilization of cadmium in contaminated water.

3.1. Introduction

Cadmium (Cd) is one of the most detected toxic heavy metals in the environment. It is generated from both natural sources (e.g., rocks and erosion of natural deposits) and anthropogenic sources (e.g., plastic manufacturing, polymer production, electroplating, corrosion of galvanized pipes, metal refineries, and waste batteries and paints) (ATSDR, 2008). Exposure to elevated levels of Cd may cause damage of lung, kidney, bones and children's brain, cardiovascular disease, obstructive pulmonary disease, and even breast cancer. To mitigate human exposure, the US Environmental Protection Agency (EPA) has set the maximum contaminant level (MCL) of Cd in drinking water at 0.005 mg/L (EPA, 2009b).

Various techniques have been applied to treat Cd-contaminated water, including chemical precipitation, coagulation, filtration, ion exchange, reverse osmosis, adsorption, and bioremediation (Bailey et al., 1999). Among them, adsorption is considered as a common and commercially adopted approach worldwide due to its low operation cost and easy handling. A variety of adsorbents have been investigated for removal of Cd, including metal oxides (e.g., Fe, Mn and/or Al oxides) (Dong et al., 2000), carbon nanotubes (Li et al., 2003), natural organic materials (e.g. algae (Yu et al., 2001) and carbonized coir pith (Kadirvelu and Namasivayam, 2003)), resins (Naushad et al., 2019; Naushad et al., 2015), and fly ash (Ayala et al., 1998). However, these adsorbents bear with several critical drawbacks, such as long reaction time, low sorption capacity, and/or potential secondary pollution. In addition, the bulk materials can hardly be used for *in situ* soil remediation. Thus, it is urgently needed to explore more cost-effective and environmentally friendly adsorptive materials with fast sorption rate and high sorption affinity and capacity for Cd at environmental related concentrations.

Various sorbents have been reported to be able to remove or immobilize Cd in water and sediments, such as rhamnolipid coated nanoscale zero valent iron (Xue et al., 2018b; Xue et al., 2018c), biochar (Ahmad et al., 2018), and magnetite (Zhao et al., 2018a). Among them, sulfur-containing minerals have been known to offer strong affinity for cadmium (K_{sp} of CdS = 1×10^{-27}) (Fu et al., 2010). Of all the commonly reported S-containing minerals including pyrite (FeS_2), greigite (Fe_3S_4), pyrrhotite ($Fe_{1-x}S$), and ferrous sulfide (FeS) (Özverdi and Erdem, 2006), FeS has drawn the greatest attention due to its high Cd sorption capacity, ubiquitous presence, unique molecular structure and surface chemical property, and long-term stability in anoxic environments (Gong et al., 2014). Cadmium can be immobilized by FeS via surface complexation and chemical precipitation as depicted in **Eq. 3-1** and **3-2** (Anirudhan et al., 2008):

$$\mathrm{FeS(s)} + \mathrm{Cd^{2+}} \rightarrow \mathrm{FeS-Cd^{2+}}\ \text{(Surface complexation)} \qquad (\mathbf{3\text{-}1})$$

$$\mathrm{FeS(s)} + \mathrm{Cd^{2+}} \rightarrow \mathrm{CdS} + \mathrm{Fe^{2+}}\ \text{(Chemical precipitation)} \qquad (\mathbf{3\text{-}2})$$

However, natural or conventionally prepared FeS particles tend to form large aggregates rapidly into the millimeter or larger scale, limiting their sorption capacity and soil deliverability. For instance, Ito et al. (Ito et al., 2004) prepared magnetic FeS particles with diameters of approximately 20 μm via sulfate-reducing bacteria and reported a low Cd sorption capacity of 9.85 mg/g.

Nanoscale FeS materials are expected to offer much higher sorption capacity compared with bare FeS particles due to their larger specific surface area, more active sorption sites, and higher surface reactivity. Moreover, fully stabilized FeS nanoparticles may be directly delivered into contaminated soil to facilitate *in situ* remediation. Recently, Xiong et al. (2009) and Gong et al. (2014) developed a "green" technique for preparing a new class of stabilized FeS nanoparticles using sodium carboxymethyl cellulose (CMC) as a stabilizer, and the stabilized FeS nanoparticles

(CMC-FeS) enhanced the maximum sorption capacity for mercury by 20% compared to bare FeS particles. They also demonstrated that the stabilized nanoparticles can be delivered into soil/sediment in a controllable manner. However, to our best knowledge, the effectiveness of CMC-FeS for immobilization of Cd at environmentally relevant levels and under various environmental conditions has not yet been explored. Moreover, the long-term stability of immobilized Cd remains to be addressed.

The overall goal of this study is to evaluate the effectiveness of CMC-FeS for Cd removal from aqueous solution and the long-term stability of particle-bound Cd. The specific objectives are to: (1) test Cd sorption capacity using CMC-FeS nanoparticles prepared at various CMC-to-FeS molar ratios; (2) examine effects of reaction time, initial Cd concentration, pH, humic acid (HA), and dissolved oxygen on Cd removal by CMC-FeS; (3) elucidate the underlying immobilization mechanisms; and (4) determine long-term stability of immobilized Cd.

3.2. Materials and methods

3.2.1. Chemicals

All chemicals used in this study were in the analytical grade or higher. Iron sulfate heptahydrate ($FeSO_4 \cdot 7H_2O$), cadmium chloride ($CdCl_2$), and CMC (MW = 90 000 in the sodium form, degree of substitute = 0.7) were purchased from Acros Organics (Pittsburgh, PA, USA). The Suwannee River Humic Acid was obtained from the International Humic Substances Society (IHSS, Georgia Tech, Atlanta, GA, USA). According to the supplier, the HA contained water (8.15%), ash (7.0%), C (52.47%), H (4.19%), O (42.69%), N (1.10%), S (0.65%), and P (0.02%) (all by weight). Sodium sulfide nonahydrate ($Na_2S \cdot 9H_2O$), sodium hydroxide (NaOH), and hydrochloric acid (HCl) were obtained from VWR International (Radnor, PA, USA).

3.2.2. Preparation and characterization of CMC-FeS nanoparticles

A 150 mL suspension of CMC-FeS nanoparticles was prepared in a 250 mL glass bottle following the previously reported procedure (Xiong et al., 2009). In brief, first, a 1 wt.% CMC stock solution was prepared. Then, 1.5 mL of the stock solution was added into 118.5 mL deionized (DI) water, and the mixture was purged with purified N_2 (>99%) for 15 min to remove dissolved oxygen (DO). Meanwhile, solutions of 8.5 mM $FeSO_4$ (20 mL) and 17.0 mM Na_2S (20 mL) were prepared with N_2-purged DI water. Under N_2 purging, the $FeSO_4$ solution (20 mL) was added to the CMC solution to yield a solution with 1.2 mM of Fe^{2+} and 1.08×10^{-2} wt.% of CMC. The mixture was then purged with N_2 for 5 min to assure complete mixing and formation of Fe^{2+}–CMC complexes. Then, the Na_2S solution (10 mL) was introduced into the solution dropwise under shaking at 150 rpm and vacuum through a burette at an Fe-to-S molar ratio of 1:1. To ensure complete reaction, the system was shaken for another 5 min. The resultant nanoparticle suspension contained 100 mg/L FeS and 0.01 wt.% of CMC. For comparison, bare FeS particles were prepared in the absence of CMC but under otherwise identical conditions. The particles were then sealed and aged for 24 h before use.

Transmission electron microscopy (TEM) analysis was carried out using a Zeiss EM10 transmission electron microscope (Zeiss, Thornwood, NJ, USA) operated at 60 kV. A 10 μL aqueous sample was placed on a formvar-carbon-coated copper grid (Electron Microscopy Sciences, Hatfield, PA, USA), allowing for full contact/spreading on the grid, followed by vacuum drying for 12 h. The particles attached to the grid were then imaged. X-ray powder diffraction (XRD) was obtained using a Bruker D8 Discover X-ray diffractometer (Bruker Corp., Madison, WI, USA) with a Cu Kα (λ = 1.540 60 Å) radiation. To this end, CMC-FeS nanoparticles were prepared at 500 mg/L as FeS at a CMC-to-FeS molar ratio of 1.0×10^{-3} in a 1 L suspension. Bare

FeS particles were prepared following the same procedure without CMC. Cd-loaded nanoparticles were obtained following the sorption kinetic tests as described in **Section 3.2.5** with an equilibrium time of 48 h. The nanoparticles were collected by filtering the suspensions using a 25 nm membrane filter of mixed cellulose esters (Millipore Corp., Billerica, MA, USA), which was able to completely remove the nanoparticles but did not retain soluble Cd. The solids were then rinsed three times with N_2-purged DI water, and subsequently freeze-dried under vacuum at −50 °C using a VirTis freeze mobile freeze-dryer (Gardiner, NY, USA) for 48 h. The samples were placed on a zero-background sample holder and scanned from 10° to 80° 2θ angles using a step interval of 0.02° and a scan speed of 5°/min. The XRD patterns were processed using the computer program known as DIFFRAC.EVA loaded with an ICDD database (Materials Data Inc., Livermore, CA, USA). Fourier transform infrared (FTIR) spectroscopy measurements of the freeze-dried samples were carried out using a SHIMADZU IR Prestige-21 spectrometer (Shimadzu Scientific Instruments, Columbia, MD, USA) to explore the interactions between FeS and CMC, and between Cd and CMC-FeS. The freeze-dried Cd-laden CMC-FeS samples were mixed with KBr powder to form thin KBr pellets consisting of 2 wt.% of the nanoparticles. A pure KBr pellet was used as a background to obtain the net FTIR spectra of the samples. For comparison, FTIR spectra for Cd-free CMC-FeS particles and neat CMC were also acquired in the same manner. Dynamic light scattering (DLS) tests of the FeS particles were performed with a Malvern Zetasizer Nano ZS (Malvern Instruments, Worcestershire, UK) to yield number-weighted particle size distributions and zeta potentials. Solution viscosities were measured with a Gilmont falling-ball viscometer (Barnant Company, Barrington, IL, USA) and then used to correct for the influence of viscosity on the DLS measurements. All measurements were conducted in duplicate, and data were reported as mean ± relative deviation from the mean.

3.2.3. Effects of CMC concentration on cadmium uptake by FeS

FeS particles were prepared at a fixed FeS concentration of 100 mg/L as FeS and at various concentrations of CMC, namely, at CMC-to-FeS molar ratios of 0, 5.0×10^{-4}, 1.0×10^{-3}, 1.5×10^{-3}, 2.0×10^{-3}, 2.4×10^{-3}, 2.9×10^{-3}, and 3.9×10^{-3}. The solution pH was kept at 7.00 ± 0.20 in all cases. To examine the effects of CMC on cadmium removal, sorption tests were carried out with the FeS particles following the procedures as described in **Section 3.2.4** with a reaction time of 48 h. In addition, effects of CMC on the physical stability of FeS particles were examined. To this end, the FeS suspensions were allowed to age for 24 h and settle under gravity, and then 1 mL of the top supernatant was sampled and mixed with 4 mL of 12 M HCl for 5 min to completely dissolve the nanoparticles, and then analyzed for total Fe. Both Fe and Cd were measured by ICP-OES 710-ES (Agilent Technologies, Santa Clara, CA, USA) with detection limits of 1 µg/L and 0.1 µg/L, respectively.

3.2.4. Cadmium sorption kinetic tests

Batch Cd sorption kinetic experiments were carried out in 50 mL Teflon vials under anoxic conditions. The reaction conditions were as follows: initial Cd concentration = 1 mg/L, FeS = 100 mg/L, and pH = 7.00 ± 0.20 (maintained with HCl and/or NaOH). The mixtures were sealed and continuously mixed on an end-over-end rotator operated at 50 rpm at room temperature (20 ± 1 °C). At predetermined times, duplicate vials were sacrificially sampled. The samples were then filtered through the 25 nm membrane filters and analyzed for Cd concentration in the filtrates. Control tests showed that loss of cadmium during the sorption and sample filtration was <2% in all cases.

3.2.5. Cadmium sorption isotherm and effects of pH

Cd sorption isotherms by CMC-FeS were constructed following similar procedures to the kinetic tests where the systems were equilibrated for 48 h. The experimental conditions were: FeS

= 100 mg/L, CMC-to-FeS molar ratio = 1.0×10^{-3}, initial Cd^{2+} = 0.6-30 mg/L, and pH = 7.00 ± 0.20. The equilibrium cadmium uptake was calculated based on differences between the initial and final concentrations of Cd in the aqueous phase. To test the pH effects on the Cd sorption, the sorption isotherms were also obtained at equilibrium pH values ranging from 4.0 to 8.0.

3.2.6. Effects of HA, co-existing ions, and dissolved oxygen

Batch Cd sorption equilibrium tests were conducted in 50 mL Teflon vials to investigate the effects of HA, co-existing ions, and oxygen. Each vial was loaded with 100 mg/L of CMC-FeS and 1 mg/L of Cd^{2+}, and equilibrated for 48 h at a constant pH of 7.00 ± 0.20. To probe the HA effect, the tests were conducted in the presence of various concentrations of HA (1 to 10 mg/L as total organic carbon (TOC)). TOC was analyzed using a Tekmar Dohrmann Phoenix 8000 UV Persulfate TOC Analyzer (Mason, OH, USA) with a detection limit of 2 μg/L. To investigate effects of commonly co-existing ions, the sorption tests were carried out in the presence of various concentrations of NaCl (0-10 mM) or $CaCl_2$ (0-10 mM). To examine the effect of dissolved oxygen (DO), the experiments were conducted under anoxic and oxic (open to air) conditions.

3.2.7. Long-term stability of FeS-immobilized Cd

To investigate the long-term stability of immobilized cadmium by CMC-FeS, the sorption tests under anoxic and oxic conditions at a constant pH of 7.00 ± 0.20 in **Section 3.2.6** were extended to 717 days. The samples were then filtered through the 25 nm membrane filters and analyzed for Cd concentration in the filtrates.

3.3. Results and discussion

3.3.1. Characterization of CMC-stabilized FeS nanoparticles and Cd-binding mechanisms

Fig. 3-1 shows the TEM image of CMC-stabilized FeS nanoparticles prepared at a CMC-to-FeS molar ratio of 1.0×10^{-3}. The particles were rather poly-dispersed with a size range from 9.89 nm to 60.22 nm and with a mean particle size of 28.42 ± 6.32 nm. At the experimental pH of 7.0, CMC was negatively charged (pK_a of CMC = 4.3), resulting in a zeta potential of -66.5 mV for CMC-FeS. CMC stabilized the nanoparticles through concurrent electrostatic repulsion and steric hinderance (He and Zhao, 2007). The specific surface area (S, m^2/g) of the FeS particles is inversely related to the radius (r, m) of nanoparticles (Kecskes et al., 2003):

$$r = 3(\rho * S)^{-1} \quad (\mathbf{3\text{-}3})$$

where ρ is the density of FeS (4740 kg/m^3). As the mean particle size of CMC-FeS nanoparticles was 28.42 nm measured by TEM, the S value was calculated to be 44.5 m^2/g, compared to 16.7 m^2/g for non-stabilized FeS (Gong et al., 2014).

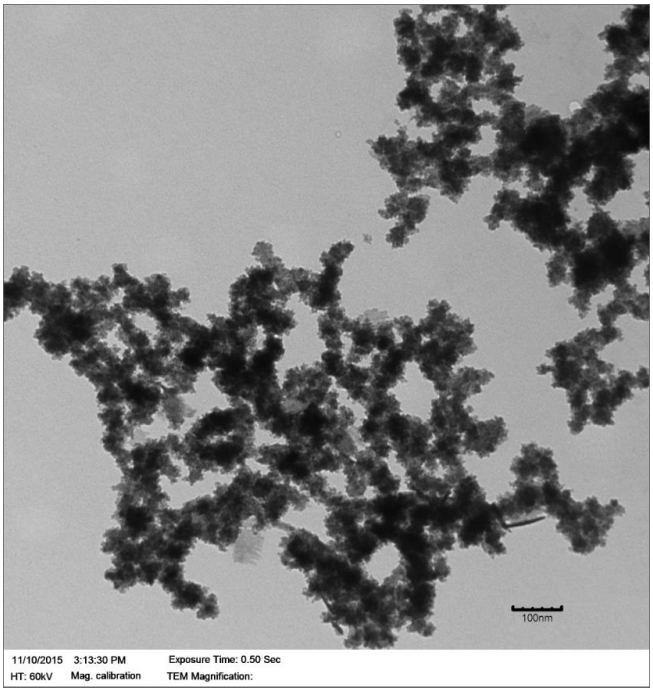

Fig. 3-1. TEM image of CMC-stabilized FeS nanoparticles. FeS = 100 mg/L, and CMC-to-FeS molar ratio = 1.0×10^{-3}.

Fig. 3-2 compares the XRD diffractograms of bare FeS, CMC-FeS, and Cd-laden CMC-FeS particles. For bare FeS and CMC-FeS, the peaks observed at 2θ values of 14.5°, 33.6°, 47.1°, 53.5°, and 64.1° were attributed to the FeS particles (Liu et al., 2008; Wolthers et al., 2003), whereas those at 19.2°, 35.7°, 54.1°, and 62.5° were characteristic peaks of Fe_3O_4 (Shi et al., 2012), indicating partial oxidation of FeS during the preparation/handling process. It is noteworthy that the peaks for CMC-FeS were much weakened compared to those of bare FeS, which can be attributed to: (1) the much smaller particle size of CMC-FeS, and (2) CMC's inhibitive effect on the growth of FeS crystals during the nucleation stage of CMC-FeS. For Cd-laden CMC-FeS, the peaks at 25.9°, 28.3°, 36.8°, 43.7°, 49.0°, 54.9°, 67.9°, and 73.2° were characteristic of CdS (Cao et al., 2015), indicating formation of CdS on the particle via chemical precipitation (K_{sp} = 1×10^{-27}).

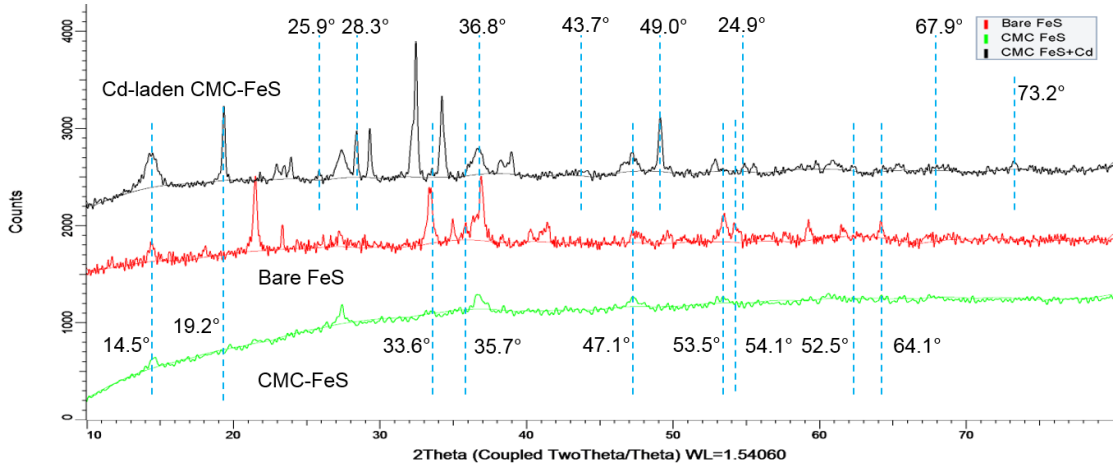

Fig. 3-2. XRD spectra of bare FeS, CMC-FeS nanoparticles, and Cd-laden CMC-FeS. Bare FeS = 500 mg/L and solution pH = 7.00 ± 0.20; CMC-FeS was prepared at the CMC-to-FeS molar ratio of 1.0×10^{-3} under otherwise identical conditions; Cd-laden CMC-FeS were prepared by equilibrating the same CMC-FeS with 30 mg/L of Cd.

Fig. 3-3 presents the FTIR spectra of neat CMC, CMC-FeS, and Cd-laden CMC-FeS. Four peaks were observed for CMC-FeS at the wavenumbers of 3352, 1580, 1408, and 1016 cm^{-1}, which are attributed to interactions between Fe^{2+} and COO^- (1580 and 1408 cm^{-1}) or −OH groups (3352 and 1016 cm^{-1}) (He et al., 2007). The −OH stretching band shifted from 3379 cm^{-1} for neat CMC to 3352 cm^{-1} for CMC-FeS, which is ascribed to enhanced intermolecular hydrogen bonding between CMC and the FeS surface (Sylvestre et al., 2004). Moreover, the band observed at 2884 cm^{-1} for neat CMC was shifted to 2851 cm^{-1}, indicating the C−H stretching vibration from the CH_2 groups of the stabilizer (Maity and Agrawal, 2007). The bands at 1587, 1412, and 1018 cm^{-1} for neat CMC are ascribed to asymmetric and symmetric vibrations of COO^- groups and C−O stretching (RCH_2OH) (Brown et al., 1988). Likewise, these peaks were shifted to 1580, 1408, and 1016 cm^{-1}, respectively. For CMC-FeS, the wavenumber separation (Δ) between the asymmetric $\upsilon_{as}(COO^-)$ (1580 cm^{-1}) and symmetric $\upsilon_s(COO^-)$ (1408 cm^{-1}) stretches was 172 cm^{-1}, suggesting that the primary mechanism for binding CMC to FeS was bidentate bridging (He et al., 2007). Upon Cd^{2+} uptake, the FTIR spectra showed similar absorption band characteristics, namely, −OH group (3344 cm^{-1}), C−H stretching (2850 cm^{-1}), asymmetric and symmetric stretches of COO^- groups (1585 and 1409 cm^{-1}), and C−O stretching (RCH_2OH) (1016 cm^{-1}). Yet, the −OH stretching band shifted from 3352 cm^{-1} for CMC-FeS to 3344 cm^{-1} for Cd-laden CMC-FeS, the

C−H stretching vibration shifted from 2851 cm^{-1} to 2850 cm^{-1}, and the asymmetric and symmetric stretches of COO^- shifted from 1580 and 1408 cm^{-1} to 1585 and 1409 cm^{-1}, respectively. Meanwhile, the IR frequencies of asymmetric and symmetric stretches of COO^- and C−O stretching were increased by 24.3%, 53.2%, and 134.3%, respectively upon Cd uptake. All these changes suggest that surface complexation between CMC-FeS and Cd was involved, where S in FeS acts as the Lewis base and Cd as the Lewis acid.

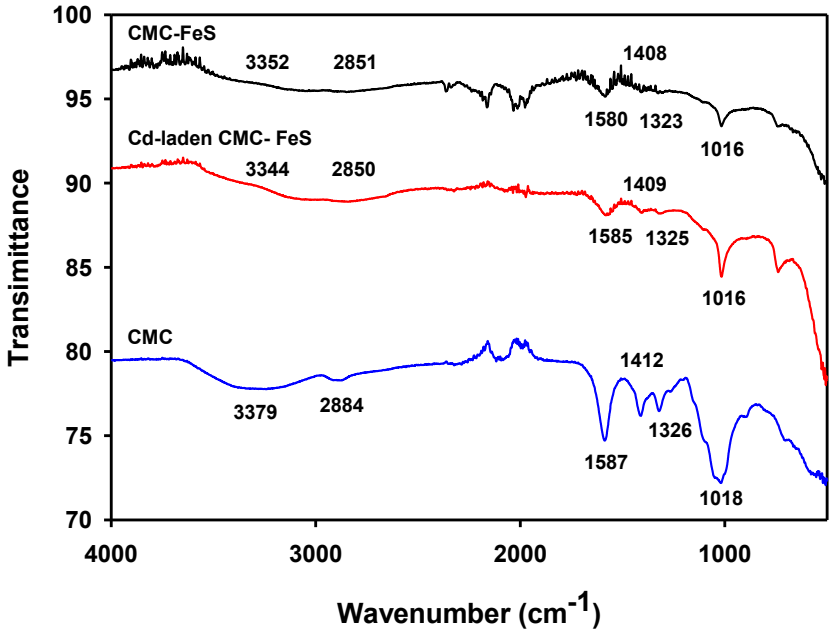

Fig. 3-3. FTIR spectra of neat CMC powder, CMC-FeS nanoparticles, and Cd-laden CMC-FeS. CMC-FeS preparation: FeS = 500 mg/L, CMC-to-FeS molar ratio = 1.0×10^{-3}, and solution pH = 7.00 ± 0.20; Cd-laden CMC-FeS was prepared by equilibrating the same CMC-FeS with 30 mg/L of Cd^{2+}.

Based on the XRD and FTIR results, it is evident that CMC-FeS took up Cd through concurrent surface complexation (**Eq. 3-1**) and chemical precipitation (formation of CdS) (**Eq. 3-2**).

3.3.2. Effects of CMC concentration on cadmium uptake by FeS

Fig. 3-4 shows the effect of the stabilizer concentration on the equilibrium uptake of Cd^{2+} by FeS particles. The Cd^{2+} removal increased from 69.1% to 95.8% when the CMC-to-FeS molar ratio was increased from 0 to 2.0×10^{-3}, with the maximum removal occurred at CMC-to-FeS molar ratios of 1.0×10^{-3}–2.4×10^{-3}. Evidently, increasing CMC concentration resulted in smaller FeS particles (**Fig. 3-1**), and therefore, greater specific surface area (44.5 m^2/g for CMC-FeS vs. 16.7 m^2/g for non-stabilized FeS) and more sorption sites. However, further increasing the CMC-to-FeS molar ratio above 2.4×10^{-3} resulted in a slight but significant decrease in Cd removal (Based on the *t*-tests, the differences are statistically significant with a *p* value of 0.0013 at the 0.05 level of significance). For instance, Cd^{2+} uptake was reduced by 2.7% when the CMC-FeS ratio was elevated from 2.5×10^{-3} to 3.9×10^{-3}. The inhibition can be attributed to the excessive uptake of CMC molecules on the particle surface, resulting in a denser CMC coating on the nanoparticles, which may inhibit access of Cd to the particles' surface sites due to elevated mass transfer resistance and/or blockage of the sorption sites (He and Zhao, 2008); on the other hand, complexation of soluble CMC with Cd^{2+} may prevent sorption of Cd^{2+} on the particle surface.

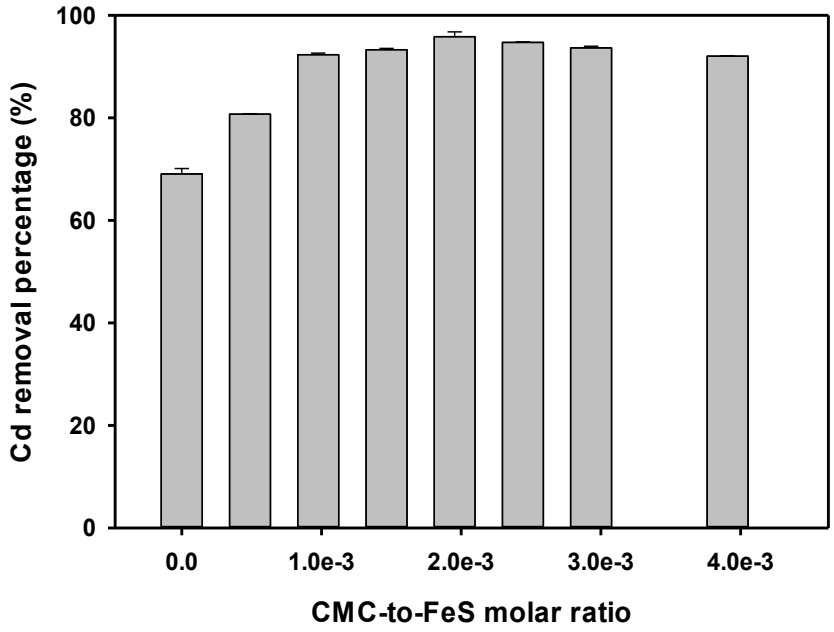

Fig. 3-4. Equilibrium cadmium removal by FeS particles prepared at various CMC-to-FeS molar ratios. Initial Cd^{2+} = 1 mg/L, FeS = 100 mg/L, equilibrium pH = 7.00 ± 0.20, and equilibration time = 48 h.

Particle stability measurements indicated that complete particle stabilization was achieved at a CMC-to-FeS molar ratio of 1.0×10^{-3}, i.e., 100% of CMC-FeS nanoparticles remained suspended after 24 h gravity settling. In contrast, only 3% of non-stabilized FeS particles were detected in the top supernatant.

Taken together, the particle stabilization not only facilitates soil delivery (Gong et al., 2012), but also elevates Cd sorption capacity. While the ultimate goal is to apply CMC-FeS to *in situ* remediation of Cd-contaminated soil and groundwater, the information from this work provides important fundamental data pertaining to the process effectiveness and viability. Considering both

Cd uptake capacity and physical stability, CMC-FeS prepared at the CMC-to-FeS molar ratio of 1.0×10^{-3} was considered optimal, and thus, was further tested in the subsequent experiments.

3.3.3. Sorption kinetics of Cd by CMC-FeS

Fig. 3-5A shows Cd^{2+} removal kinetics by bare FeS and CMC-FeS. For both cases, the removal displays a rapid initial rate (89.5% of equilibrium capacity was achieved in the first 0.33 h by CMC-FeS, and 74.9% in the first 1 h by bare FeS particles), followed by a gradual phase till equilibrium at ~4 h for CMC-FeS and ~12 h for bare FeS, which is consistent with the common notion that more accessible sites are occupied first (Axe and Anderson, 1995). At equilibrium, 93.4% of Cd was removed by CMC-FeS, compared to 89.3% for bare FeS. The faster removal rate and higher removal capacity of CMC-FeS can be attributed to the smaller particle size and larger specific surface area of the nanoparticles. The commonly used pseudo-second-order kinetic model was able to simulate the kinetic data (**Fig. 3-5B**):

$$\frac{dq_t}{dt} = k_2(q_e - q_t)^2 \quad \textbf{(3-4)}$$

Integrate **Eq. 3-4** for the boundary conditions ($t = 0$, $q_t = 0$ and $t = t$, $q_e = q_t$) gives the **Eq. 3-5** below:

$$q_t = \frac{q_e t}{\frac{1}{k_2 q_e} + t} \quad \textbf{(3-5)}$$

where q_e and q_t are the amount of adsorbed Cd on the FeS particles (mg/g) at equilibrium and time t (h), respectively, and k_2 is the rate constant. For comparison, the pseudo-first-order model was also teste-fitted (not shown in figure). The expression of the pseudo-first-order model is:

$$\frac{dq_t}{dt} = k_1(q_e - q_t) \quad \textbf{(3-6)}$$

Integrating **Eq. 3-6** for the boundary conditions ($t = 0$, $q_t = 0$ and $t = t$, $q_e = q_t$) leads to the formula below (Moussout et al., 2018):

$$q_t = q_e[1 - \exp(-k_1 t)] \quad \textbf{(3-7)}$$

where q_e and q_t are the amount of adsorbed Cd on the FeS particles (mg/g) at equilibrium and time t (h), respectively, and k_1 is the rate constant. **Table 3-1** gives the best-fitted kinetic model parameters. For both bare FeS and CMC-FeS, the pseudo-second-order kinetic model provided better data fitting (R^2 = 0.9668 for bare FeS and 0.9998 for CMC-FeS) than the pseudo-first-order model (R^2 = 0.8997 and 0.9986, respectively). The k_2 values were 0.775 g·mg^{-1}·hr^{-1} for bare FeS and 6.677 g·mg^{-1}·hr^{-1} for CMC-FeS, confirming the much faster Cd removal rate of CMC-FeS.

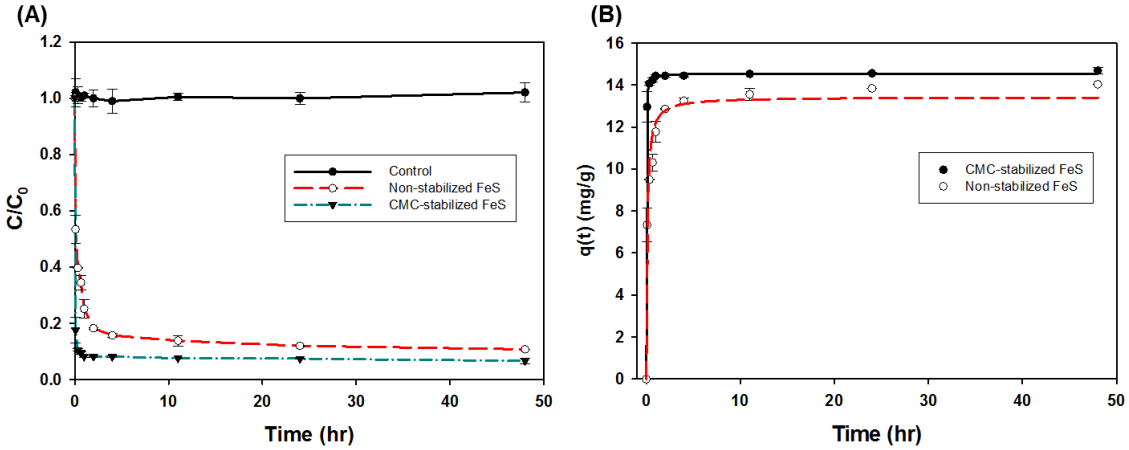

Fig. 3-5. (A) Cd^{2+} sorption kinetics using bare and CMC-stabilized FeS particles; and (B) pseudo-second-order kinetic fittings of Cd^{2+} sorption. Initial Cd^{2+} = 1 mg/L, FeS = 100 mg/L, CMC-to-FeS = 1.0 × 10^{-3} for CMC-FeS particles, and pH = 7.00 ± 0.20.

Table 3-1. Best fitted kinetic parameters with various kinetic models applied for simulating the sorption kinetics of cadmium removal by bare or CMC-stabilized FeS particles (errors given as standard deviation).

Kinetic Models	Governing Equation	Parameters		
			Non-stabilized FeS	CMC-FeS
Pseudo-first-order kinetic model	$q_t = q_e[1 - \exp(-k_1 t)]$	q_e (mg/g)	12.66 ± 0.55	14.42 ± 0.06
		k_1 (hr^{-1})	7.247 ± 2.234	27.604 ± 1.549
		R^2	0.8997	0.9986
Pseudo-second-order kinetic model	$q_t = \frac{q_e t}{\frac{1}{k_2 q_e} + t}$	q_e (mg/g)	13.42 ± 0.35	14.54 ± 0.03
		k_2 ($g \cdot mg^{-1} \cdot hr^{-1}$)	0.775 ± 0.180	6.677 ± 0.337
		R^2	0.9668	0.9998

Note: q_e is the amount of sorbed Cd (mg/g) at equilibrium.

q_e and q_t are the calculated amount of sorbed Cd (mg/g) at equilibrium and time t (h), respectively.

k_1 and k_2 are the rate constants of pseudo-first-order and pseudo-second-order kinetic models.

R^2: correlation coefficient, which is calculated per the equation $R^2 = 1 - \frac{\sum_i (y_i - y_{i(predict)})^2}{\sum_i (y_i - \bar{y})^2}$, where y_i and $y_{i(predict)}$ are the original data values and model values, respectively, and $\bar{y}$ is the mean of the observed data.

3.3.4. Sorption isotherms

Sorption isotherms of Cd onto CMC-FeS were carried out in the pH range of 4-8 (**Fig. 3-6**). It was evident that the Cd uptake was enhanced with increasing solution pH. The classical Langmuir and Freundlich models (**Eq. 3-5** and **3-6**) and a newly proposed dual-mode model (**Eq. 3-7**) were employed to fit the isotherm data (**Fig. 3-6**):

$$\text{Langmuir model: } q_e = \frac{bQC_e}{1 + bC_e} \quad \textbf{(3-8)}$$

$$\text{Freundlich model: } q_e = K C_e^{\frac{1}{n}} \quad \textbf{(3-9)}$$

$$\text{Dual-mode model: } q_e = K_d C_e + \frac{bQC_e}{1+bC_e} \quad \textbf{(3-10)}$$

where q_e represents the cadmium uptake (mg/g), C_e is the equilibrium concentration of cadmium in the solution phase (mg/L), Q is the Langmuir maximum sorption capacity (mg/g), b is the Langmuir affinity constant (L/mg) related to the adsorption energy, K is the Freundlich constant related to adsorption capacity, n is the heterogeneity factor indicating the adsorption intensity of the adsorbate, and K_d is the linear distribution coefficient (L/g) associated with precipitation in this case. **Table 3-2** summarizes the resulting fitting results. Clearly, the dual-mode isotherm model outperforms the Langmuir and Freundlich model. In this case, the dual-mode model incorporates a chemical precipitation term, which is linearly proportional to the Cd concentration, and mono-layer adsorption (surface complexation or ionic binding), and thus the model is mechanistically more sound than the other two models that take into adsorption only (Gong et al., 2014). The maximum adsorption capacities of Cd by CMC-FeS were 138.0 mg/g, 204.6 mg/g, 398.3 mg/g, 497.5 mg/g, and 532.2 mg/g, at pH of 4.0, 5.0, 6.0, 7.0, and 8.0, respectively. These capacity values are much higher than those reported for other materials (**Table 3-3**), such as 134.9 mg/g for algae at pH 5.0 (Yu et al., 2001), 93.2 mg/g for carbonized coirpith at pH 5.0 (Kadirvelu and Namasivayam, 2003), 10.9 mg/g for CNTs at pH 5.0 (Li et al., 2003), and 8.0 mg/g for fly ash at pH 5.0 (Ayala et al., 1998). As pH increased from 4.0 to 8.0, the maximum sorption capacity rosed sharply from 138.0 to 532.2 mg/g. The predominant cadmium species in the pH range is Cd^{2+}. The declined Cd removal at lower pH can be attributed to several factors. First, more of the CMC-FeS nanoparticles were dissolved at lower pH, and thus partial loss of the binding sites. As shown in **Fig. 3-7A**, 35.0% of FeS was dissolved at pH 4.0, and the

percentage was decreased to ≤1.2% at pH ≥ 7. The observation is consistent with the speciation of FeS simulated per MINTEQ (**Fig. 3-7B**). Second, lower pH was less favorable for foramtion of CdS precipitation (for H_2S, $pK_{a1} = 7.04$; $pK_{a2} = 11.96$). This is reflected by the K_d values in the the dual-mode model (**Table 3-2**), where the K_d values at pH 4.0 and 5.0 were negligible (1.517×10^{-11} and 1.371×10^{-10} L/mg, respectivily), compared to those at pH 6.0, 7.0, and 8.0 (K_d = 1.090, 2.478, and 2.522 L/mg, respectively). Namely, there was barely any CdS precipitation when pH was below 5. At alkaline, however, both chemical precipitation and surface adsorption became important mechanisms, where more CdS(s) was formed at higher pH as more free S^{2-} became available ($pK_{a1} = 7.04$, $pK_{a2} = 11.96$). Third, the increase of pH rendered more negatively charged surface of CMC-FeS, resulting in smaller paticles, larger specific area, and more favorable interactions with the Cd^{2+} cations. In fact, as pH increased from 4.0 to 8.0, the zeta potential of CMC-FeS was increased from -24.6 to -73.9 mV, and the DLS-based particle size decreased from 160.9 to 123.8 nm. In addition, the Ostwald ripening process was more likely operative at lower pH, namely, smaller particles dissolved and redeposited onto larger particles, resulting in fewer but larger particles.

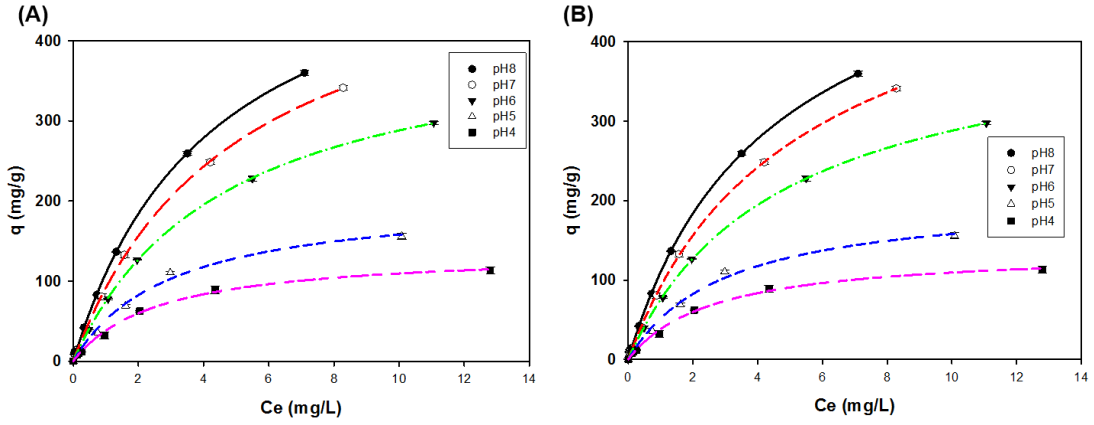

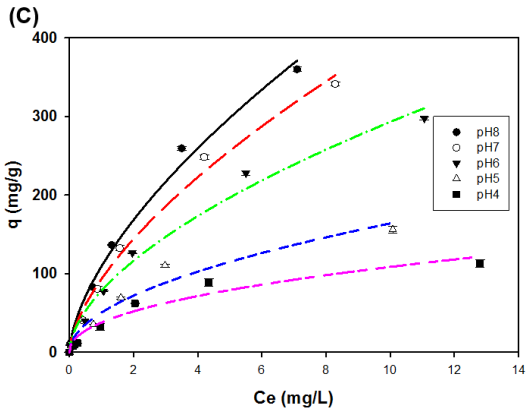

Fig. 3-6. Cadmium sorption isotherms fitted with (A) dual-mode model, (B) Langmuir model, and (C) Freundlich model for CMC-FeS nanoparticles. FeS = 100 mg/L, CMC-to-FeS = 1.0×10^{-3}, initial Cd concentration = 0.06-30 mg/L, pH = 4.0-8.0, and equilibration time = 48 h.

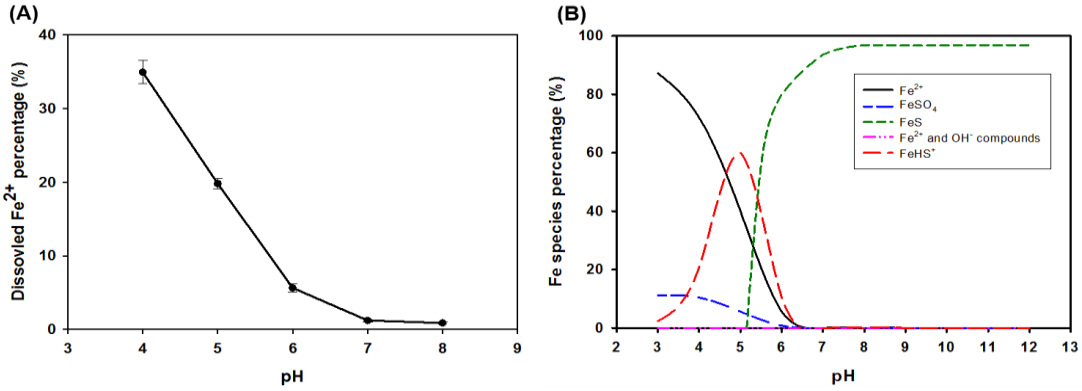

Fig. 3-7. (A) Dissolution of CMC-FeS measured as soluble Fe as a function of equilibrium pH; and (B) Fe speciation (without CMC) simulated using Visual MINTEQ (version 2.61). FeS = 100 mg/L, and CMC-to-FeS molar ratio = 1.0×10^{-3}.

Table 3-2. Langmuir, Freundlich, and dual-mode isotherm model parameters for the sorption of cadmium by CMC-stabilized FeS nanoparticles at pH 4 to 8 (errors given as standard deviation).

Sorption Isotherm Model	Governing Equation	Parameters					
		pH	**4**	**5**	**6**	**7**	**8**
Langmuir	$q_e = \frac{bQC_e}{1+bC_e}$	Q (mg/g)	138.00 ± 4.57	204.57 ± 9.44	421.49 ± 5.76	544.96 ± 11.50	573.74 ± 14.27
		b (L/mg)	0.386 ± 0.035	0.342 ± 0.038	0.216 ± 0.007	0.202 ± 0.009	0.237 ± 0.012
		R^2	0.9962	0.9943	0.9997	0.9995	0.9993
Freundlich	$q_e = KC_e^{\frac{1}{n}}$	K	37.931 ± 4.656	50.505 ± 5.865	78.157 ± 6.114	93.124 ± 5.741	109.315 ± 5.994
		n	2.226 ± 0.285	1.984 ± 0.232	1.750 ± 0.116	1.594 ± 0.086	1.608 ± 0.084
		R^2	0.9551	0.9618	0.9883	0.9926	0.9931
Dual-mode	$q_e = K_dC_e + \frac{bQC_e}{1+bC_e}$	Q (mg/g)	138.00 ± 7.22	204.57 ± 18.15	398.31 ± 40.66	497.50 ± 97.03	532.21 ± 125.31
		K_d (L/g)	$(1.517 \pm 0.189)\times10^{-11}$	$(1.371 \pm 0.691)\times10^{-10}$	1.090 ± 1.925	2.478 ± 5.160	2.522 ± 7.724
		b (L/mg)	0.387 ± 0.042	0.345 ± 0.051	0.231 ± 0.025	0.226 ± 0.042	0.267 ± 0.060
		R^2	0.9967	0.9952	0.9997	0.9996	0.9994

Note: q_e represents the total cadmium uptake (mg/g).

C_e is the equilibrium concentration of cadmium in the solution phase (mg/L).

Q is the Langmuir maximum sorption capacity (mg/g).

b is the Langmuir constant (L/mg) related to the adsorption energy.

K is the Freundlich constant related to adsorption capacity.

n is the heterogeneity factor indicating the adsorption intensity of the adsorbate.

K_d is the linear distribution coefficient (L/g) associated with precipitation.

Table 3-3. Maximum Cd sorption capacities by different materials.

Materials	Maximum sorption capacity (mg/g)	Equilibrium pH	Reference
CMC-FeS nanoparticles	138.0	4.0	Present study
	204.6	5.0	
	398.3	6.0	
	497.5	7.0	
	532.2	8.0	
Ecofriendly curcumin (7-bis(4-hydroxy-3-methoxyphenyl)-1,6-heptadiene-3,5-dione) formaldehyde resin (CFR)*	322.6	7.0	(Naushad et al., 2015)
Algae	134.9	5.0	(Yu et al., 2001)
Carbonized coirpith	93.2	5.0	(Kadirvelu and Namasivayam, 2003)
Magnetite coated biuret-formaldehyde pre polymeric resin (Fe_3O_4@BFR)	92.6	6.0	(Naushad et al., 2019)
Sulfide-modified nanoscale zerovalent iron (S-nZVI)	85.0	6.0-9.0	(Su et al., 2015)
Phosphorylated magnetic chitosan composite (P-MCS)	71.5	6.0	(Wu et al., 2019)
Carbon nanotubes (CNTs)	10.9	5.0	(Li et al., 2003)
Fly ash	8.0	5.0	(Ayala et al., 1998)

Note: Cd maximum sorption capacity of CFR was measured at 45 °C whereas the capacities for other materials were carried out at room temperature (22°C).

3.3.5. Effects of HA and co-existing ions

Fig. 3-8 shows equilibrium Cd removal by CMC-FeS in the presence of various concentrations of HA (0-10 mg/L as TOC). The Cd removal was inhibited by 2.7 % when the HA concentration was increased from 0 to 3 mg/L as TOC (*p* value of 0.0450 at the 0.05 level of significance). However, the removal rate bounced back when the HA concentration was >3 mg/L as TOC. HA could affect the Cd sorption in several ways: (1) HA contained various functional groups such as amino and carboxylic groups (Yates III and von Wandruszka, 1999), which could complex with Fe^{2+} and Cd^{2+}; (2) HA may compete with CMC molecules on the surface of CMC-FeS nanoparticles, altering the physical stability of the nanoparticles and resulting in larger particles and less negative zeta potential; (3) The attachment of HA molecules on the CMC-FeS surface may increase the mass transfer barrier for Cd uptake; and (4) Adsorbed HA may facilitate adsorption of Cd^{2+} through surface complexation.

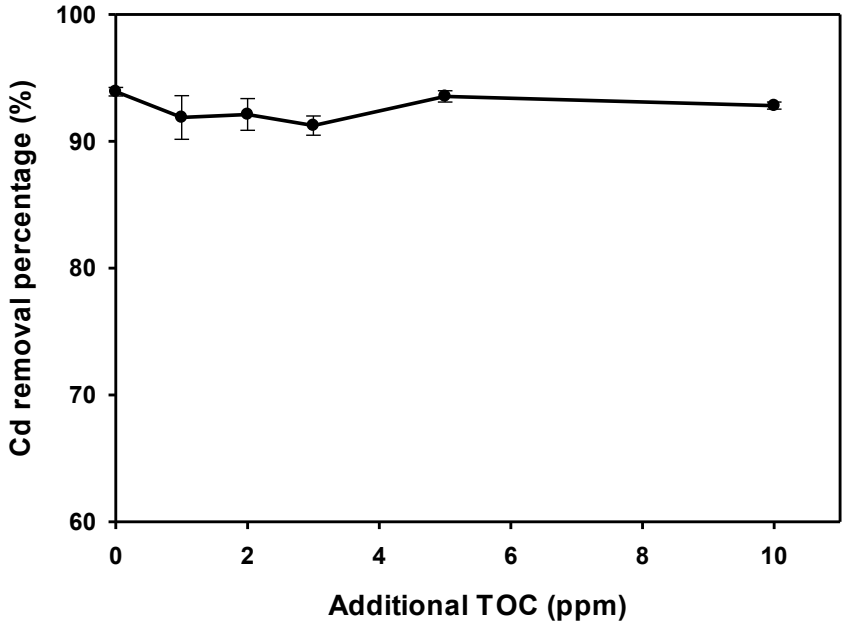

Fig. 3-8. Effects of humic acid on equilibrium cadmium removal by CMC-FeS. FeS = 100 mg/L, CMC-to-FeS molar ratio = 1.0×10^{-3}, initial Cd^{2+} = 1 mg/L, and pH = 7.00 ± 0.20.

Fig. 3-9 shows the equilibrium uptake of Cd by CMC-FeS in the presence of a range of NaCl and $CaCl_2$ (0-10 mM). Increasing the NaCl concentration from 0 to 10 mM inhibited the Cd removal from 93.9% to 84.4%, a 10.1% reduction; whereas increasing the $CaCl_2$ concentration from 0 to 10 mM suppressed the Cd removal from 93.9% to 67.9%, a 27.7% reduction. Evidently, the presence of divalent calcium demonstrated a stronger inhibiting effect on Cd sorption. The co-existing cations can affect Cd uptake in several ways: First, elevated concentrations of Na^+ or Ca^{2+} can compress the electrical double layer and suppress the negative surface potential of CMC-FeS nanoparticles, leading to aggregation and thus increased particle size. Meanwhile, the less negative surface potential is less favorable to interacting with the positively charged Cd^{2+}. Second, Ca^{2+} and Na^+ ions can directly compete with Cd^{2+} for the sorption sites. Third, Cl^- as an inorganic ligand can form soluble complexes with Cd, weakening both ion exchange and ligand exchange interactions between Cd and CMC-FeS. It is noteworthy that Ca^{2+} with higher valence showed greater inhibitive effect on Cd uptake due to its stronger ability to induce double-layer compression and electrostatic interactions with FeS. Practically, Ca^{2+} in groundwater barely exceeds 1 mM (or 100 mg/L as $CaCO_3$ hardness), and thus, no detrimental inhibitive effect would be expected when used for *in situ* remediation of Cd-contaminated groundwater.

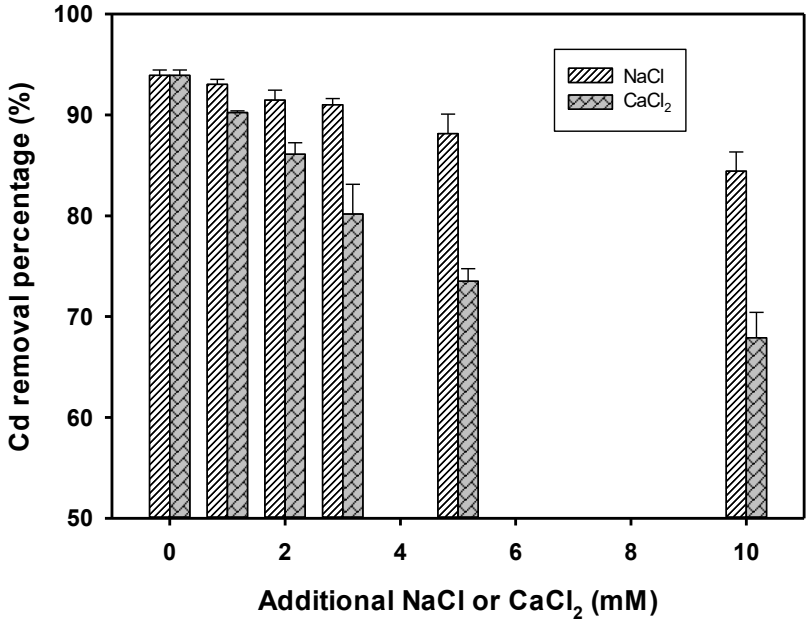

Fig. 3-9. Effects of co-existing ions NaCl and $CaCl_2$ on Cd equilibrium uptake by CMC-FeS. FeS = 100 mg/L, CMC-to-FeS molar ratio = 1.0×10^{-3}, initial Cd^{2+} = 1 mg/L, and pH = 7.00 ± 0.20.

3.3.6. Effects of dissolved oxygen and long-term stability of immobilized Cd

The presence of DO may break the interior Fe-S bonds in FeS, and thus impacts the Cd removal (Su et al., 2015). **Fig. 3-10** compares the equilibrium Cd removal by CMC-FeS under oxic or anoxic conditions at pH 7.0. After 2 days, DO slightly decreased the Cd removal from 93.4% to 91.9% (p value of 0.0446 at the 0.05 level of significance). It was interesting that DO could oxidize Fe(II) to form FeOOH (**Eq. 3-11**) (Sapsford et al., 2005), which was also an effective sorbent for Cd (Granados-Correa et al., 2011).

$$O_2(aq) + 4Fe^{2+} + 6H_2O \leftrightarrow 4FeOOH(s) + 8H^+ \quad \textbf{(3-11)}$$

It should be pointed out that the oxidation of FeS resulted in the formation of H^+ ions, which can lead to a decrease in solution pH. Without the addition of tris buffer, under oxic conditions,

the solution pH decreased from initial 7.0 to 5.3, and thus, the removal percentage of Cd dropped dramatically to 71.3%.

For engineered remediation uses, it is desirable that the immobilized Cd remains stable without remobilization over prolonged periods. **Fig. 3-10** shows that immobilized Cd remained stable for 717 days when the suspension pH was maintained constant regardless of the DO condition. In fact, the Cd removal was increased from 91.9% to 96.1% under oxic conditions and from 93.4% to 96.6% under anoxic conditions. Long-term slow diffusion of cadmium into the nanopores of the nanoparticles could result in an increase in Cd uptake (Kramers, 1940). Meanwhile, the aging of amorphous iron oxides to energetically more stable phases may also contribute to the increased Cd uptake (Radha et al., 2010).

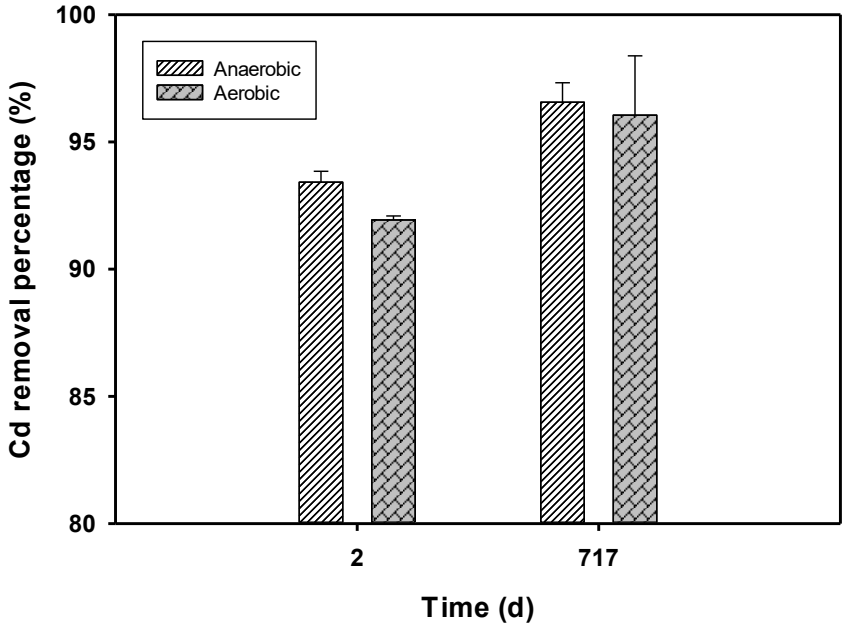

Fig. 3-10. Effects of dissolved oxygen on Cd uptake by CMC-FeS and long-term stability of immobilized cadmium. FeS = 100 mg/L, CMC-to-FeS molar ratio = 1.0×10^{-3}, initial Cd^{2+} = 1 mg/L, and pH = 7.00 ± 0.20.

3.4. Conclusions

This study demonstrated potential and viability of CMC-stabilized FeS nanoparticles for enhanced immobilization of Cd from contaminated water or groundwater. The primary findings are summarized as follows:

(1) Fully stabilized FeS nanoparticles were prepared at 100 mg/L FeS using 0.01 wt.% CMC, which showed much smaller size and greater specific surface area than bare FeS particles. FTIR analysis revealed that CMC molecules were attached to the surface of FeS nanoparticles by interactions between hydroxyl or carboxyl functional groups and Fe.

(2) The particle stabilization greatly enhanced equilibrium Cd removal from 69.1% to 95.8% when the CMC-to-FeS molar ratio was increased from 0 to 2.0×10^{-3}. However, further increasing the ratio from 2.0×10^{-3} to 3.9×10^{-3} diminished the Cd uptake by 3.8%.

(3) Sorption kinetic tests indicated a faster Cd removal rate of CMC-FeS compared with bare FeS. More than 93.4% Cd removal was achieved using 100 mg/L CMC-FeS (initial Cd = 1 mg/L, pH = 7.0) within 4 h. The kinetic data were adequately interpreted by a pseudo-second-order kinetic model. The rate constants for Cd removal by CMC-FeS and bare FeS were 6.68 and 0.78 $g \cdot mg^{-1} \cdot hr^{-1}$, respectively.

(4) XRD and FTIR analyses showed that chemical precipitation (CdS) and surface complexation between Cd and FeS were the key immobilization mechanisms. A dual-mode isotherm model incorporating chemical precipitation and surface complexation was able to

adequately interpret the equilibrium sorption data. The maximum Cd sorption capacity by CMC-FeS was determined to be 497.5 mg/g at pH 7.0.

(5) Cd uptake via CMC-FeS was enhanced with increasing pH from 4.0 to 8.0. HA may slightly inhibit Cd removal when HA concentration was increased from 0 to 3 mg/L as TOC, and the HA inhibitive effect was weakened when HA was increased from 3 to 10 mg/L as TOC. Oxygen had negligible effect on Cd uptake via CMC-FeS when pH was kept constant at 7.0.

(6) The immobilized Cd by CMC-FeS gradually increased when preserved for 717 days under both oxic and anoxic conditions when pH was kept at 7.0. The slight increase in Cd removal capacity can be attributed to the slow diffusion of Cd into the nanopores of the nanoparticles and the aging of amorphous iron oxides to energetically more stable phases.

Compared to other materials used for Cd removal or sequestration, CMC-stabilized FeS nanoparticles offer some unique advantages, including higher sorption capacity, faster kinetics, and long-term stability of immobilized Cd. The nanoparticles hold the potential to serve as an effective and environmentally friendly sorbent for *in situ* immobilization of Cd in contaminated water and soil.

Chapter 4. Comparing Three Stabilizers for Stabilizing FeS Nanoparticles: Performance and Effects on Immobilization of Cd

Fully stabilized ferrous sulfide (FeS) nanoparticles (100 mg/L) were prepared using 0.010 wt.% sodium carboxymethyl cellulose (CMC), 0.025 wt.% carboxymethyl starch (CMS), or 0.065 wt.% of a water-soluble starch. The batch kinetic tests showed that all stabilized FeS can rapidly remove >89% of Cd within 12 h (initial Cd = 1 mg/L and FeS dosage = 100 mg/L and pH = 7.0). The kinetic data were well interpreted by a pseudo-second-order rate model with rate constants of 0.15, 0.47, 0.78, and 6.68 $g \cdot mg^{-1} \cdot hr^{-1}$ for starch-FeS, CMS-FeS, bare FeS, and CMC-FeS, respectively. When pH increased from 4.0 to 8.0, the removal of Cd increased 25.8%, 34.4%, and 18.3% for CMC-FeS, CMS-FeS, and starch-FeS, respectively. When the 58.3 mg/kg Cd-laden soil was treated by 100 mg/L of CMC-FeS and CMS-FeS, the toxicity characteristic leaching procedure (TCLP) based Cd leachability reduced by 88.4% and 68.0%. After 55 pore volumes (PVs) of treatment using the nanoparticle suspensions and at an EBCT of 52.7 min, water-leachable Cd was reduced by 98.2% and 98.0%, respectively. The results further demonstrated that both CMC-FeS and CMS-FeS are promising materials for Cd immobilization in contaminated water and soil.

4.1. Introduction

Cadmium (Cd) as one of the most commonly detected toxic heavy metals in the environment is a big concern in soil contamination. The uncontrolled industrialization, unsustainable urbanization and intensive agricultural practices (Khan et al., 2017) results in the Cd concentration in soil increasing from a general concentration of 0.53 mg/kg to as high as 59.7 mg/kg (Liu et al., 2013). Cd released from natural sources and anthropogenic sources can reach to soil, and then

subsequently bio-accumulates in food crops. Exposure to elevated levels of Cd may cause damage of lung, kidney, bones and children's brain, cardiovascular disease, obstructive pulmonary disease, and even breast cancer. To mitigate human exposure, regulations are set up to limit Cd concentrations in soil. Cd is on the U.S. Environmental Protection Agency (EPA) National Emission Standards for Hazardous Air Pollutants (NESHAP) list of 189 hazardous air pollutants and is listed as one of 33 hazardous air pollutants that present the greatest threat to public health in urban areas (ATSDR, 2012). EPA biosolids rule states that the ceiling for the amount of Cd that can be applied to land is 85 mg/kg fill material (ATSDR, 2008).

Remediation of Cd contaminated soils via chemical extraction with both conventional and unconventional washing agents are widely used (Klik et al., 2020). Finding an environmentally friendly and cost-effective technique used for remediation of moderate to high Cd contaminated soil has broad research prospects. *in situ* immobilization of trace metals in the subsurface by delivering reactive nanoparticles into the contaminated source zones has been considered a promising soil remediation method (Gong et al., 2012; Liu and Zhao, 2007a; b; Xiong et al., 2009). Xiong et al. (2009) and Gong et al. (2012) prepared soil-deliverable FeS nanoparticles using carboxymethyl cellulose (CMC) as a stabilizer and observed that the CMC-stabilized FeS nanoparticles can effectively immobilize Hg^{2+} spiked in a marine sediment and field-contaminated soils from a New Jersey site and an Alabama site. FeS was proved to be an efficient sorbent to remove Cd compared with $Fe_3(PO_4)_2$ in previous work. Stabilized FeS nanoparticle was selected to study the *in situ* remediation technology application in Cd immobilization.

Stabilizers are used to prevent particles from aggregation and help to form nanoscale materials which are expected to offer much higher sorption capacity compared with non-stabilized particles due to their larger specific surface area, more active sorption sites, and higher surface

reactivity. CMC is a food grade, environment friendly and low-cost stabilizer which can function well in heavy metal immobilization by our group developed technology. Carboxymethyl starch (CMS) and soluble starch have similar physical and chemical properties. CMS is a water-soluble polysaccharide which is widely employed as an additive. It is biodegradable and non-toxic products, and can be used as thicker, binder and emulsifying agent in various applications. A starch is a complex polysaccharide made up of a large number of glucose units joined together by glycosidic bonds. Starch is an important food product and a versatile biomaterial which has a wide range of applications beyond the food industry, e.g., paper and board sector, the pharmaceuticals sector, the industrial binder sector, and the textile industry sector, *etc.* (Emeje and Blumenberg, 2020). CMS and starch were also selected as stabilizer in this study to compare with CMC.

The overall goal of this study is to evaluate the effectiveness of three stabilizers stabilized FeS nanoparticles for Cd immobilization in liquid and solid phase. The specific objectives are to: (1) prepare and optimize stabilized FeS nanoparticles using CMC, CMS, and starch; (2) compare the adsorption rate and capacity of the three types of stabilized FeS nanoparticles for the removal of Cd in water through batch kinetic tests; (3) examine the effect of pH on the Cd removal by stabilized FeS nanoparticles; and (4) investigate the effectiveness of the stabilized nanoparticles for Cd immobilization (defined as reduction in solubility and leachability) in an Alabama site soil sample.

4.2. Materials and methods

4.2.1. Materials

All chemicals used in this study were in the analytical grade or higher. Iron sulfate heptahydrate ($FeSO_4 \cdot 7H_2O$), cadmium chloride ($CdCl_2$), CMC (MW = 90 000 in the sodium form, degree of substitute = 0.7), and a water-soluble potato starch (hydrolyzed for electrophoresis) were

purchased from Acros Organics (Pittsburgh, PA, USA). CMS was purchased from Spectrum Chemical Mfg Corp (New Brunswick, NJ, USA). Sodium sulfide nonahydrate ($Na_2S \cdot 9H_2O$), sodium hydroxide (NaOH), and hydrochloric acid (HCl) were obtained from VWR International (Radnor, PA, USA).

The soil sample was collected from an Alabama site that is designated as both a Resource Conservation and Recovery Act (RCRA) facility and a National Priority List (NPL) site. Before use, the samples were sieved through a 2 mm screen. The salient properties of the soil were analyzed (Gong et al., 2012). It has 80% sand, 19% clay, and 1% soil organic matter (SOM), which was classified to be a sandy clay loam. The pH of the soil was 7.51. The cation exchange capacity was 4.6 meq/100 g. The hydraulic conductivity was 4×10^{-4} cm/s. It contained C (0.61%), N (0.04%), S (0.03%), Ca (557 mg/kg), K (45 mg/kg), Mg (134 mg/kg), Al (148 mg/kg), Fe (5170 mg/kg), Mn (28 mg/kg), Na (134 mg/kg), and Zn (2 mg/kg).

4.2.2. Preparation of stabilized FeS nanoparticles

A 150 mL suspension of CMC, CMS, or starch stabilized FeS nanoparticles was prepared in a 250 mL glass bottle following the previously reported procedure (Xiong et al., 2009). To prepare CMC-FeS, first, a 1 wt.% CMC stock solution was prepared. Then, 1.5 mL of the stock solution was added into 118.5 mL deionized (DI) water, and the mixture was purged with purified N_2 (>99%) for 15 min to remove dissolved oxygen (DO). Meanwhile, solutions of 8.5 mM $FeSO_4$ (20 mL) and 17.0 mM Na_2S (20 mL) were prepared with N_2-purged DI water. Under N_2 purging, the $FeSO_4$ solution (20 mL) was added to the CMC solution to yield a solution with 1.2 mM of Fe^{2+} and 1.08×10^{-2} wt.% of CMC. The mixture was then purged with N_2 for 5 min to assure complete mixing and formation of Fe^{2+}–CMC complexes. Then, the Na_2S solution (10 mL) was introduced into the solution dropwise under shaking at 150 rpm and vacuum through a burette at an Fe-to-S

molar ratio of 1:1. To ensure complete reaction, the system was shaken for another 5 min. The resultant nanoparticle suspension contained 100 mg/L FeS and 0.010 wt.% of CMC. For comparison, CMS-FeS and starch-FeS nanoparticles were prepared to contain 0.025 wt.% CMS and 0.065 wt.% starch but under otherwise identical conditions. The particles were then sealed and aged for 24 h before use.

The effects of CMC, CMS, and starch on the physical stability of FeS particles were examined by particle sedimentation tests. To this end, the FeS suspensions were allowed to age for 24 h and settle under gravity, and then 1 mL of the top supernatant was sampled and mixed with 4 mL of 12 M HCl for 5 min to completely dissolve the nanoparticles, and then analyzed for total Fe. Both Fe and Cd were measured by ICP-OES 710-ES (Agilent Technologies, Santa Clara, CA, USA) with detection limits of 1 μg/L and 0.1 μg/L, respectively. All measurements were conducted in duplicate, and data were reported as mean ± relative deviation from the mean.

4.2.3. Cadmium sorption kinetic tests

To compare the performance of three stabilizers, batch Cd sorption kinetic experiments were carried out with CMC-FeS, CMS-FeS, and starch-FeS nanoparticles in 50 mL Teflon vials under anoxic conditions. The reaction conditions were as follows: initial Cd concentration = 1 mg/L, FeS = 100 mg/L, pH = 7.00 ± 0.20 (maintained with HCl and/or NaOH), CMC = 0.010 wt.%, CMS = 0.025 wt.%, and starch = 0.065 wt.%. The mixtures were sealed and continuously mixed on an end-over-end rotator operated at 50 rpm at room temperature (20 ± 1 °C). At predetermined times, duplicate vials were sacrificially sampled. The samples were then filtered through the 25 nm membrane filters and analyzed for Cd concentration in the filtrates. Control tests were carried out with 0.010 wt.% CMC, 0.025 wt.% CMS, and 0.065 wt.% starch solution, and showed that loss of cadmium during the sorption and sample filtration was <2% in all cases.

4.2.4. pH effect

pH effect experiments were constructed following similar procedures to the kinetic tests where the systems were equilibrated for 48 h. The experimental conditions were: initial Cd concentration = 1 mg/L, FeS = 100 mg/L, CMC = 0.010 wt.%, CMS = 0.025 wt.%, starch = 0.065 wt.%, and the solution pH was adjusted to 4.0-8.0 using 1 M NaOH or 1 M HCl solution.

Dynamic light scattering (DLS) tests of the FeS particles with pH range from 4.0 to 8.0 were performed with a Malvern Zetasizer Nano ZS (Malvern Instruments, Worcestershire, UK) to yield number-weighted particle size distributions and zeta potentials. Solution viscosities were measured with a Gilmont falling-ball viscometer (Barnant Company, Barrington, IL, USA) and then used to correct for the influence of viscosity on the DLS measurements.

4.2.5. Soil spiked with Cd

For subsequent Cd immobilization tests with stabilized FeS nanoparticles, the soil was spiked with known concentrations of Cd following procedures described by Liu et al. (2007b). 50 mg/L $CdCl_2$ was added to the soil at a solution-to-solid ratio of 10:1 (mL/g) and at an initial pH 6.0. After mixing for 96 h, the soil suspension was centrifuged, and the supernatant was decanted. The remaining soil was washed three times with DI water to remove any traces of the original soluble Cd spike. The decanted supernatant was filtered through 0.45 μm mixed cellulose ester (MCE) membrane filter, and the concentration of Cd in the filtrate was analyzed. The Cd uptake by soil was calculated by comparing the initial and final concentrations of Cd in the aqueous phase. The resultant Cd concentrations in the soil was 58.3 mg/kg. The Cd-laden soil was then air-dried for future uses.

4.2.6. TCLP tests

Toxicity characteristic leaching procedure (TCLP) tests were performed following EPA Method 1311 to determine the leachability of Cd in the untreated and nanoparticle-amended samples. The nanoparticle-amended soils were obtained by mixing 2 g (dry weight) of the Cd-laden soil with 20 ml of CMC-FeS or CMS-FeS nanoparticles with the particle concentration of 100, 200, and 500 mg/L under anoxic conditions. The mixtures were then sealed and rotated on an end-to-end rotator at 50 rpm at room temperature (20 ± 1 °C). After 48 h, the samples were centrifuged at 6000g-force for 10 min to separate the solid and liquid. The soil samples were then air-dried for TCLP tests.

The TCLP tests were conducted by adding 1.2 g (dry weight) of untreated or nanoparticle-amended samples to 24 ml of fluid #1 (acetic acid, initial pH = 4.93). The mixtures were rotated at 50 rpm at room temperature (20 ± 1 °C) for 18 h and then centrifuged at 6000 g for 10 min. The supernatant was filtered through 0.45 μm MCE membrane filters. The concentration of Cd in the filtrate was analyzed and all tests were conducted in duplicate.

4.2.7. Deliverability of stabilized FeS nanoparticles

The *in situ* remediation technology requests the nanoparticles were deliverable into contaminated sediments or soils. The nanoparticle breakthrough tests were carried out through a fixed-bed column to probe the deliverability of stabilized FeS nanoparticles. The experimental setup included a Plexiglass column (10mm in diameter), an Accuflow Series I high pressure liquid chromatography stainless steel pump, and an Eldex automatic fraction collector. 14 g air-dried untreated soil (7.9 mL) was packed in the column and 100 mg/L CMC-FeS or CMS-FeS nanoparticles with pH 7 was introduced in the soil bed in an up-flow mode. A constant flowrate of 0.15 mL/min was maintained, which translated to an empty bed contact time (EBCT) of 52.7

min, and a superficial liquid velocity (SLV) of 0.11 m/h. Effluent samples were digested with 4 mL of 12 M HCl for 5 min to completely dissolve the nanoparticles, and then analyzed for total Fe. To acquire information on hydrodynamic behavior and dispersion characteristics of the soil, the breakthrough curve for a conservative tracer (50 mg/L KBr) were also conducted in the same manner. The Br^- concentration in effluent was measured by ion chromatography (IC) (Dionex, CA, USA) with an IonPac AS22 IC column.

4.2.8. Immobilization of Cd: fixed-bed column tests

In situ Cd immobilization were conducted by the fixed-column tests with the same experimental setup and procedure as described in **Section 4.2.7** except the soil packed in the column was 58.3 mg/kg Cd-laden soil. Nanoparticle-bound Cd and dissolved or free Cd in the aqueous phase were tested. The total Cd (both nanoparticle-bound and free Cd) was quantified by analyzing the whole samples, i.e., the collected samples were digested with 4 mL of 12 M HCl for 5 min to completely dissolve the nanoparticles and then analyzed for total Cd. The free Cd was quantified by analyzing the Cd concentration in the filtrates, i.e., the collected samples were filtrated using 25 nm MCE membrane filters to remove all CMC-FeS or CMS-FeS nanoparticles, and then analyzed to give the concentration of dissolved Cd. For comparison, control Cd elution tests were carried out using a 0.010 wt.% CMC or 0.025 wt.% CMS solution as the influent.

4.3. Results and discussion

4.3.1. Sorption kinetics of Cd by stabilized FeS nanoparticles

The particle sedimentation tests indicated that complete particle stabilization was achieved with 0.010 wt.% CMC, 0.025 wt.% CMS or 0.065 wt.% starch stabilized 100 mg/L FeS suspension, i.e., 100% of FeS nanoparticles remained suspended after 24 h gravity settling. Thus, these

stabilizer concentrations were considered optimal and was further tested in the subsequent experiments.

Fig. 4-1 shows Cd^{2+} removal kinetics by bare, CMC-stabilized, CMS-stabilized, and starch-stabilized FeS nanoparticles. The removal displays a rapid initial rate (89.5% of equilibrium capacity was achieved in the first 0.33 h by CMC-FeS, and 73.5%, 72.4%, and 74.9% in the first 1 h by CMS-FeS, Starch-FeS, and bare FeS particles, respectively), followed by a gradual phase till equilibrium at ~4 h for CMC-FeS and ~12 h for CMS-FeS, Starch-FeS, and bare FeS particles, which is consistent with the common notion that more accessible sites are occupied first (Axe and Anderson, 1995). At equilibrium, 93.4% of Cd was removed by CMC-FeS, compared to 92.0%, 91.0%, and 89.3% for CMS-FeS, Starch-FeS, and bare FeS, respectively. The faster removal rate and higher removal capacity of CMC-FeS compared to other stabilized FeS particles can be attributed the less CMC concentration. Denser stabilizer coating on the nanoparticles may inhibit access of Cd to the particles' surface sites due to elevated mass transfer resistance and/or blockage of the sorption sites (He and Zhao, 2008). Besides, CMC and CMS stabilized FeS have negative surface potential which are more favorable to interacting with the positively charged Cd^{2+} (**Fig. 4-3a**). The commonly used pseudo-second-order kinetic model was able to simulate the kinetic data (**Table 4-1**):

$$\frac{dq_t}{dt} = k_2(q_e - q_t)^2 \quad \textbf{(4-1)}$$

Integrate **Eq. 4-1** for the boundary conditions ($t = 0$, $q_t = 0$ and $t = t$, $q_e = q_t$) gives the **Eq. 4-2** below:

$$q_t = \frac{q_e t}{\frac{1}{k_2 q_e} + t} \quad \textbf{(4-2)}$$

where q_e and q_t are the amount of adsorbed Cd on the FeS particles (mg/g) at equilibrium and time t (h), respectively, and k_2 is the rate constant. The k_2 values were 0.15, 0.47, 0.78, and 6.68 $g \cdot mg^{-1} \cdot hr^{-1}$ for starch-FeS, CMS-FeS, bare FeS, and CMC-FeS, respectively, confirming the much faster Cd removal rate of CMC-FeS.

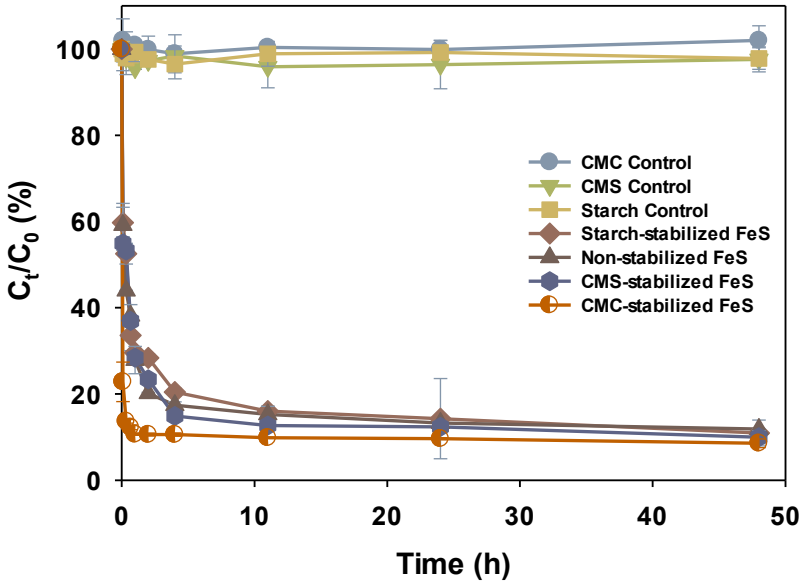

Fig. 4-1. Cd^{2+} sorption kinetics using bare, CMC-stabilized, CMS-stabilized, and starch-stabilized FeS particles. Initial Cd = 1 mg/L, FeS = 100 mg/L, CMC = 0.010 wt.%, CMS = 0.025 wt.%, starch = 0.065 wt.%, and pH = 7.00 ± 0.20.

Table 4-1. Best fitted kinetic parameters with pseudo-second-order kinetic model applied for simulating the sorption kinetics of cadmium removal by bare, CMC, CMS, and starch stabilized FeS particles (errors given as standard deviation).

Governing Equation	Parameters				
		Non-stabilized FeS	CMC-FeS	CMS-FeS	Starch-FeS
$q_t = \frac{q_e t}{\frac{1}{k_2 q_e} + t}$	q_e (mg/g)	13.42 ± 0.35	14.54 ± 0.03	13.80 ± 0.58	13.40 ± 0.46
	k_2 (g·mg^{-1}·hr^{-1})	0.78 ± 0.18	6.68 ± 0.34	0.47 ± 0.12	0.15 ± 0.04
	R^2	0.9668	0.9998	0.9348	0.9557

Note: q_e is the amount of sorbed Cd (mg/g) at equilibrium.

q_e and q_t are the calculated amount of sorbed Cd (mg/g) at equilibrium and time t (h), respectively.

k_2 is the rate constants of pseudo-second-order kinetic models.

R^2: correlation coefficient, which is calculated per the equation $R^2 = 1 - \frac{\sum_i (y_i - y_{i(predict)})^2}{\sum_i (y_i - \bar{y})^2}$, where y_i and $y_{i(predict)}$ are the original data values and model values, respectively, and $\bar{y}$ is the mean of the observed data.

4.3.2. pH effect

Fig. 4-2 shows the pH effect on Cd removal by CMC-FeS, CMS-FeS, and starch-FeS nanoparticles. The Cd uptake increased for all cases when pH increased from 4.0 to 8.0. The removal of Cd increased 25.8% for CMC-FeS (60.3% to 94.8%), 34.4% for CMS-FeS (73.0% to 98.8%), and 18.3% for starch-FeS (71.6% to 89.9%). The declined Cd removal at lower pH can be attributed to several factors. First, more of the FeS nanoparticles were dissolved at lower pH, and thus partial loss of the binding sites. Second, more CdS(s) was formed at higher pH as more free S^{2-} became available (pK_{a1} = 7.04, pK_{a2} = 11.96). Third, the increase of pH rendered more negatively charged surface of FeS, resulting in smaller paticles, larger specific area, and more favorable interactions with the Cd^{2+} cations. In addition, the Ostwald ripening process was more likely operative at lower pH, namely, smaller particles dissolved and redeposited onto larger particles, resulting in fewer but larger particles.

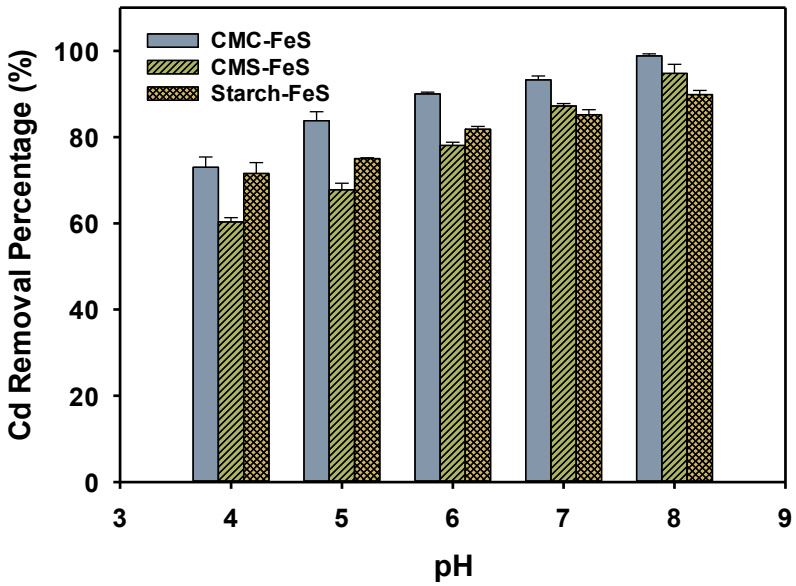

Fig. 4-2. Effects of pH on equilibrium cadmium removal by CMC-FeS, CMS-FeS, and starch-FeS. Initial Cd = 1 mg/L, FeS = 100 mg/L, CMC = 0.010 wt.%, CMS = 0.025 wt.%, starch = 0.065 wt.%.

The CMS stabilized FeS nanoparticles were more sensitive to pH changing while starch stabilized ones were more stable, which was confirmed by DLS-based particle size and zeta potential results (**Fig. 4-3**). **Fig. 4-3a** shows that, as pH increased from 4.0 to 8.0, the zeta potentials of CMC-FeS, CMS-FeS, and starch-FeS were more negative from -24.6 to -73.9 mV, -23.9 to -49.6 mV, 4.3 to -1.8 mV, respectively. **Fig. 4-3b** gives the DLS size of CMC-FeS (160.9-123.8 nm), CMS-FeS (350.8-142.0 nm), and starch-FeS (291.4-245.6 nm).

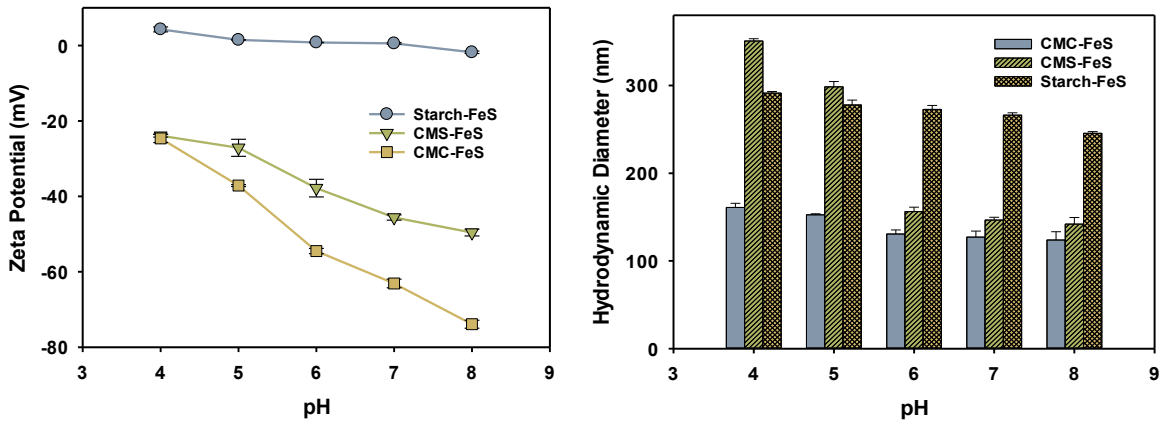

(a) (b)

Fig. 4-3. (a) Zeta potential and (b) DLS-based particle size for CMC-FeS, CMS-FeS, and starch-FeS as a function of pH. Initial Cd = 1 mg/L, FeS = 100 mg/L, CMC = 0.010 wt.%, CMS = 0.025 wt.%, starch = 0.065 wt.%.

The particle stabilization elevates Cd sorption capacity and removal rate. Taken together, the stabilizer recommend order is CMC > CMS > starch. Therefore, CMC-FeS nanoparticles were selected to study the *in situ* remediation of Cd-contaminated soil and groundwater. For comparison, CMS-FeS nanoparticles were also tested.

4.3.3. TCLP leachability of Cd

TCLP leachability of Cd tests were carried out to test the effectiveness of stabilized FeS nanoparticles for enhancing Cd^{2+} immobilization. **Fig. 4-4** shows that the TCLP leachable Cd for the untreated is 481.9 μg/L. When treated with 100 mg/L CMC-FeS and CMS-FeS, the leached Cd concentration was reduced to 56.1 μg/L (a 88.4% reduction) and 154.2 μg/L (a 68.0% reduction), respectively. Increasing the FeS dosage to 500 mg/L, the TCLP leachable Cd was further lowered 8 μg/L (CMC-FeS) and 36.1 μg/L (CMS-FeS). Besides, they were all lower than the maximum concentration of contaminants for toxicity characteristic of 1.0 mg/L regulated by EPA (EPA, 2009a). Increasing nanoparticle concentration was result in higher viscosity since FeS was coated with CMC or CMS (Mohamadiun et al., 2018). Therefore, 100 mg/L is an optimal dosage for both CMC and CMS stabilized FeS.

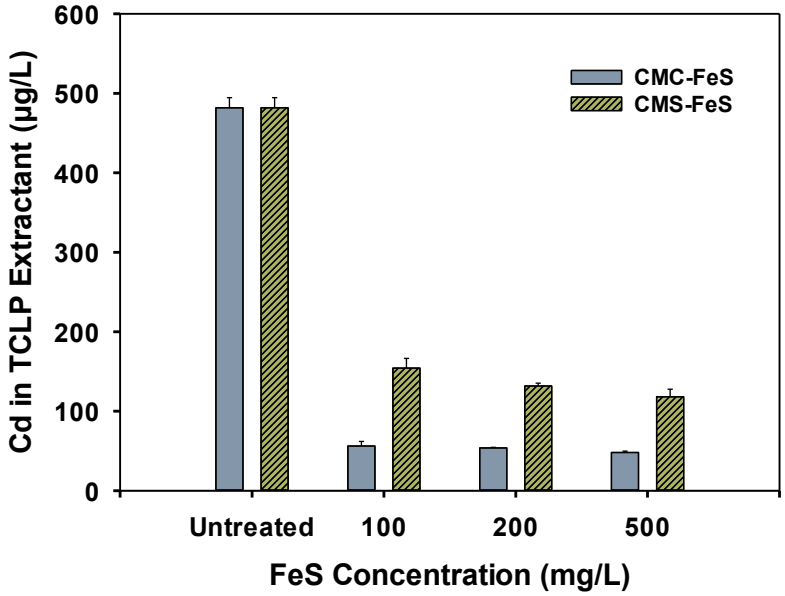

Fig. 4-4. TCLP leachability of Cd-laden soil before and after CMC-FeS and CMS-FeS nanoparticle treatments. Initial Cd spiked = 58.3 mg/kg, FeS = 100 mg/L.

4.3.4. Deliverability of stabilized FeS nanoparticles

Column breakthrough tests were carried out to demonstrate the deliverability of stabilized FeS nanoparticles in soil. **Fig. 4-5** shows that the full breakthrough of CMC-FeS occurred at around 4.5 pore volumes (PVs), compared to around 25.0 PVs for CMS-FeS and around 1.8 PVs for the KBr tracer. At the full breakthrough, ~30% of CMC-FeS or CMS-FeS in the influent consistently remained in the column during delivery period. It indicated that the stabilized nanoparticles could be delivered to the target contaminated zone and remained immobilized, especially when the external injection pressure is released (Gong et al., 2012). It not only *in situ* immobilized Cd, but also avoid nanoparticle-facilitated spreading of the contaminants. The CMC-FeS had a faster breakthrough profile compared to CMS-FeS may be due to the smaller particle

size and more negative surface charge. The spatial distribution of the retained FeS nanoparticles was gained by analyzing the Fe concentration eluted from different regions of the column. Both ~60% CMC-FeS and CMS-FeS particles stayed in the first 2.5 cm layer, which was a typical incipient filtration process.

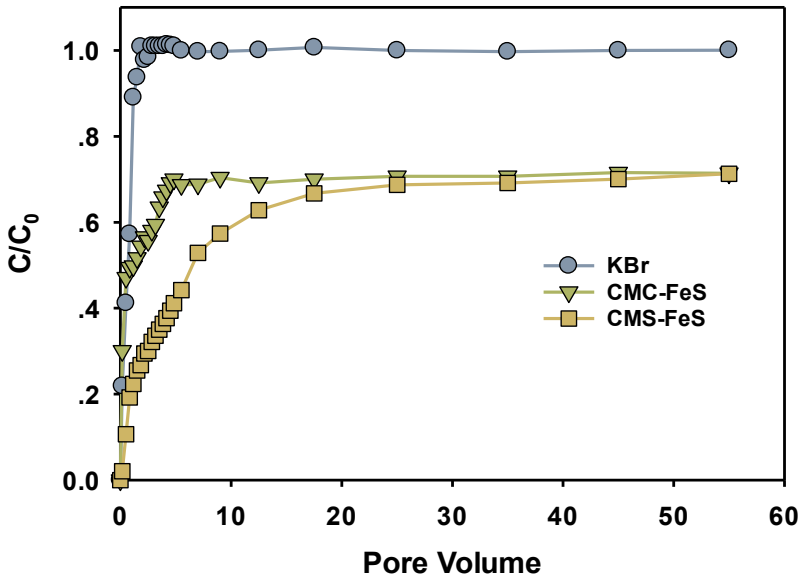

Fig. 4-5. Breakthrough curves of a tracer (KBr), CMC-FeS, and CMS-FeS nanoparticles. KBr = 50 mg/L, FeS = 100 mg/L, CMC = 0.010 wt.%, CMS = 0.025 wt.%, flowrate = 0.15 mL/min, EBCT = 52.7 min, SLV = 0.11 m/h.

4.3.5. Immobilization of Cd: fixed-bed column tests

Fig. 4-6a gives the information of total Cd (nanoparticle-bound Cd + free Cd) and free Cd leaking patterns pumped with 100 mg/L CMC-FeS suspension and 0.010 wt.% CMC solution. After 55 PVs, 12.6% of the Cd mass (816.2 μg in total) leached out from the soil. Among it, only

1.9% of Cd was free Cd. Namely, 100.9 μg Cd was bound to CMC-FeS and leached out, while only 2.0 μg Cd was mobile Cd. It confirms that CMC-FeS has strong affinity toward Cd (Tian et al., 2020) and the water-leachable Cd is immobilized by transferred from the soil to thermodynamically more stable nanoparticles (Gong et al., 2012). 0.010 wt.% CMC solution eluted 11.1% of Cd (90.6 μg) from the soil during the 55 PVs elution test, compared to 0.25% (2.0 μg) with the nanoparticle suspension, a 98.2% reduction in Cd leachability. 100 mg/L CMS-FeS suspension and 0.025 wt.% CMS solution were also tested for Cd leaking patterns in the same manner (**Fig. 4-6b**). After 55 PVs, 7.1% of the Cd mass (58.0 μg) leached out from the soil, while 0.22% of Cd (1.6 μg) was free Cd. 0.025 wt.% CMS solution eluted 9.6% of Cd (78.6 μg) from the soil during the 55 PVs elution test, compared to 0.22% (1.6 μg) with the nanoparticle suspension, a 98.0% reduction in Cd leachability. CMS and CMS-FeS had slower transport processes compared to CMC and CMC-FeS.

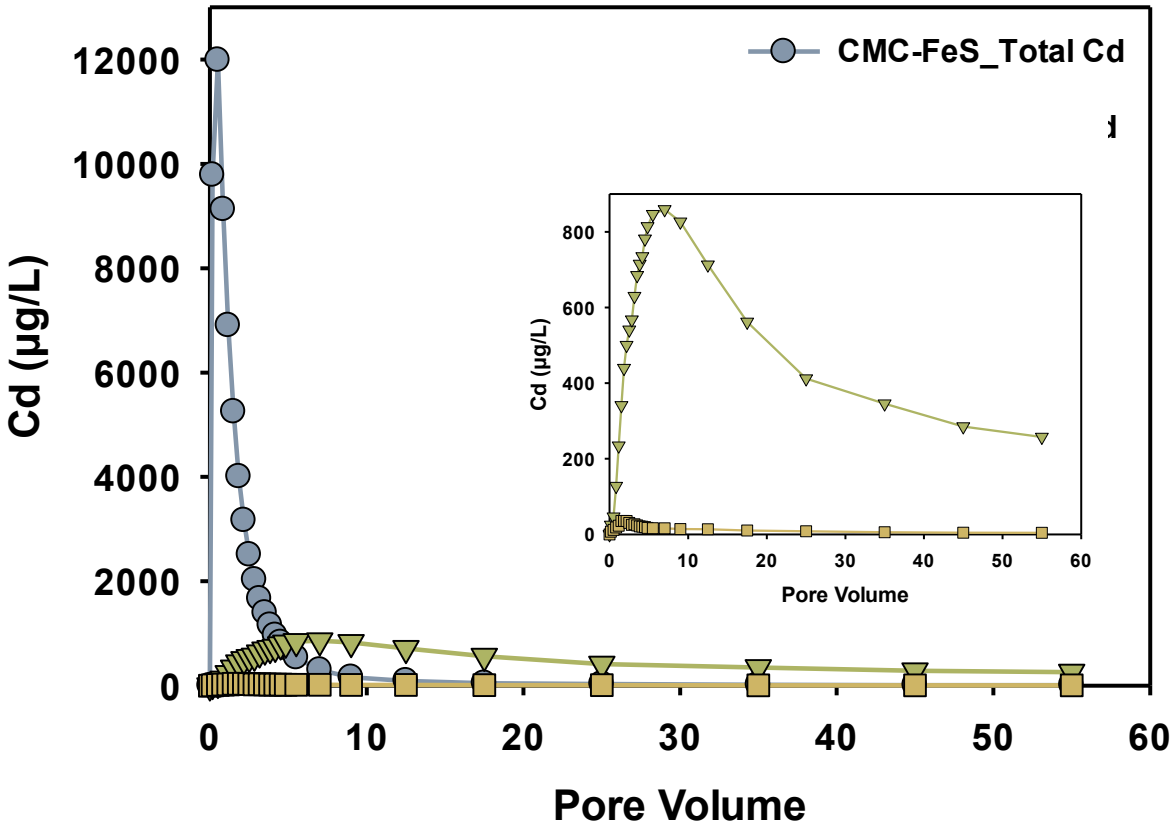
CMC-FeS_Total Cd
Cd (µg/L)
Pore Volume
12000
10000
8000
6000
4000
2000
0
0
10
20
30
40
50
60
800
600
400
200
0
0
10
20
30
40
50
60
Cd (µg/L)
Pore Volume

(a)

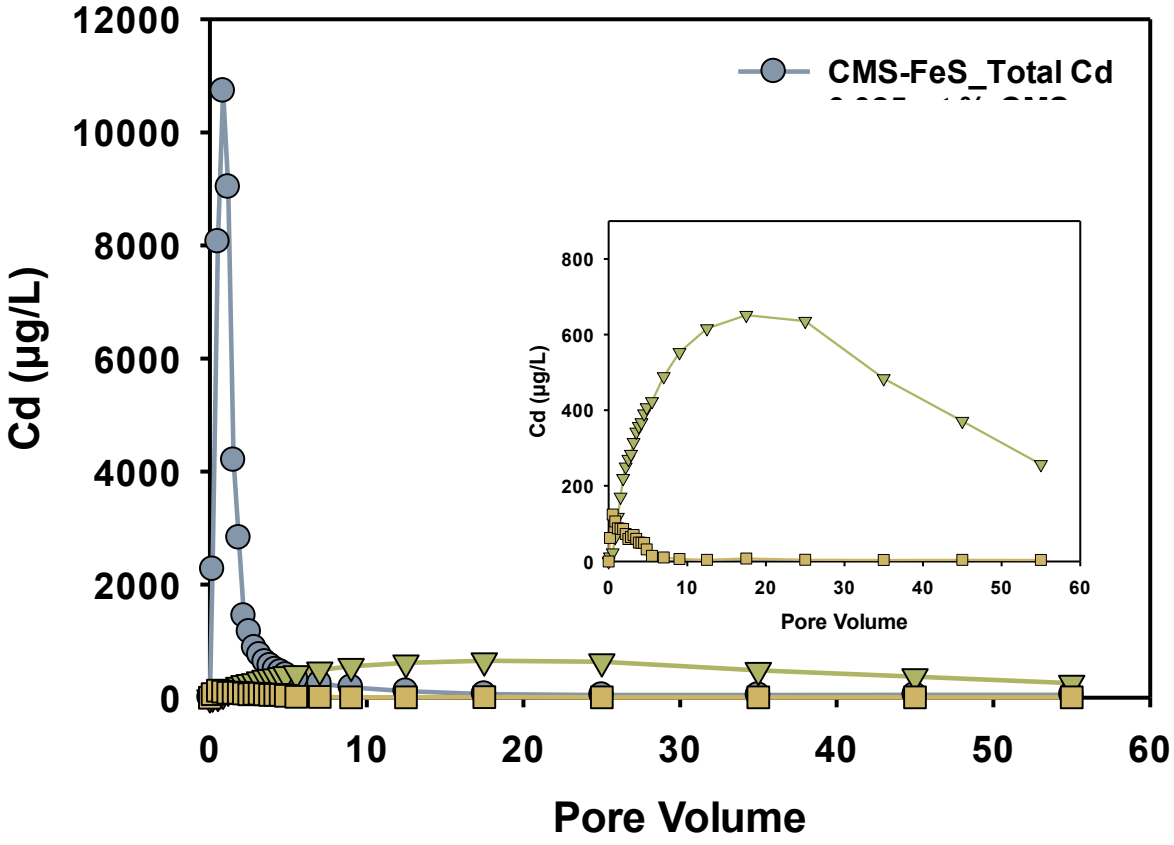

(b)

Fig. 4-6. Total and free Cd elution histories of Cd-laden soil injected with CMC-FeS and CMS-FeS nanoparticles. FeS = 100 mg/L, CMC = 0.010 wt.%, CMS = 0.025 wt.%, flowrate = 0.15 mL/min, EBCT = 52.7 min, SLV = 0.11 m/h. Inset: a close-up of dissolved Cd concentration histories

4.4. Conclusions

This study evaluated the effectiveness of stabilized FeS nanoparticles prepared using three different stabilizers for Cd immobilization in water and soil. The primary findings are summarized as follows:

(1) Fully stabilized FeS nanoparticles were prepared at 100 mg/L FeS using 0.010 wt.% CMC, 0.025 wt.% CMS, or 0.065 wt.% starch. Sorption kinetic tests indicated a faster Cd removal rate of CMC-FeS compared with CMS-FeS, starch-FeS, and bare FeS. CMC-FeS achieved the highest Cd removal percentage (93.4%) using 100 mg/L nanoparticles (initial Cd = 1 mg/L, pH = 7.0) within 4 h. The kinetic data were adequately interpreted by a pseudo-second-order kinetic model. The rate constants for Cd removal by CMC-FeS, CMS-FeS, and starch-CMC were 6.68, 0.47 and 0.15 $g \cdot mg^{-1} \cdot hr^{-1}$, respectively.

(2) Increasing pH from 4.0 to 8.0 enhanced Cd uptake for CMC-FeS, starch-FeS, and bare FeS particles.

(3) The CMC-FeS and CMS-FeS nanoparticles are highly effective for immobilizing Cd in soils, and were able to decrease TCLP-leachable Cd by 88.4% and 68.0% when a Cd-laden soil (58.3 mg-Cd/kg) was amended with 100 mg/L CMC-FeS and CMS-FeS suspensions, respectively.

(4) When the Cd-laden soil was treated by 55 PVs of the suspensions of 100 mg/L CMC-FeS and CMS-FeS nanoparticles at an EBCT of 52.7 min, water-leachable Cd were reduced by 98.2% and 98.0%, respectively.

These results showed that both CMC and CMS were effective stabilizers to stabilize FeS nanoparticles. Stabilized FeS nanoparticles could serve as an effective and environmentally friendly sorbent for *in situ* immobilization of Cd in contaminated water and soil.

Chapter 5. Removal of PFBA by Various Ion Exchange Resins: Effectiveness, Mechanisms, and Regeneration

Perfluorobutanoic acid (PFBA) is one of the most common short-chain PFAS. PFBA is persistent in the environment and has a high mobility in soil and water. While anion exchange resins have been known to be able to remove PFBA from water or wastewater, a systematic comparison of various types of resins has been lacking, as well as the effects of different resin matrices and functional groups. In this work, we tested two strong anion exchange resins (IRA900 and IRA958), one weak anion exchange resin (DOW 66), and one polymeric ligand exchanger (DOW 3N-Cu) for PFBA adsorption. The effects of resin properties, such as polymer matrix and functional group, the solution pH, and common inorganic and organic co-solutes were investigated. Batch kinetic tests showed that, after 120 h adsorption, IRA900, IRA958, DOW 66, and DOW 3N-Cu removed 93.8%, 70.7%, 94.3%, and 94.6% of PFBA (initial PFBA = 100 mg/L, resin dosage = 1 g/L, and pH = 7.0). The kinetic data were well interpreted by a pseudo-second-order rate model with rate constants of 0.06, 0.10, 0.07, and 0.19 $g \cdot mmol^{-1} \cdot hr^{-1}$, respectively, and the sorption isotherms were well simulated by the Freundlich isotherm model. Of the resins studied, IRA900 showed the best PFBA removal rate and capacity and was able to perform well over a broad pH range. The amount of PFBA sorbed on the resins was 1.16 times higher than the initial chloride ions released from the resins, indicating that the adsorption of PFBA involved both ion exchange and adsolubilization via hydrophobic interactions between PFBA and the hydrophobic resin matrix (polystyrene). This study also compared the effectiveness of different regeneration solutions, including the brine solution only, the organic solvent only, the mixture of a brine solution and an organic solvent or oil dispersant. Among the various regeneration recipes, the

mixture of 1% NaCl and 40% CH_3OH solution exhibited the best regeneration effectiveness and was able to recover about 90% of the capacity for all the four resins.

5.1. Introduction

Perfluorobutanoic acid (PFBA) is 4-C sort-chain per and polyfluoroalkyl substances (PFAS) which are not naturally occurring in the environment. PFBA is a breakdown product of other PFAS that are widely used in stain-resistant fabrics, paper food packaging, carpets, and manufacturing photographic film (EPA, 2021). Consequently, PFBA has been detected in food products, household dust, soils, and surface, ground, and drinking water. PFBA is more persistent and immobile in soil and water than other PFAS. Nowadays, PFBA is used as a safer alternative to legacy PFAS which can accumulate and remain in the human body over prolonged times (Jian et al., 2018), and can lead to various adverse health effects, such as low infant birth weight, thyroid hormone disruption, impairment on the immune system, and even cancer (EPA, 2017). Zhou et al. (2013) even found the PFBA concentration in Tangxun Lake, China was 47 800 ng/L. However, the toxicity for exposure to PFBA is still lacking. Weatherly et al. (2021) demonstrated that sustained dermal exposure to PFBA induces systemic effects and raised concerns of short-chain PFAS being promoted as safer alternatives. It has a great potential to study PFBA removal.

Adsorption is an effective method to remove PFAS. Adsorbents such as activated carbons, anion exchange resins, fluorinated clays, modified biomass, and β-cyclodextrin polymer have been used to remove PFAS, among which activated carbons and anion exchange resins are the most popular adsorbents. Using resin to adsorb PFAS is one of the practical ways in drinking or industry waste water treatment. Synthetic resins offer the advantages of controlled polymeric matrix, functional groups, and pore size distribution, though rather costly. As such, polymeric resins have been considered one of the most viable ways to remove PFAS in water treatments. Selective

removal of target PFAS may be achieved by selecting the most suitable resins or by tailoring the resin properties (matrix, functionality, and pore size). Polymeric resins can be divided into two types: ion exchange resins (with functional groups) and non-ion exchange or non-functionalized resins (without functionality). Senevirathna et al (2010), Xiao et al. (2012) and Du et al. (2015) tested the two types of resins for PFOA and PFOS removal, and observed that anion exchange resins offer much higher removal efficiency than non-functionalized resins, because of concurrent hydrophobic and electrostatic interactions. In general, short–chain PFAS are more favorably adsorbed by ion exchange resins because of their ability to access more ion exchange sites and ability to orientate their head groups for effective ion pairing with the fixed co-ions on the resin surface. In contrast, PFAS with longer tails exhibit higher hydrophobicity, and thus, can interact more strongly with the hydrophobic surface of non-functionalized resins (Maimaiti et al., 2018). For non-ion exchange resins, different polar properties could lead to different PFAS adsorption capacity. Xiao et al. (2012) found that moderately polar non-ionic Amberlite XAD-7HP performed better than the non-polar Amberlite XAD-2 resin in PFOA and PFOS removal. Besides the hydrophobic effect, the moderately polar non-ionic resins could offer charge–polar force and H-bonding to increase PFAS adsorption uptake while non-polar non-ionic resins couldn't (Xiao et al., 2012).

The pK_a of PFBA is 0.4 indicates that PFBA is anion form in the solution when pH is higher than 0.4 (Goss, 2008). In conclusion, anion exchange resins were selected as they could offer much higher removal efficiency in this study.

The objectives of this study are 1) condition three commercial ion exchange resins, including two strong-base anion (SBA) exchange resins (IRA900 and IRA958), and one weak-base anion (WBA) exchange resin (DOW 66), and prepare one polymeric ligand exchanger (PLE) (DOW 3N-

Cu), 2) test the removal rate and capacity of the resins for removal of PFBA through batch kinetic and isotherm experiments and column breakthrough measurements, 3) examine effects of the resin properties, such as polymer matrix and functional groups, the solution pH, and the presence of inorganic and organic matters on the PFBA uptake, 4) explore various regeneration strategies for the different type of resins by comparing various regenerants (brine, methanol, mixtures of brine and organic solvent, and oil dispersants), and 5) elucidate the adsorption and regeneration mechanisms.

5.2. Materials and methods

5.2.1. Materials

Perfluorobutanoic acid (PFBA) and HPLC grade methanol were purchased from VWR (USA). Four anion exchange resins including Amberlite IRA900, IRA958, DOW 66, and DOW 3N were purchased from Aldrich (Milwaukee, WI, USA), and their main properties are shown in **Table 5-1**. DOW 3N was used to prepare DOW 3N–Cu. The copper loading procedures used by Zhao and Sengupta (1998) were slightly modified. In brief, DOW 3N was first conditioned through cyclic acid and base washing using 1N HCl and 1N NaOH, respectively. Upon rinsing using DI water, the resin was equilibrated with 0.1% (w/w) copper solution at pH 3.5–4.0 for 2 weeks. Analytical grade $CuCl_2 \cdot 2H_2O$ (Aldrich, Milwaukee, WI, USA) was used for preparing the copper solution. The resin-to-solution ratio was approximately 1:200 (w/w). To enhance copper loading, the resin–solution mixture was intermittently heated at 70℃ for ~4h every other day and then placed back at ambient temperature (~21℃). (Note: Mild heating can cause resin swelling and enhance aging, thereby enhancing the copper loading kinetics and stability). To avoid oxidation of the resin matrix, nitrogen gas was purged in the solution during heating. Upon completion, the copper loaded resin was thoroughly rinsed using DI water and air dried for use. Other three resins were conditioned

following the same acid–base-washing procedure as described above. All resins were prepared in the chloride form. Other chemicals are of analytical grade.

Table 5-1. Properties of four resins used in this study.

Resin	Matrix	Porosity	Functional group
IRA900	Polystyrene	Macroporous	Quaternary ammonium
IRA958	Polyacrylic	Macroporous	Quaternary ammonium
DOW 66	Polystyrene	Macroporous	Polyamine
DOW 3N-Cu	Polystyrene	Macroporous	Bis-Picolylamine

5.2.2. PFBA sorption kinetic tests

Batch sorption experiments were carried out at 150 rpm and 25 °C in an orbital shaker for 122 h with 1 g of resin (IRA900, IRA958, DOW 66, and DOW 3N-Cu) in the flasks containing 1000 mL PFBA solution. All experiments were conducted twice, and the average value was adopted. The solution pH was adjusted to 7.0 ± 0.2 using 1 M NaOH solution in this study. The sorption kinetics experiments were conducted at the initial PFBA concentration of 100 mg/L. After the sorption experiments, the mixture was filtered with a 0.22 μm mixed cellulose ester (MCE) membrane. The control experiment indicated that the adsorption of PFBA on the membrane was negligible due to its high concentrations in solution.

5.2.3. PFBA sorption isotherm

The sorption isotherm experiments were conducted at the initial PFBA concentration ranging from 10 to 400 mg/L and the resin IRA900, IRA958, DOW 66, and DOW 3N-Cu concentrations is 1 g/L. The solution pH was adjusted to 7.0 ± 0.2 using 1 M NaOH solution. A LC-10ADvp HPLC with a CDD-6A conductivity detector and a TC-C18 column (4.6 × 250 mm) from Agilent Technologies (USA) was adopted to determine the concentrations of PFBA in aqueous solution. 55/45 (v/v) of methanol/0.02 M NaH_2PO_4 mixture was used as the mobile phase at 0.5 mL/min flow rate and the sample volume injected was 80 μL. In this study, the detection limit for PFBA is about 0.1 mg/L, and the amount of PFBA adsorption on the resins was calculated according to the difference of initial and equilibrium PFBA concentrations,

5.2.4. Effects of pH, HA, and co-existing ions

pH effect experiments were carried out at 150 rpm and 25 °C in an orbital shaker for 122 h with 0.2 g of resin (IRA900, IRA958, DOW 66, and DOW 3N-Cu) in the flasks containing 200 mL PFBA solution. The resin concentration is 1g/L. The solution pH was adjusted to 4-9 using 1 M NaOH or 1 M HCl solution. The sorption experiments were conducted at the initial PFBA concentration of 100 mg/L. The samples' PFBA concentration were measured.

Humic acid (HA) represented as the natural organic matter which is ubiquitous in groundwater. HA effect experiments were carried out at 150 rpm and 25 °C in an orbital shaker for 72 h with 0.1 g of IRA900 in the flasks containing 100 mL of 100 mg/L PFBA solution. The resin concentration was 1g/L. 0, 10, 20, 50, and 100 mg/L HA was added to the solution. The solution pH was adjusted to 7.0 ± 0.2 using 1 M NaOH solution.

Co-existing ions effects were studied under the same experimental conditions except for 1 mmol/L of chloride, nitrate, sulfate, bicarbonate, or phosphate was added to the solution. The

solution pH was adjusted to 7.0 ± 0.2 using 1 M NaOH solution. All experiments were conducted twice, and the average value was adopted.

5.2.5. PFBA-laden resins regeneration

A 0.02 g amount of PFBA-laden resin was added into 100 mL regeneration solution at pH 7 for SBA and pH 10 for WBA and PLE. The regeneration experiment was conducted at 150 rpm and 25 °C in an orbital shaker for 24 h. The PFBA concentration in solution was measured, and the regeneration percent was calculated.

5.2.6. Fixed-bed column tests

Both adsorption and regeneration patens in fixed-bed column were studied for future application in real water treatment. The optimal sorption and regeneration conditions are applied. The experimental setup included a Plexiglass column (10mm in diameter), an Accuflow Series I high pressure liquid chromatography stainless steel pump, and an Eldex automatic fraction collector. The breakthrough behavior of PFBA sorption was tested using IRA900 in a fixed-bed configuration. 1.68 g IRA900 was packed in the column and 100 mg/L PFBA with pH 7 was introduced in the resin bed in an up-flow mode. A constant flowrate of 1.20 mL/min was maintained, which translated to an empty bed contact time (EBCT) of 2.95 min, and a superficial liquid velocity (SLV) of 0.92 m/h. The regeneration of PFBA in a fixed-bed configuration was set up using 1.68 g PFBA-laden IRA900 (PFBA = 731.8 mg/g). 1% NaCl and 40% methanol regeneration solution with pH 10 was introduced in the resin bed in an up-flow mode. A constant flowrate of 0.20 mL/min was maintained, which translates to an EBCT of 17.67 min, and a superficial liquid velocity (SLV) of 0.15 m/h.

5.3. Results and discussion

5.3.1. Effect of resin properties

Generally, the properties of anion exchange resins mainly differ in three aspects including polymer matrix (e.g., polyacrylic and polystyrene structure), porosity (*e.g.*, gel–type and microporous), and functional group (*e.g.*, polyamine and quaternary amine), which not only influence the sorption capacity but also affect the sorption rate (Boyer and Singer, 2008; Gu et al., 2005; Li and Sengupta, 2000). Four resins were selected to investigate the effect of resin properties on the sorption kinetics of PFBA. As shown in **Fig. 5-1**, the pseudo-second-order kinetic model can describe the sorption kinetics of PFBA on the resins well according to the correlation coefficient (R^2), shown in **Table 5-2**. DOW 3N-Cu (PLE) had the highest sorption rate, which was 0.19 $g \cdot mmol^{-1} \cdot hr^{-1}$, compared to IRA958 (0.10 $g \cdot mmol^{-1} \cdot hr^{-1}$), DOW 66 (0.07 $g \cdot mmol^{-1} \cdot hr^{-1}$), and IRA900 (0.06 $g \cdot mmol^{-1} \cdot hr^{-1}$) when pH was 7. However, IRA900 had the highest adsorption capacity. The adsorption capacities of IRA900, DOW 66, DOW 3N-Cu, and IRA958 were 0.57, 0.54, 0.48, and 0.41 mmol/g, respectively. When the initial PFBA concentration was around 100 mg/L, these four resins perform similar. As the initial PFBA concentration increased, they became act differently. **Fig. 5-2** shows the PFBA sorption by four resins fit with Freundlich isotherm model. **Table 5-3** shows that Freundlich model has higher R^2 compared to Langmuir model, except DOW 66. In the higher initial PFBA range, IRA900 performed much better than other three resins. According to the Langmuir isotherm model fitting, the maximum PFBA sorption capacity of IRA900, DOW 66, IRA958, and DOW 3N-Cu were 16.27, 1.92, 1.70, 1.59 mmol/g, respectively. DOW 3N-Cu and IRA900 were optimal resins for lower and higher initial PFBA concentration range, respectively.

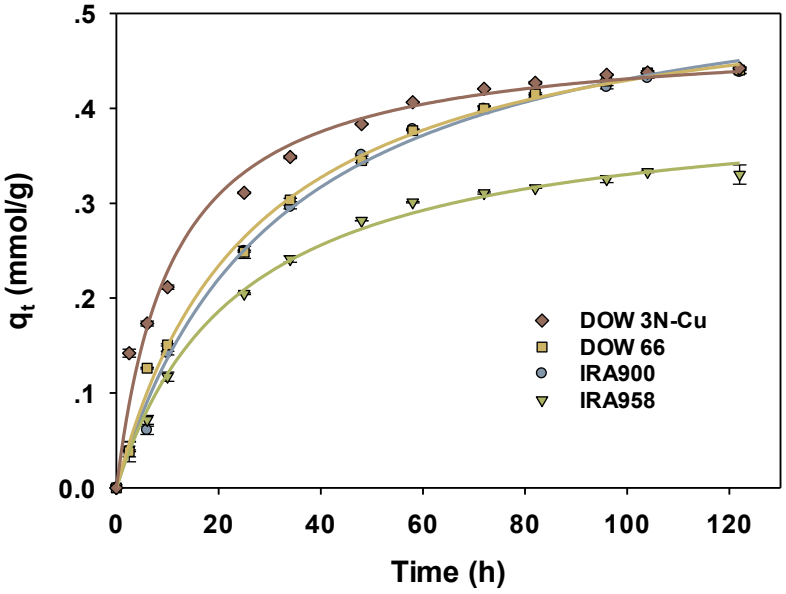

Fig. 5-1. PFBA sorption kinetics using IRA900, IRA958, DOW 66, and DOW 3N-Cu with pseudo-second-order kinetic fittings. Experiment conditions: initial PFBA = 100 mg/L, resin dosage = 1 g/L, and pH = 7.0 ± 0.2.

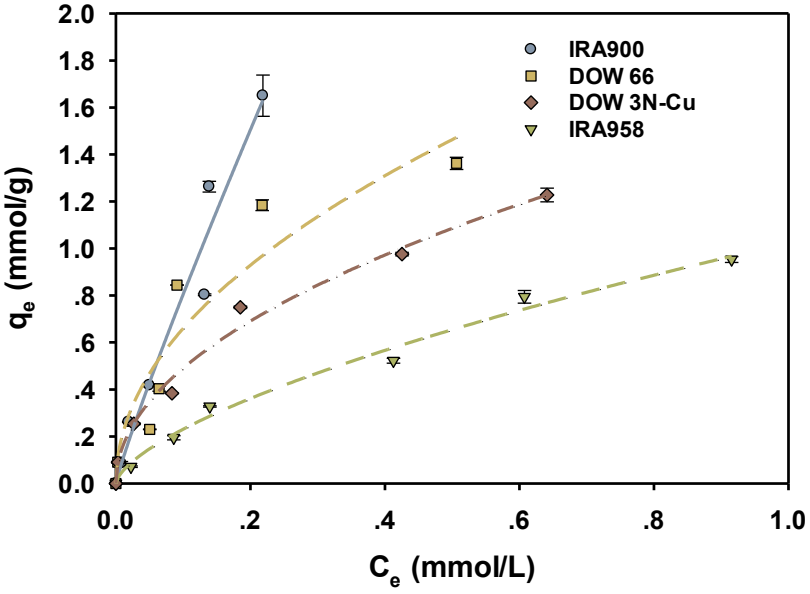

Fig. 5-2. PFBA sorption isotherm using IRA900, IRA958, DOW 66, and DOW 3N-Cu fit with Freundlich isotherm model. Experiment conditions: initial PFBA = 10 to 400 mg/L, resin dosage = 1 g/L, and pH = 7.0 ± 0.2.

Table 5-2. Best fitted kinetic parameters with various kinetic models applied for simulating the sorption kinetics of PFBA removal by IRA900, IRA958, DOW 66, and DOW 3N-Cu resins at pH 7 (errors given as standard deviation).

Kinetic Models	Governing Equation	Parameters				
			IRA900	**IRA958**	**DOW 66**	**DOW 3N-Cu**
Pseudo-first-order kinetic model	$q_t = q_e[1 - \exp(-k_1 t)]$	q_e (mmol/g)	0.44 ± 0.01	0.33 ± 0.00	0.44 ± 0.01	0.42 ± 0.01
		k_1 (hr^{-1})	0.03 ± 0.00	0.04 ± 0.00	0.04 ± 0.00	0.07 ± 0.01
		R^2	0.9977	0.9985	0.9910	0.9573
Pseudo-second-order kinetic model	$q_t = \frac{q_e t}{\frac{1}{k_2 q_e} + t}$	q_e (mmol/g)	0.57 ± 0.02	0.41 ± 0.01	0.54 ± 0.01	0.48 ± 0.01
		k_2 ($g \cdot mmol^{-1} \cdot hr^{-1}$)	0.06 ± 0.01	0.10 ± 0.01	0.07 ± 0.01	0.19 ± 0.03
		R^2	0.9958	0.9971	0.9963	0.9839

Note: q_e is the amount of sorbed PFBA (mmol/g) at equilibrium.

q_e and q_t are the calculated amount of sorbed PFBA (mmol/g) at equilibrium and time t (h), respectively.

k_1 and k_2 are the rate constants of pseudo-first-order and pseudo-second-order kinetic models.

R^2: correlation coefficient, which is calculated per the equation $R^2 = 1 - \frac{\sum_i (y_i - y_{i(predict)})^2}{\sum_i (y_i - \bar{y})^2}$, where y_i and $y_{i(predict)}$ are the original data values and model values, respectively, and $\bar{y}$ is the mean of the observed data.

Table 5-3. Langmuir and Freundlich isotherm model parameters for the sorption of PFBA by IRA900, IRA958, DOW 66, and DOW 3N-Cu resins at pH 7 (errors given as standard deviation).

Sorption Isotherm Model	Governing Equation	Parameters				
			IRA900	**IRA958**	**DOW 66**	**DOW 3N-Cu**
Langmuir	$q_e = \frac{bQC_e}{1 + bC_e}$	Q (mmol/g)	16.27 ± 43.37	1.70 ± 0.31	1.92 ± 0.35	1.59 ± 0.16
		b (L/mmol)	0.51 ± 0.38	1.35 ± 0.34	5.76 ± 1.68	4.49 ± 0.92
		R^2	0.9587	0.9841	0.9385	0.9833
Freundlich	$q_e = KC_e^{\frac{1}{n}}$	K	6.44 ± 1.84	1.02 ± 0.04	2.06 ± 0.36	1.53 ± 0.07
		n	1.11 ± 0.16	1.55 ± 0.11	2.02 ± 0.37	2.03 ± 0.14
		R^2	0.9603	0.9896	0.8997	0.9908

Note: q_e represents the total PFBA uptake (mmol/g).

C_e is the equilibrium concentration of PFBA in the solution phase (mmol/L).

Q is the Langmuir maximum sorption capacity (mmol/g).

b is the Langmuir constant (L/mmol) related to the adsorption energy.

K is the Freundlich constant related to adsorption capacity.

n is the heterogeneity factor indicating the adsorption intensity of the adsorbate.

Overall, polystyrene resins (IRA900, DOW 66, and DOW 3N-Cu) had higher adsorption rates and capacities. It is due to polystyrene matrix is more hydrophobic than the polyacrylic one (IRA958). Hydrophobic interaction is one of PFBA sorption mechanism. One evidence was that the amount of PFBA sorbed on the IRA900 was 1.16 times higher than the initial chloride ions released from the resins, indicating that the adsorption of PFBA involved both ion exchange and adsolubilization via hydrophobic interactions between PFBA and the hydrophobic resin matrix (polystyrene). PFBA sorption prefer polystyrene matrix, while Deng et al. (2010) showed that polyacrylic resin (IRA67) removed PFOS 10.8 times of polystyrene resin (IRA400). Microporous structure and short-chain PFAS may results in less important of intraparticle diffusion and size exclusion (Tan and Kilduff, 2007) compared to hydrophobic interaction.

Compared the PFBA sorption rates and capacity of IRA900 (SBA) and DOW 66 (WBA), functional group did not play an important role under the neutral or acid pH and lower initial PFBA concentration. The results of base pH sorption condition are discussed in **Section 5.3.2.**

5.3.2. Effect of solution pH

Clearly, strongly basic anion exchangers with polystyrene backbone would be more effective for PFBA removal from wastewater at acid pH. **Fig. 5-3** shows that the effect of solution pH on the sorption of PFBA on four resins. IRA900 and DOW 3N-Cu had high sorption capacity for PFBA (both averages were 0.44 mmol/g) in a wide pH range from 4 to 9. The sorption capacity of PFBA by IRA958, IRA900 and DOW 3N-Cu stayed steady. The PFBA uptake amount by DOW 66 decreased 15.8% when pH increased to 9, since most of amine groups on the resin had converted into the base form at high pH and lost the ability of anion exchange. Therefore, strongly basic anion exchange resins (i.e. IRA900) were more efficient in PFBA removal in all pH range.

Eq. 5-1 and **5-2** give the general ion exchange reactions for anion exchange resins with quaternary amine and polyamine groups during PFBA removal (Dudley, 2012).

$$[R_4N^+]Cl^- + PFBA^- \leftrightarrow [R_4N^+]PFBA^- + Cl^- \quad \textbf{(5-1)}$$

$$[R_3N] + H^+ + PFBA^- \leftrightarrow [R_3NH^+]PFBA^- \quad \textbf{(5-2)}$$

where $[R_4N^+]$ and $[R_3N]$ represents the ion exchange sites, (*i.e.*, the quaternary amine and polyamine groups, respectively) of a strong base and a weak base anion exchange resin. The pK_a of PFBA is 0.4 (Goss, 2008). The predominant PFBA species in the pH range is $PFBA^-$. Note the weak base exchange resins only work when the functional groups (i.e., the polyamine) are protonated at pH below the resin pK_a value (Dudley, 2012).

Consider of the conditions (pH and initial PFBA concentration, PFBA removal efficiency), IRA900 was selected for the following studies.

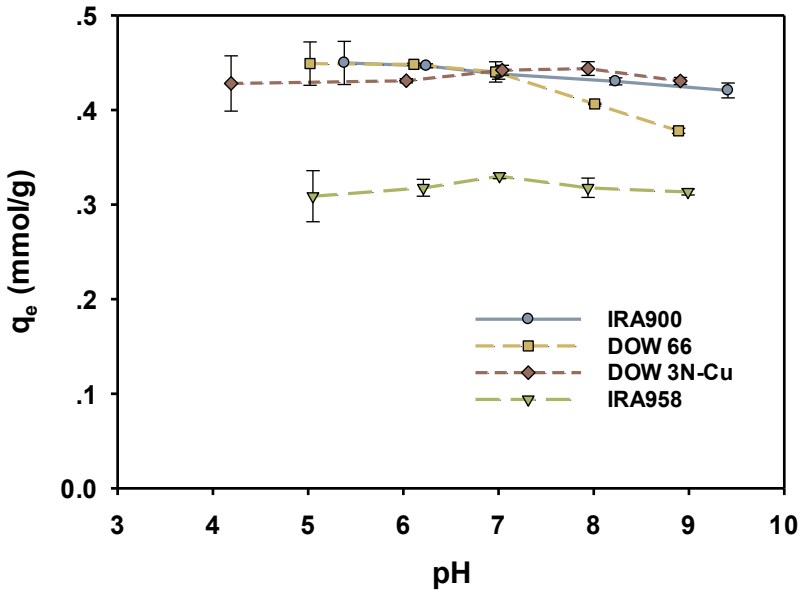

Fig. 5-3. pH effect of PFBA sorption by IRA900, IRA958, DOW 66, and DOW 3N-Cu. Experiment conditions: initial PFBA = 100 mg/L, resin dosage = 1 g/L.

5.3.3. Effect of HA and co-existing ions

To study the effect of organic and inorganic compounds effects to PFBA adsorption by resins, HA was selected as organic factor, and chloride, nitrate, sulfate, bicarbonate, and phosphate were selected as inorganic factors. **Fig. 5-4** shows that with the additional of 100 mg/L HA could reduce PFBA sorption amount by 11.4 %. The main mechanism of PFBA sorption is ion exchange. The anionic organic compound, HA, could compete with PFBA anion for anion exchange sites, which lead to the decrease of PFBA adsorption. The nonionic organic compounds barely affect the adsorption (Maimaiti et al., 2018).

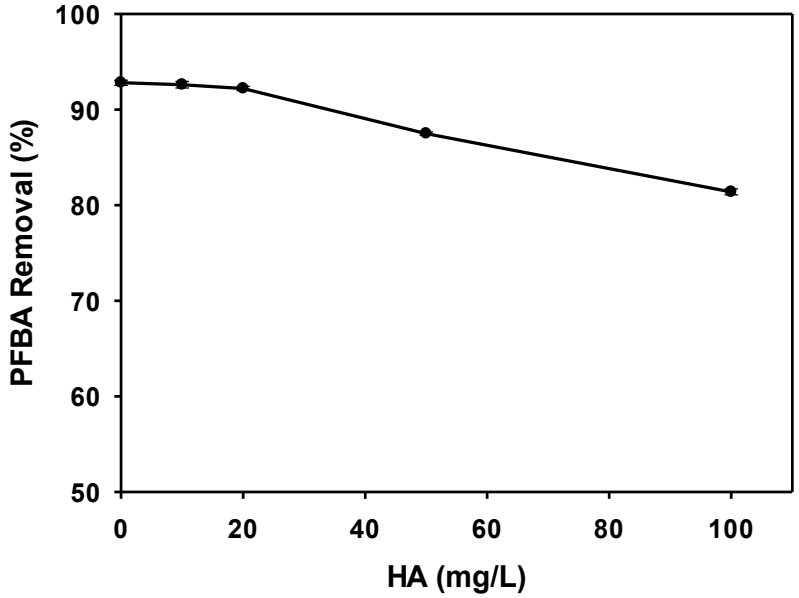

Fig. 5-4. HA effect of PFBA sorption by IRA900. Experiment conditions: initial PFBA = 100 mg/L, resin dosage = 1 g/L, HA = 0-100 mg/L, and pH = 7.0 ± 0.2.

Fig. 5-5 shows the effect of addition of 1 mmol/L Cl^-, NO_3^-, HCO_3^-, $H_2PO_4^-$, or SO_4^{2-} to PFBA sorption. HCO_3^- barely affect the sorption, while SO_4^{2-} had the strongest affect compared to other anions. 1 mmol/L SO_4^{2-}, $H_2PO_4^-$, NO_3^-, or Cl^- decreased PFBA uptake amount by 25.1%, 12.7%, 8.2%, and 7.7%, respectively. They could compete with $PFBA^-$ for anion exchange sites. These anions in high concentration may also introduce electrical double-layer compression (screening effect), which could reduce the surface net charge of adsorbent, and salting-out effects, which could decrease the solubility of PFAS, on the PFAS adsorption (Du et al., 2014).

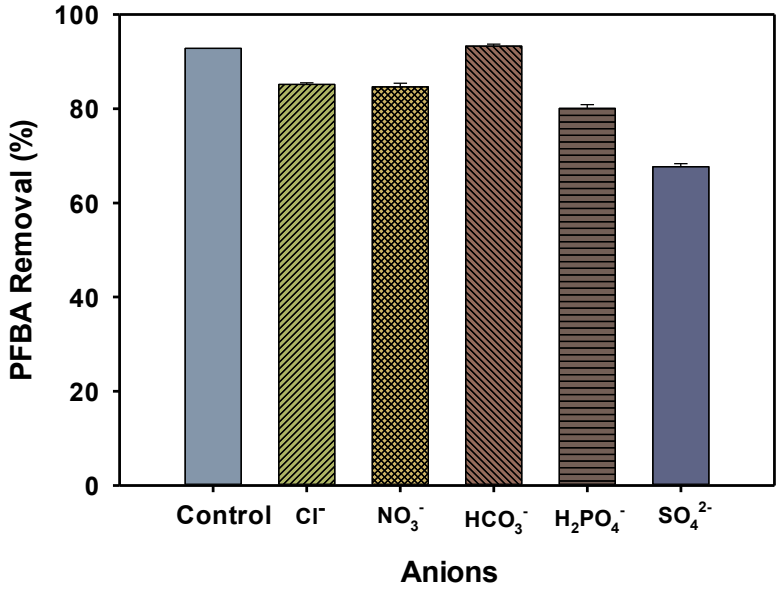

Fig. 5-5. Co-existing ions effect of PFBA sorption by IRA900. Experiment conditions: initial PFBA = 100 mg/L, resin dosage = 1 g/L, pH = 7.0 ± 0.2, and the addition of $[Cl^-]$, $[NO_3^-]$, $[HCO_3^-]$, $[H_2PO_4^-]$, or $[SO_4^{2-}]$ = 1 mmol/L.

5.3.4. Resin regeneration

Different regeneration solutions were studied on PFBA-laden IRA900. Four types of regenerants were included, which are the brine solution only, the organic solvent only, the mixture of a brine solution and an organic solvent/the dispersant. The dispersant was chosen because it was environmentally friendly and contained hydrophobic and hydrophilic parts which can easily separate oil and water. **Fig. 5-6** shows that for all resins, the resin regeneration percentages are 40% methanol < 1% NaCl + 180 mg/L SPC1000 (dispersant) < 1% NaCl < 1% NaCl + 40% methanol. When using 1% NaCl + 40% methanol to regenerate resins, the percentages for DOW 3N-Cu, IRA900, DOW 66, and IRA958 were 96.3%, 96.1%, 90.2%, and 89.8%, respectively. The commonly used regeneration solutions for resins, such as high concentration NaCl solution or methanol, were not effective for PFAS-sorbed resins. The anionic head of the PFAS molecule could be effectively desorbed by a brine solution from the resin ion exchange site, but the hydrophobic carbon-fluorine tail tended to stay adsorbed to the resin backbone. Meanwhile, hydrophobic tail could be effectively desorbed by an organic solvent, like methanol or ethanol, but the anionic head of the PFAS kept attached to the resin ion exchange site. Therefore, a mixture of inorganic and organic solvents should be used for an effective regeneration (Woodard et al., 2017). SPC1000 was failed to replace of methanol. Future works are needed to lower methanol volume or find a surrogate of methanol because of its toxicity.

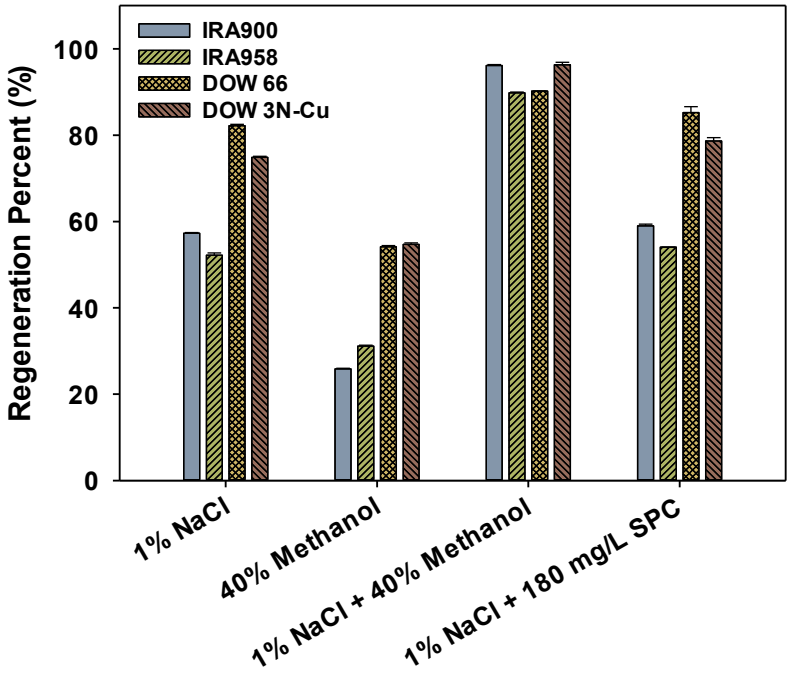

Fig. 5-6. Regeneration of the PFBA-laden IRA900, IRA958, DOW 66, and DOW 3N-Cu using different regeneration solutions. Experiment conditions: resin dosage = 0.2 g/L, contact time = 24 hours, pH = 10.0 ± 0.2.

5.3.5. Fixed-bed column tests

Fixed-bed column tests were taken placed because we can observation of high initial concentrations of percolates at low L/S ratios and predict the resin behavior in the field condition. **Fig. 5-7** shows the breakthrough curve of PFBA in the fixed-bed column experiments using IRA900 with pH 7. When < 4000 pore volumes (PVs), the PFBA concentration in effluent was lower than 5 mg/L. The column was fully breakthrough at 8000 PVs. Each gram of resin sorbed 731.8 mg PFBA, proved that IRA900 had a huge PFBA sorption capacity, compared to 19.1 mg/g for A600E, 29.5 mg/g for A520E, 52.3 mg/g for A532E (Zaggia et al., 2016), and 635.7 mg/g of

IRA910 (Maimaiti et al., 2018). The PFBA-laden resins were then dried and repacked in the column and feed with 1% NaCl + 40% methanol regenerant with pH 10. PFBA peak concentration (~8000 mg/L) reached at 2-6 PVs and 94.0% of PFBA was leached out within 80 PVs (**Fig. 5-8**). It confirmed the high efficiency of the regeneration solution made of 1% NaCl + 40% methanol.

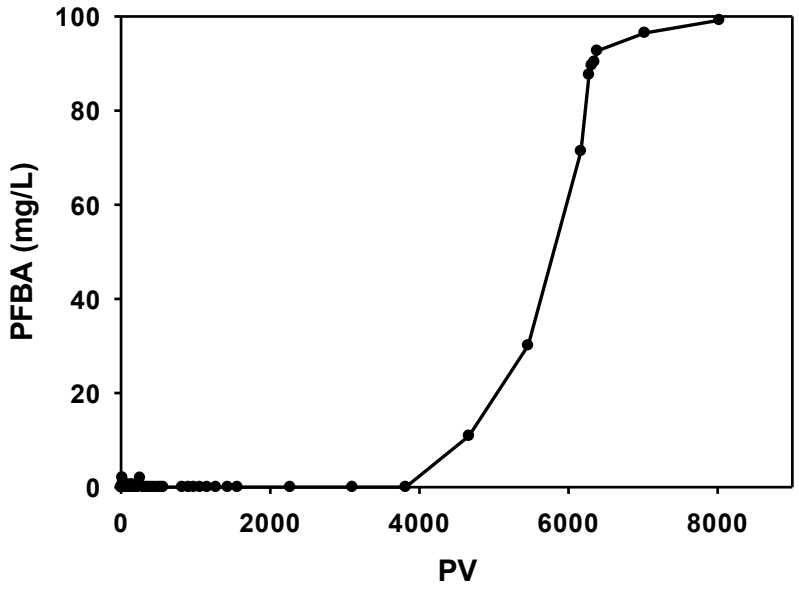

Fig. 5-7. Breakthrough curve of PFBA in IRA fixed-bed column. Experiment conditions: IRA900 = 1.68 g, PFBA = 100 mg/L, pH = 7.0 ± 0.20, flowrate = 1.2 mL/min, EBCT = 2.95 min, SLV = 0.92 m/h.

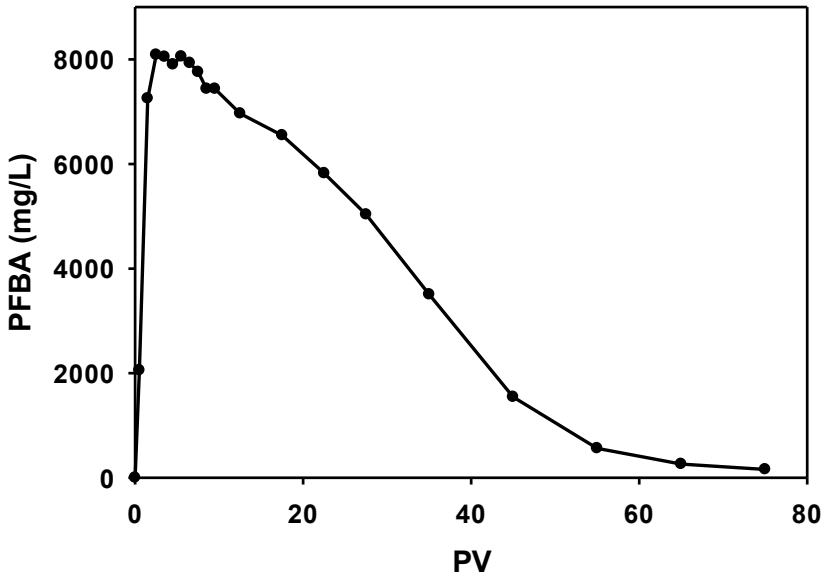

Fig. 5-8. Regeneration of the PFBA-laden IRA900 using 1% NaCl and 40% methanol regeneration solution. Experiment conditions: PFBA-laden IRA900 = 1.68 g, PFBA = 731.8 mg/g, pH = 10.0 ± 0.2, flowrate = 0.2 mL/min, EBCT = 17.67 min, SLV = 0.15 m/h.

5.4. Conclusions

This study revealed that anion exchange resins and a polymeric ligand exchanger were effective for PFBA sorption.

1. At pH 4-9, when initial PFBA concentration was lower than 100 ppm, DOW 3N-Cu was recommended for PFBA sorption; when initial PFBA concentration was higher than 100 ppm, IRA900 was recommended.
2. Polystyrene matrix is more favorable for PFBA sorption than polyacrylic matrix.
3. IRA900, IRA957, and DOW 3N-Cu can effectively remove PFBA over a broad pH range, while elevating pH from 7 to 9 reduced 15.8% of the PFBA uptake amount by DOW 66.

4. The presence of 100 mg/L HA reduced PFBA uptake by 11.4 %, whereas the presence of 1 mmol/L SO_4^{2-}, $H_2PO_4^-$, NO_3^-, or Cl^- decreased PFBA uptake amount by 25.1%, 12.7%, 8.2%, and 7.7%, respectively. The effect of HCO_3^- was negligible.
5. The mixture of 1% NaCl and 40% CH_3OH regeneration solution showed the best regeneration effectiveness and was able to recover about 90% of the capacity for all the four resins.
6. Column breakthrough tests showed that under the conditions of influent PFBA = 100 mg/L, pH = 7, and EBCT = 2.95 min, IRA900 was able to treat more than 4000 PVs of the high-strength PFBA-laden water, with full breakthrough occurring at 8000 PVs.
7. When the PFBA exhausted IRA900 was eluted with 1% NaCl and 40% CH_3OH (pH = 10, EBCT = 17.67 min), 94.0% of PFBA was leached out within 80 PVs.

Chapter 6. A 'Concentrate-&-Destroy' Technology for Enhanced Removal and Destruction of Per- and Polyfluoroalkyl Substances in Municipal Landfill Leachate

Per- and polyfluoroalkyl substances (PFAS) are ubiquitous in landfill leachate due to their widespread applications in various industrial and consumer products. Yet, there has been no cost-effective technology available for treating PFAS in leachate because of the intrinsic persistency of PFAS and the high matrix strength of landfill leachate. For the first time, we tested a two-step "Concentrate-&-Destroy" technology for treating PFAS from a model landfill leachate through bench- and pilot-scale experiments. The technology was based on an adsorptive photocatalyst (Fe/TNTs@AC), which was able to selectively adsorb PFAS despite the strong matrix effect of the leachate. Moreover, the pre-concentrated PFAS on Fe/TNTs@AC were effectively degraded under UV, which also regenerates the material. The presence of 0.5 M H_2O_2 during the photocatalytic degradation enhanced the solid-phase destruction of the PFAS. Fresh Fe/TNTs@AC at a dosage of 10 g/L removed >95% of 13 PFAS from the leachate, 86% after first regeneration, and 74% when reused three times. Fe/TNTs@AC was less effective for PFBA and PFPeA partially due to the transformation of precursors and/or longer-chain homologues into these short-chain PFAS. Pilot-scale tests preliminarily confirmed the bench-scale results. Despite the strong interference from additional suspended solids, Fe/TNTs@AC removed >92% of 18 PFAS in 8 h under the field conditions, and when the PFAS-laden solids were subjected to the UV-H_2O_2 system, ~84% of 16 PFAS in the solid phase were degraded. The "Concentrate-&-Destroy" strategy appears promising for more cost-effective removal and degradation of PFAS in landfill leachate or PFAS-laden high-strength wastewaters.

6.1. Introduction

Per- and polyfluoroalkyl substances (PFAS) have been manufactured since 1940s and have been used in numerous industrial and residential products, including fluoropolymeric surfactants, aqueous film-forming foams, metal plating, textile, and household products (Ahrens and Bundschuh, 2014). Landfills serve as the final repository for most of PFAS-laden spent materials. As a result, PFAS in the waste mass not only accumulate in landfills, but also leach out in the leachate, which can contaminate soil and waters. About 455 PFAS have been detected in the aquatic environment from 2009 to 2017, of which perfluorooctanoic acid (PFOA) and perfluorooctane sulfonic acid (PFOS) have been the most detected PFAS in drinking water worldwide (Wei et al., 2019). Due to the low molecular polarity, strong C-F bond energy (536 kJ/mol), long biological half-life (~3 years), and the amphiphilic nature, PFAS are uniquely persistent, bio-accumulative, and toxic in the environment.

According to a recent study by the Michigan Department of Environment, Great Lakes, and Energy (EGLE) and the Michigan Waste and Recycling Association (MWRA), PFOA and PFOS were detected at the μg/L or higher levels in all 32 active municipal solid waste landfills studied in the State (MWRA, 2019). In addition, the other frequently detected PFAS (at the ng/L to mg/L) in landfill leachate included perfluoroalkyl acids (PFAAs), fluorotelomer polymers (FTPs), perfluoroalkyl sulfonamide derivatives, and polyfluoroalkyl phosphate esters (PAPs). For instance, perfluoroalkyl carboxylic acids (PFCAs) and perfluoroalkyl sulfonic acids (PFSAs) have been reported in the U.S. landfill leachate at 10-8900 ng/L and 50-3200 ng/L, respectively. The broad concentration range is attributed to the diversity of the solid wastes, as well as the landfill age, climate conditions, and level of biological activities (Wei et al., 2019).

Human exposure to PFAS has been linked to cancers, elevated cholesterol, obesity, immune suppression, and endocrine disruption (Hu et al., 2016). Health concerns in the early 2000s prompted manufacturers in Europe and North America to phase out production of some long-chain PFAS (Land et al., 2018). To mitigate human exposure, the US Environmental Protection Agency (EPA) established an advisory level of 70 ng/L for PFOA and PFOS, individually or combined.

PFAS are resistant to various conventional water treatment processes, such as standard biological, Fenton, and photochemical processes (Vecitis, 2009). As such, intensive studies have been carried out in recent years to develop more cost-effective technologies for removal and preferably degradation of PFAS (mainly PFOS and PFOA) (Espana et al., 2015).

Sorption has been one of the most cited methods to remove PFAS from aqueous media, and to this end, various adsorbents have been investigated, including activated carbon (AC) (Franke et al., 2019), carbon nanotubes (Deng et al., 2012), ion exchange resins (Deng et al., 2010), synthetic magnetite nanoparticles (Gong et al., 2016), and biomaterials (Chen et al., 2011). However, these adsorbents bear with some critical drawbacks, in particular, the material regeneration, which not only requires costly and toxic organic solvents (e.g., methanol), but also generates large volumes of regenerant waste residuals. For instances, AC has been tested/used at several sites of the US Department of Energy to remove PFOA and PFOS from contaminated water; however, the cost-effectiveness of AC systems remains questionable due to costly regeneration and disposal of the spent regenerant. Moreover, while adsorption concentrates PFAS, it does do not degrade them.

Photocatalytic degradation of persistent organic pollutants (POPs), including PFAS, has gained strong momentum in recent years due to its high transformation efficiency and easy- and low-energy operation (Cambié et al., 2016; Schneider et al., 2014; Wang et al., 2017). Modified TiO_2-based materials and other catalysts (e.g., In_2O_3 and Ga_2O_3) have been shown promising for

the degradation of PFAS, while neat TiO_2 is less effective (Li et al., 2020a; Li et al., 2020b). However, because PFAS are usually present at trace concentrations (μg/L or ng/L levels) in contaminated waters or leachate, it's not energy-effective to directly treat large volumes of the liquid by photodegradation. To overcome this drawback, Li et al. (2020b) developed a "Concentrate-&-Destroy" technique, which can effectively adsorb and concentrate PFAS from water on to an adsorptive photocatalyst and then degrade the pre-sorbed PFAS by subjecting the PFAS-laden solids to UV irradiation (Li et al., 2020b). The key to this technology was a new type of iron-doped, carbon-modified composite (Fe/TNTs@AC) that serves as both an adsorbent and a photocatalyst. As an adsorbent, the material offers not only good adsorption rate, but also high adsorption selectivity towards PFAS, thanks to the concurrent hydrophobic interactions (between AC and PFAS tails) and Lewis acid-base interactions (between metal and PFAS head groups). As a photocatalyst, the material provides superior photocatalytic activity over conventional photocatalysts (e.g., TiO_2) owing to the carbon-mediated electron transfer and enhanced generation of reactive species.

Yet, degrading PFAS in landfill leachate is much more challenging than in water because of the complex matrices of leachate. Typically, landfill leachate contains high levels of dissolved substances, such as dissolved organic matter (DOM), chloride, sulfate, ammonium and metal ions, which can inhibit standard adsorption and photochemical degradation of PFAS. While membrane bioreactors, AC adsorption, and membrane filtration have been found to be able to remove PFAAs from leachates (Wei et al., 2019), their practical uses are limited by their high operating costs. Although ozone- and UV-based advanced oxidation processes (AOPs) have been pursued, the high strength of leachate matrices, particularly DOM, greatly inhibits the effectiveness of these processes.

To this end, the "Concentrate-&-Destroy" strategy may offer some unique advantages. First, the selective adsorption concentrates the target PFAS technique from bulk leachate onto a small volume of the material, minimizing the matrix interference with the subsequent photodegradation; and second, the pre-concentrating not only facilitates the photodegradation, but also allows for the use of other additional physico-chemical methods to enhance the degradation process, which would be cost-inhibitive when used for treating the bulk leachate.

Taking advantage of the high adsorption selectivity and photocatalytic activity of Fe/TNTs@AC, the overall goal of this study was to test the technical effectiveness of the "Concentrate-&-Destroy" technology for removal and degradation of PFAS in landfill leachate. The specific objectives were to: 1) characterize a model municipal solid waste (MSW) landfill leachate, 2) test the effectiveness of Fe/TNT@AC for adsorption and subsequent photocatalytic degradation of PFAS in the leachate and optimize the treatment conditions through bench-scale experiments; and 3) preliminarily pilot-test the treatment efficiency and material reusability under the field conditions.

6.2. Materials and methods

6.2.1. Chemicals

All chemicals were of analytical grade or higher. Nano-TiO_2 (P25, 80% anatase and 20% rutile) was purchased from Evonik (Worms, Germany). PFOA was obtained from Sigma-Aldrich (St. Louis, MO, USA). Sodium hydroxide (pellets) and Fe(II) chloride tetrahydrate were obtained from VWR International (Radnor, PA, USA). Filtrosorb-400® granular activated carbon (F-400 GAC) was acquired through the courtesy of Calgon Carbon Corporation (Pittsburgh, PA, USA) and was used as received. F-400 GAC was made of bituminous coal to achieve high density and high surface area for organic pollutant removal. Perfluoro-n-[1,2,3,4-$^{13}C_4$]octanoic acid ($13C_4$-

PFOA or M4PFOA) and Perfluoro-n-[1,2,3,4,5,6,7,8-$^{13}C_8$]octanoic acid ($^{13}C_8$-PFOA or M8PFOA) were purchased from Wellington Laboratories Inc. (Guelph, Ontario, Canada) and were used as isotopically labeled surrogate and internal standards.

6.2.2. Leachate sample collection and characterization

Leachate samples were collected from a confidential MSW landfill site in the State of Michigan, USA. The facility was built in 1960s and is still being actively operated. Leachates from all sections (closed areas, interim covered areas, and active areas) is all directed to an onsite leachate pretreatment system, which was designed to lower the concentrations of ammonium, metals, and DOM through a sequence of air stripping, chemical precipitation and biological degradation. **Fig. 6-1** gives the schematic of the treatment train. The ammonia stripping system was designed for use only when the aerated lagoons cannot achieve the discharge requirements. The pre-treated leachate was then discharged to an adjacent wastewater treatment facility for further treatment.

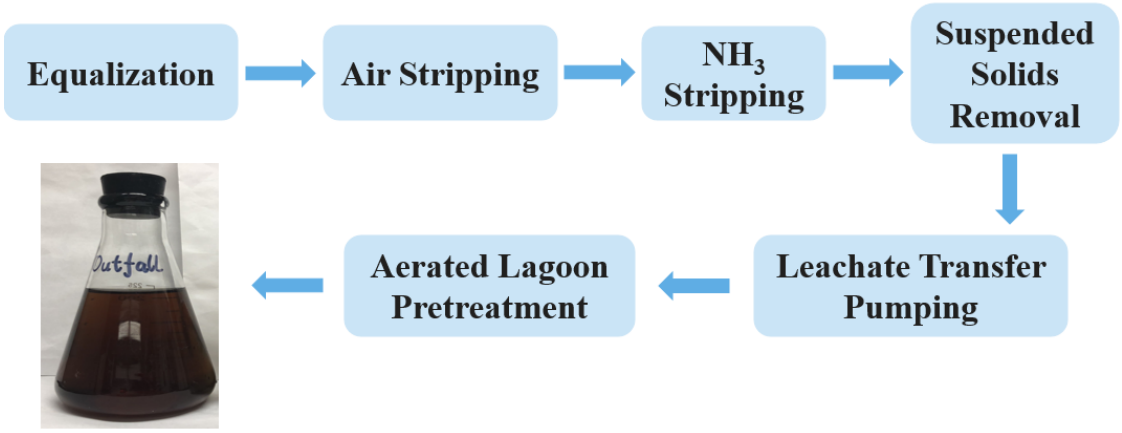

Fig. 6-1. Flow chart of the on-site leachate pretreatment system at the landfill site.

The leachate sampling procedure followed the Michigan General PFAS Sampling Guidance (EGLE, 2018). For the purpose of the study, leachate samples were collected at two locations: 1) an aboveground storage tank used to store the leachate collected from all waste areas before transmitting to the on-site leachate pretreatment system (samples are referred to as raw leachate); and 2) an outfall located after the on-site leachate pretreatment system before entering the sewer system connected to the wastewater treatment plant (designated as pre-treated leachate). The samples were kept in sealed containers at room temperature for 30 days, which allowed the gravity-settleable solids to be removed. The supernatant leachate samples were then shipped, on ice, to two National Environmental Laboratory Accreditation Program (NELAP)-certified laboratories (Eurofins TestAmerica Laboratories, Inc. of North Canton, Ohio and Vista Analytical Laboratory of El Dorado Hills, California) for analyzing PFAS and some common co-contaminants (**Section 6.2.6**).

6.2.3. Preparation of Fe/TNTs@AC

The adsorptive photocatalyst (Fe/TNTs@AC) was synthesized by integrating a commonly used AC and titanate nanotubes (TNTs) through a facile hydrothermal treatment approach (**Fig. 6-2**) (Li et al., 2020b; Liu et al., 2016). Typically, 7.8 g of TiO_2 was mixed with 7.8 g of F-400 GAC and then dispersed into 435.5 mL of a 10 M NaOH solution. After stirring for 12 h, the mixture was transferred into a 500 mL Teflon reactor and heated at 130 °C for 72 h. Then, the precipitates, *i.e.*, TNTs@AC, were washed with DI to neutral pH and dried in an oven at 105 °C for 24 h. Then, 15 g of dried TNTs@AC was well dispersed in 500 mL of DI water, and subsequently, 150 mL of an $FeCl_2$ solution (1 g/L as Fe, pH = 3.0) was added into the TNTs@AC suspension (Fe/TNTs@AC = 1 wt.%). The mixture was equilibrated for 12 h, and then left still for 1 h to allow the composite materials to settle by gravity (>99% of the particles settled). Then, the materials

were oven-dried at 105 °C for 24 h, and then calcined at 550 °C for 5.5 h under a nitrogen flow of 100 mL/min.

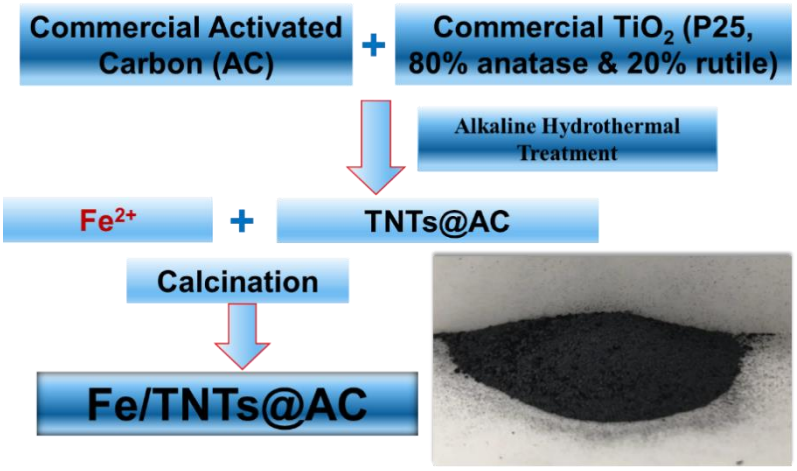

Fig. 6-2. Preparation of the adsorptive photocatalyst Fe/TNTs@AC (Li et al., 2020b).

6.2.4. Treatability study

6.2.4.1. Pre-oxidation of DOM in leachate by H_2O_2

To alleviate the potential inhibition of dissolved organic matter (DOM) on the performance of Fe/TNTs@AC for PFAS adsorption and photodegradation, laboratory studies were conducted to assess the feasibility of H_2O_2 for pre-oxidizing DOM and how the pre-treatment affects the subsequent PFAS adsorption and photodegradation. H_2O_2 was selected because it is a common oxidizing agent used for landfill leachate treatment (Hilles et al., 2016; Kurniawan and Lo, 2009; Wang et al., 2003). To this end, the onsite pre-treated leachate was amended using various dosages of H_2O_2 (0.1, 0.2, 0.5, 1.0 M) in 250 mL flasks by adding a known volume of H_2O_2 to 200 mL of the leachate. The bottles were then shaken at 100 rpm. At pre-determined times, 8 mL samples were taken and analyzed for DOM remaining (as total organic carbon, TOC). The treatment was

carried out both in the dark and under a simulated solar light to examine the effect of potential photochemical degradation. A 94041A solar simulator (Newport Corporation, Irvine, CA) was used as the light source (intensity = 100 mW/cm^2). All tests were carried out at least in duplicate.

6.2.4.2. Adsorption of PFAS in leachate by Fe/TNTs@AC

Batch adsorption kinetic tests were performed using 45 mL high-density polypropylene (HDPE) vials under the following experimental conditions: initial PFOA = 100 μg/L, material dosage = 5 g/L, pH = 8.5 (not adjusted), and temperature = 22 ± 1 ℃. To facilitate quick chemical analysis and a rapid preliminary evaluation of various treatment options, the onsite pretreated leachate sample was spiked with 100 μg/L of PFOA and used in the screening stage of the experiments. PFOA was selected as the probe compound because PFCAs were the dominant PFAS in the SCL leachate and PFOA is one of the two priority PFAS.

The adsorption tests were initiated by mixing a known mass of Fe/TNTs@AC with 40 mL of a leachate sample with or without the H_2O_2 pre-oxidation. The vials were kept in darkness and rotated at 60 rpm. At predetermined time intervals, duplicate vials were sacrificially sampled. Upon centrifugation for 3 min at 4000 rpm, 5 mL supernatants were collected and filtered through 0.22 μm poly(ether sulfones) (PES) membrane filters (~100% PFAS recovery), and filtrates were then analyzed for remaining PFOA. Meanwhile, another 8 mL filtered samples were analyzed for TOC remaining.

6.2.4.3. Photocatalytic degradation of PFAS in leachate by Fe/TNTs@AC

Batch photocatalytic degradation tests were carried out following the adsorption tests, which concentrated PFAS on a small volume of the composite material. After 2 h of the adsorption, the mixtures were centrifuged at 4000 rpm for 3 min to separate Fe/TNTs@AC from leachate. Upon removal of nearly 99% of the supernatant, the solid particles were transferred into a quartz photo-

reactor equipped with a quartz cover. Subsequently, 10 mL of DI water was added into the photo-reactor and the mixture pH was adjusted to 7.0 using a HCl solution (1 M). The photo-reactor was then placed in a Rayonet chamber UV-reactor (Southern New England Ultraviolet CO., Branford, CT, USA) operated at a wavelength of 254 nm and an intensity of 21 mW/cm^2. The mixture was mixed every 2 h during the photoreaction. The temperature of the photo-reactor was maintained at ~38 °C through a cooling fan inside the chamber of the UV-reactor.

At predetermined times (1, 8, 16, and 24 hours), the particles were separated through centrifugation, and then subjected to hot-methanol extraction as described by Li et al. (2020b), where M4PFOA was used as the surrogate standard to correct the mass recovery. The samples were filtered through 0.22 μm PES membranes, the filtrates were analyzed to figure out PFOA (or other PFAS) remaining in the solid phase. All tests were carried out in duplicate.

6.2.4.4. Effects of experimental conditions on solid-phase photodegradation of PFOA

Batch photodegradation kinetic tests were carried out to examine the effects of pH, H_2O_2, sodium persulfate, solid:liquid ratio, and temperature on the photodegradation of PFOA pre-concentrated on Fe/TNTs@AC.

First, PFOA and other PFAS were preloaded on Fe/TNTs@AC through the batch adsorption experiments using the PFOA spiked leachate. The experimental conditions were as follows: Fe/TNTs@AC = 0.2 g, leachate = 40 mL, pH = 8.5, equilibration time = 2 h. The PFAS-laden particles were then subjected to the UV irradiation following the same procedure as described above, but at various solution pH (5.0, 7.0, and 8.5), in the presence of various concentrations of H_2O_2 (0.1, 0.5, 1.0, and 1.5 M) or 0.2 M persulfate, or at different solid:liquid ratios (0.2:5, 0.2:10, and 0.2:15 g:mL) in the photo-reactor. To test combined effects of temperature and H_2O_2 or

$Na_2S_2O_8$, the experiments with 0.5 M H_2O_2 or 0.2 M $Na_2S_2O_8$ were also carried out with the cooling fan of the photo-reactor turned off, which resulted in a chamber temperature of ~65 °C.

6.2.4.5. Fe/TNTs@AC reusability tests

The photodegradation of PFAS-laden Fe/TNTs@AC was expected to regenerate the material for repeated uses. To test the reusability, two rounds of adsorption-photodegradation/regeneration tests were performed using the PFOA-spiked leachate. The adsorption tests were performed following the procedures described in **Section 6.2.4.2** under the following experimental conditions: initial PFOA = 100 μg/L, material dosage = 5 g/L, pH = 8.5, and temperature = 22 ± 1℃. After 2 hours of adsorption, the PFOA-laden Fe/TNTs@AC was subjected to the photodegradation/regeneration process and under the following experimental conditions: pH = 7.0, $[H_2O_2]$ = 0.5 M, and solid:liquid = 0.2:10 g:mL. After 24 hours of catalytic photodegradation, the regenerated materials were reused in another round of the adsorption-photodegradation tests under the same conditions.

Building upon the results from the screening experiments, bench-scale adsorption and photodegradation tests were performed to treat the original PFAS from both the raw and onsite pre-treated leachate samples. Fourteen PFAS in the leachate were followed. Adsorption kinetic tests were carried out under the following conditions: Fe/TNTs@AC = 5 or 10 g/L, leachate = 120 mL, and pH = 8.5. Following 4 hours of adsorption, the PFAS-laden Fe/TNTs@AC was subjected to the photodegradation under the following conditions: pH = 7.0, $[H_2O_2]$ = 0.5 M, solid:liquid = 0.2:10 g:mL. After 24 hours of photocatalytic photodegradation, the regenerated material was reused in two more consecutive cycles of the adsorption-regeneration runs.

6.2.5. Preliminary pilot-scale experiments

Building upon the bench-scale experimental results, pilot-scale experiments were carried out at the landfill site to further evaluate the technology towards future field applications. A pilot-scale batch reactor and a chamber UV reactor were designed and constructed for the pilot study (**Fig. 6-3**). The batch reactor consists of a 15-gallon open-top, cone-bottom tank and a portable Tamco mixer (U.S. Plastic Corporation, Lima, OH, USA). The UV reactor consists of a chamber equipped with six 4-ft long UV (254 nm) fluorescent lamps (Larson Electronics LLC, Kemp, TX, USA). The total intensity of the lamps was 6.9 mW/cm^2 at a 10-in distance.

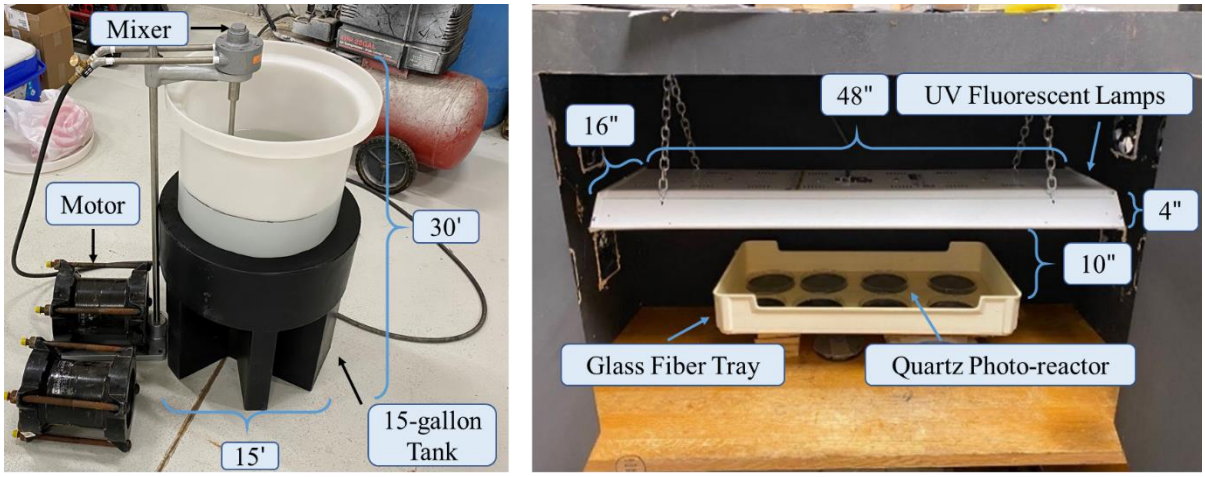

(a) **(b)**

Fig. 6-3. (a) Pictures of a completely stirred batch reactor for pilot-scale adsorption of PFAS from landfill leachate and (b) a chamber UV reactor for pilot-scale photocatalytic degradation of PFAS pre-adsorbed on Fe/TNTs@AC.

The adsorption kinetic tests were carried out under the following conditions: Fe/TNTs@AC = 10 g/L, leachate volume = 37.85 liters (10 gallons), pH = 6.5. At predetermined time intervals

(1, 4, and 8 hours), leachate samples were collected for analyzing various PFAS remaining in the aqueous phase. Following the adsorption tests, the PFAS-laden Fe/TNTs@AC was separated via gravity settling and then transferred into the UV reactor (**Fig. 6-3b**) under the following experimental conditions: pH = 7.0, [H_2O_2] = 0.5 M, and solid:liquid = 0.2:10 g:mL. After 72 hours of catalytic photodegradation, the regenerated material was reused in another round of the adsorption-regeneration runs.

6.2.6. Analytical methods

TOC was analyzed on a TOC analyzer (model TOC-L; Shimadzu, Kyoto, Japan). Leachate pH was determined using a pH meter (PH800 Digital, Apera Instruments, US). Samples involving spiked PFOA were analyzed via an ultra-performance liquid chromatography system coupled with a quadrupole time-of-flight mass spectrometer (UPLC-QTOF/MS) with electrospray ionization (ESI), which was operated in the negative mode and with the Masslynx software (V4.1) (ACQUITY, Waters Corp., USA) (Li et al., 2020b). The instrument detection limit for PFOA was 1.0 μg/L.

Table 6-1 gives the analytes and analytical methods used by the two external certified analytical companies. **Table 6-2** lists the acronyms of the PFAS detected in the landfill leachate. All PFAS in the landfill leachate were analyzed via an ultra-performance liquid chromatography-tandem mass spectrometer (UPLC-MS/MS). **Table 6-3** gives the method detection limits for the PFAS analyzed.

Table 6-1. The analytes of leachate and the analytical methods.

Analytical Laboratory	Analytes	Analytical Methods
Vista Analytical Laboratory	PFBA	Modified USEPA Method 537
	PFBS	
	PFPeA	
	PFPeS	
	PFHxA	
	PFHxS	
	4:2 FTS	
	PFHpA	
	PFHpS	
	PFOA	
	PFOS	
	6:2 FTS	
	PFOSA	
	PFNA	
	PFNS	
	PFDA	
	PFDS	
	8:2 FTS	
	PFUnA	
	MeFOSAA	

	PFDoA	
	EtFOSAA	
	PFTrDA	
	PFTeDA	
Eurofins TestAmerica Laboratories	Chloride	USEPA Method 9056A
	Fluoride	
	Sulfate	
	Ammonia	Method 4500 NH3 C-2011
	Nitrate-nitrite as nitrogen	USEPA Method 353.2
	Total phosphate	Method SM4500 P E-2011
	Total dissolved solids (TDS)	Method SM 2540C
	Total suspended solids (TSS)	Method SM 2540D
	Iron	USEPA Method 6010C
	Magnesium	
	Manganese	
	Calcium	
	Potassium	
	Sodium	
Auburn University	pH	Method 9040C
	Total organic carbon (TOC)	Method 9060A

Table 6-2. A list of acronyms for PFAS detected in a model landfill leachate.

PFBA	Perfluorobutanoic acid
PFBS	Perfluorobutanesulfonic acid
PFPeA	Perfluorophosphonic acid
PFPeS	Perfluoropolyethers
PFHxA	Perfluorohexanoic acid
PFHxS	Perfluorohexane sulfonate
4:2 FTS	4:2 Fluorotelomer sulfonic acid
PFHpA	Perfluoroheptanoic acid
PFHpS	Perfluoroheptanesulfonic acid
PFOA	Perfluorooctanoic acid
PFOS	Perfluorooctane sulfonate
6:2 FTS	6:2 Fluorotelomer sulfonic acid
PFOSA	Perfluorooctanesulfonamide
PFNA	Perfluorononanoic acid
PFNS	Perfluorononanesulfonic acid
PFDA	Perfluorodecanoic acid
PFDS	Perfluorodecanesulfonic acid
8:2 FTS	8:2 Fluorotelomer sulfonic acid
PFUnA	Perfluoroundecanoic acid
MeFOSAA	N-Methylperfluorooctane sulfonamidoacetic acid
PFDoA	Perfluorododecanoic acid

EtFOSAA	N-ethyl-perfluorooctane sulfonamido acetic acid
PFTrDA	Perfluorotridecanoic acid
PFTeDA	Perfluorotetradecanoic acid

Table 6-3. Method detection limit (MDL) and method reporting limit (MRL) for various PFAS analyzed by Vista Analytical Laboratory (with isotope dilution and 125 mL extraction).

	Analyte	**MDL (ng/L)**	**MRL (ng/L)**
1	PFBA	0.729	4
2	PFBS	1.79	4
3	PFPeA	1.28	4
4	PFPeS	2.42	4
5	PFHxA	2.18	4
6	PFHpA	0.591	4
7	4:2 FTS	1.39	4
8	PFHpA	0.591	4
9	PFHpS	0.937	4
10	PFOA	0.651	4
11	PFOS	0.807	4
12	6:2 FTS	2	4
13	PFOSA	1.77	4
14	PFNA	0.81	4
15	PFNS	3.87	4

16	PFDA	1.49	4
17	PFDS	1.23	4
18	8:2 FTS	2.06	4
19	PFUnA	1.05	4
20	MeFOSAA	1.65	4
21	PFDoA	0.792	4
22	EtFOSAA	1.37	4
23	PFTrDA	0.494	4
24	PFTeDA	0.755	4

To avoid potential matrix interferences with the PFAS analysis, solid phase extraction (SPE) was performed to extract PFAS from the liquid samples. Briefly, an ISOLUTE ENV+ SPE cartridge (200 mg/6 mL) was preconditioned with 10 mL of methanol followed by 10 mL of 1% acetic acid and 10 mL of DI water at a rate of 1 drop/sec under vacuum. Then, 5.0 mL of a liquid sample, containing 0.5 mL M4PFOA (200 µg/L), was passed through the cartridge. Then, the cartridge was rinsed two consecutive times with 7.5 mL DI water per rinse. Subsequently, the target analytes (PFAS) were eluted with 5 mL methanol at a rate of 1 drop/sec and collected in a polypropylene vial that was precleaned using 1:1 (v/v) methanol/acetone. The elution procedure was repeated with a second 5 mL aliquot of methanol. The eluents were then combined and concentrated to 2 mL under a flow of high purity nitrogen. Then, 1 mL of the sample was combined with 0.8 mL DI water and 0.2 mL internal standard (M8PFOA, 200 µg/L) in a LC/MS vial. Upon mixing, the samples were stored at 4 °C until analyzed for the target PFAS.

6.3. Results and discussion

6.3.1. Leachate characterization

Table 6-4 summarizes concentrations of PFAS and other key compositions in the leachate samples with or without the onsite pre-treatment. Despite some seasonal fluctuations, 14 PFAS were consistently detected. Overall, the highest concentrations of PFAS were PFHxA (568-2260 ng/L), PFBA (399-1020 ng/L), PFPeA (242-1570 ng/L), PFOA (209-573 ng/L), and PFBS (158-630 ng/L). Namely, the short-chain PFAS were the predominant PFAS. The level of PFOS was only 34.1 ng/L in the raw leachate and 62.0 ng/L in the pre-treated leachate. The dominance of short-chain PFAS can be attributed to the conversion of the longer-chain homologues and/or PFAS precursors through the complex biogeochemical processes inside the landfill and chemical and photochemical processes when it was exposed to the natural environment (Li et al., 2020a; Wei et al., 2019). Moreover, the on-site pretreatment increased the concentrations of the primary PFAS by a factor ranging from 2.6 for PFBA to 6.5 for PFPeA, and increased to the sum of all the PFAS from 1917.1 to 5636.3 ng/L, indicating that these PFAS were generated during the process. It has been known that degradation of PFAS follows a stepwise chain-shortening process, with shorter-chain (4-6 carbons) PFAS being less degradable and more mobile in the environment (Li et al., 2020a). Seasonally, the PFAS levels from the March and September samples were quite comparable, (Sum of PFAS = 5636.3, 6130.8, 5907.7 ng/L, respectively, for the treated leachate samples obtained from the three dates). This is in line with the company's two-year monitoring data that the PFAS concentrations had been rather stable, indicating the dissolution and transformation processes of PFAS in the landfill were quite steady.

Table 6-4. PFAS and other key compositions in a MSW landfill leachate.

Sample Location		Outfall (After On-site Leachate Pretreatment System)		
Date		3/5/2020	9/10/2020	9/15/2020
PFAS* (ng/L)	PFBA	1020	583	824
	PFBS	630	588	616
	PFPeA	873	1570	1360
	PFPeS	ND	ND	10.8
	PFHxA	1770	1980	2260
	PFHxS	217	241	126
	4:2 FTS	ND	ND	5.47
	PFHpA	297	298	258
	PFHpS	ND	ND	ND
	PFOA	570	573	217
	PFOS	62	55.5	46.5
	6:2 FTS	92.2	104	35.9
	PFOSA	ND	ND	ND
	PFNA	28.4	26	10
	PFNS	ND	ND	ND
	PFDA	25	27.8	30.7
	PFDS	ND	ND	ND
	8:2 FTS	11.6	9.12	8.2
	PFUnA	ND	ND	6.57
	MeFOSAA	22.6	46.9	29.4
	PFDoA	ND	ND	16.7
	EtFOSAA	17.5	28.5	46.5
	PFTrDA	ND	ND	ND
	PFTeDA	ND	ND	ND

Sample Location		Outfall (After On-site Leachate Pretreatment System)		
Date		3/5/2020	Date	3/5/2020
Inorganics (mg/L)	Calcium	130	--	270
	Magnesium	110	--	140
	Iron	7.7	--	14
	Manganese	0.46	--	0.82
	Potassium	350	--	380
	Sodium	2900	--	3100
	Chloride	6100	--	6100
	Fluoride	0.95	--	1.7
	Sulfate	610	--	640
	Ammonia	550	--	14
	Total nitrogen	600	--	--
	Nitrate-nitrite	0.93	--	49
	Total phosphate	--	--	4.5
Others (mg/L)	Total Dissolved Solids (TDS)	10000	--	11000
	Total Suspended Solids (TSS)	6	--	280
	Total Organic Carbon (TOC)	440.1	424.4	418.6

* A list of acronyms for the PFAS are provided in the Supplementary Material.

As expected, the leachate samples contained high concentrations of total dissolved solids (TDS) and DOM. The TDS level amounted to ~10000 mg/L in the raw leachate, which was decreased to 3300 mg/L after the on-site pre-treatment. Chloride was the predominant anion (6100 and 1700 mg/L in the raw and pretreated leachate, respectively), whereas sodium was the primary cation (2900 and 940 mg/L). In addition, high concentrations (hundreds of mg/L) of calcium,

magnesium, ammonium, and sulfate were also present. The concentrations of the anions are orders of magnitude higher than those of PFAS. Consequently, the anions may inhibit the adsorption of anionic PFAS by Fe/TNTs@AC. Conversely, as the TNTs sites carry the negatively charged O^- functional groups, the presence of cations (especially Ca^{2+} and Mg^{2+}) may facilitate the adsorption due to suppressed negative surface potential and cation bridging effects (Xu et al., 2020a). Also noteworthy is the unusually high concentration of DOM (293.8 and 440.1 mg/L as TOC in the raw and pretreated leachate, respectively). The elevated TOC level after the treatment was attributed to unsettled biomass and/or microbial exudates.

The onsite pretreated leachate was used in the subsequent PFAS treatability study.

6.3.2. Bench-Scale treatability study

6.3.2.1. Pre-oxidation of TOC in leachate by H_2O_2 and simulated solar light

DOM is known to cause fouling AC and ion exchange resins, and the high-strength organic matrix (DOM and organic-N) may interfere with the PFAS adsorption and photocatalytic degradation (Li et al., 2020b; Zhao et al., 2018b). To mitigate the inhibition, an attempt was made to oxidize part of the organics by H_2O_2 before the adsorption by Fe/TNTs@AC.

Fig. 6-4 shows that increasing the H_2O_2 dosage from 0.1 to 1.0 M progressively reduced the leachate color after 4 or 8 hours of contact. **Fig. 6-5** shows that the application of simulated solar light improved the leachate decoloring effectiveness by H_2O_2 (0.5 M). Given that leachate color is associated with DOM and metal-organics complexes, these preliminary data suggest that combining solar light and H_2O_2 may break down part of DOM and their complexes. **Fig. 6-6** shows TOC removal kinetics by H_2O_2 in the dark or in the presence of simulated solar light. Consistent with the color removal data, H_2O_2 alone may not effectively mineralize the TOC, with only 16% TOC removed at a dosage of 1.0 M after 8 h. In contrast, 0.5 M combined with simulated solar

light removed ~28% TOC from the leachate. As DOM in landfill leachate can be quite diverse in their size, structure, functionality, aromaticity, and hydrophobicity, the results indicate that only a fraction of the DOM was prone to the oxidation, leaving a large fraction of DOM remain in the leachate.

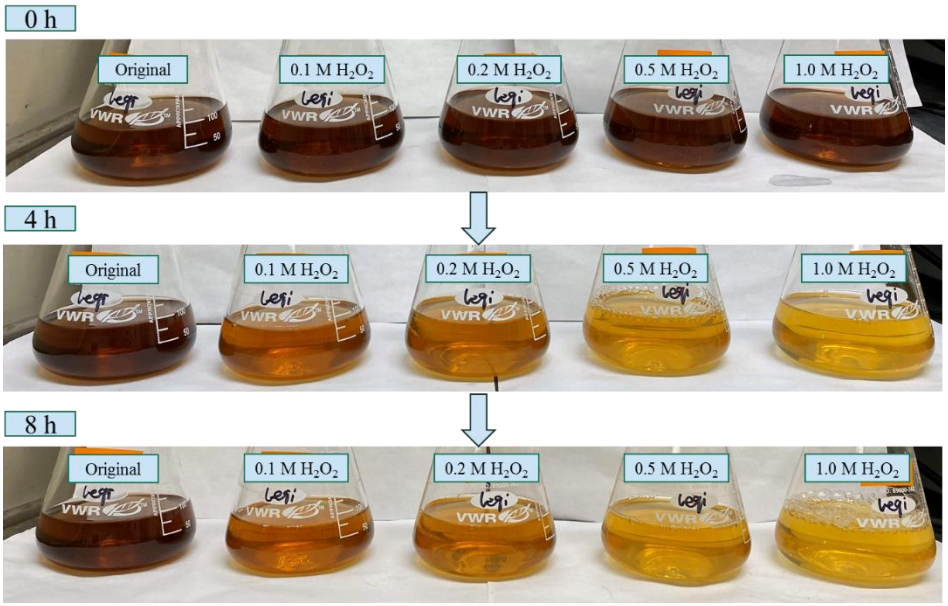

Fig. 6-4. Optical views of leachate color change after 4 and 8 hours of treatment with H_2O_2 at various concentrations (0.1 to 1 M) under ambient indoor light.

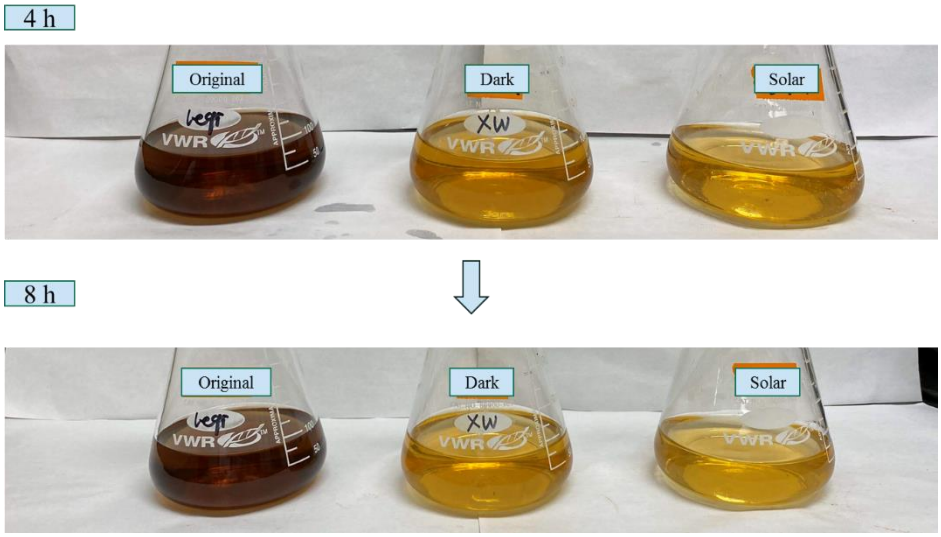

Fig. 6-5. Optical views of leachate color change after 4 and 8 hours of treatment with 0.5 M H_2O_2 in darkness or under simulated solar light.

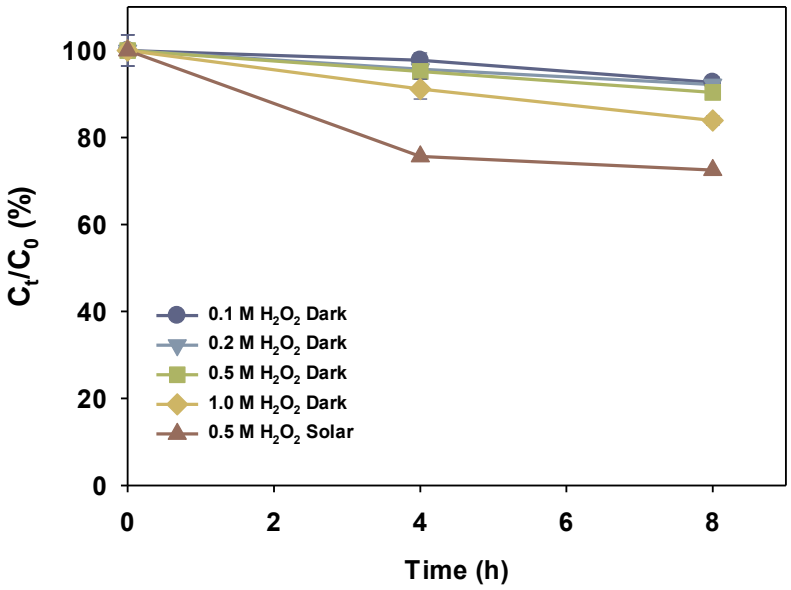

Fig. 6-6. TOC removal kinetics by H_2O_2 in the dark or in the presence of simulated solar light. Experiment conditions: initial TOC = 424.4 mg/L, pH = 8.5, and solar light intensity = 100 mW/cm^2.

6.3.2.2. Effects of TOC pre-oxidation on subsequent adsorption and photodegradation of PFOA by Fe/TNTs@AC

Fig. 6-7a shows the adsorption kinetics of spiked-PFOA in leachate with Fe/TNTs@AC with or without the H_2O_2 pretreatment. In both cases, PFOA was rapidly adsorbed, with >80% of PFOA removed in ~1 hour. The adsorption equilibrium was reached after ~8 h, where 98% of PFOA was removed. The H_2O_2 pre-oxidation modestly improved the initial adsorption rate, which resulted in

a PFOA removal of 88% after 1 h. After 24 hours of adsorption, the PFOA removal was about the same for both cases. **Fig. 6-7b** shows that the H_2O_2 pretreatment resulted in a lower final TOC level (272.9 vs. 211.5 mg/L) or accumulated less TOC on the solids (by a factor of 0.63), although it had no appreciable effect on the adsorption kinetics.

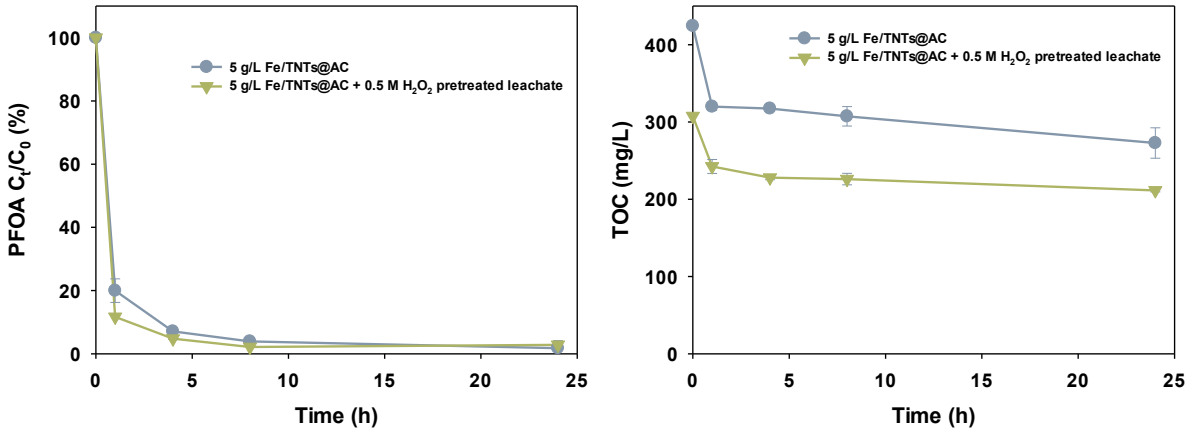

(a) **(b)**

Fig. 6-7. Effects of H_2O_2 pre-oxidation on adsorption kinetics of spiked PFOA (a) and DOM (measured as TOC) (b) in landfill leachate by Fe/TNTs@AC. Pre-oxidation conditions: initial TOC = 424.4 mg/L, [H_2O_2] = 0.5 M, contact time = 8 hours, and solar light intensity = 100 mW/cm^2. Adsorption conditions: initial PFOA spiked in leachate = 100 µg/L, TOC after the H_2O_2 with solar light = 307.7 mg/L, Fe/TNTs@AC = 5 g/L, and pH = 8.5. Data are plotted as mean of duplicates, and errors refer to relative deviation from the mean.

Given the diversity of DOM in landfill leachate and their different characteristics, these observations can be attributed to 1) the H_2O_2 pretreatment may not remove the fraction of DOM

that inhibits the adsorption of PFOA, and 2) the adsorption capacity of Fe/TNTs@AC for PFOA was not fully used under the experimental conditions.

While more intensive reaction conditions (e.g., higher chemical dosage, stronger oxidant, and elevated temperature) can break down more DOM, it may not be practically feasible due to the associated cost.

Based on the equilibrium adsorption data of PFOA and TOC, the relative binary separation factor $\alpha_{PFOA/TOC}$ is calculated according to:

$$\alpha_{PFOA/TOC} = \frac{q_{PFOA}C_{TOC}}{q_{TOC}C_{PFOA}} \quad \textbf{(6-1)}$$

where q is the equilibrium uptake of PFOA or TOC, and C is the corresponding aqueous phase concentration. The calculated $\alpha_{PFOA/TOC}$ is 110, which is much higher than 1, indicating the material is highly selective towards the target PFOA over the competing DOM.

Following the adsorption, the PFOA-laden Fe/TNTs@AC was separated from the leachate and then subjected to the UV irradiation. **Fig. 6-8** shows that Fe/TNTs@AC with the UV irradiation alone was not able to effectively degrade PFOA. In contrast, Li et al. (2020b) reported that Fe/TNTs@AC with UV was able to degrade >90% of PFOA that was pre-loaded on the Fe/TNTs@AC from an aqueous solution. These observations clearly indicate the strong inhibitive effect of the leachate matrix.

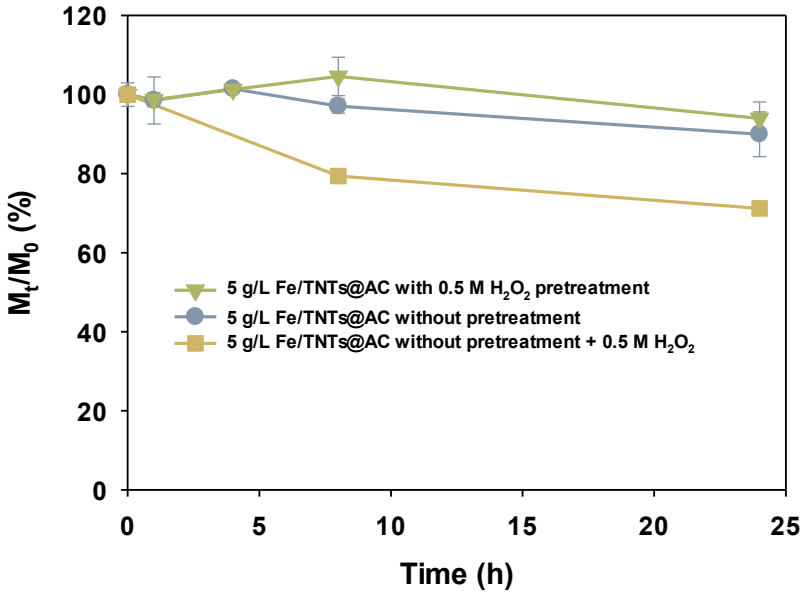

Fig. 6-8. Effect of H_2O_2 pre-oxidation on photodegradation kinetics of pre-sorbed PFOA by Fe/TNTs@AC. Pre-oxidation conditions (when applied): $[H_2O_2]$ = 0.5 M, contact time = 8 hours, and solar light intensity = 100 mW/cm^2. Adsorption conditions: Initial PFOA spiked in leachate = 100 µg/L, Fe/TNTs@AC = 5 g/L, and pH = 8.5. Photodegradation conditions: $[H_2O_2]$ = 0.5 M (when applied), and UV (λ = 254 nm) intensity = 21 mW/cm^2. M_0 and M_t: Mass of PFOA in the system at time 0 and t, respectively.

Based on the adsorption and photodegradation results, the H_2O_2 pretreatment of the leachate displayed little positive effects on the adsorption and photodegradation of PFOA. Moreover, from a practical standpoint, pretreating a large volume of the leachate may demand a large amount of H_2O_2, rendering it cost-prohibitive. Therefore, the H_2O_2 pretreatment of the leachate was excluded in the subsequent experiments.

Instead of applying H_2O_2 to pre-treat the leachate, it should be much more cost-effective practical to apply H_2O_2 or other engineered means to the PFOA-laden solids in the photodegradation stage because the volume of the solids is much smaller than that of the leachate. For instance, at a material dosage of 5 g/L, the liquid volume is 85 times of the bulk volume of the solids. This is a major advantage of the "concentrate-&-destroy" strategy, which concentrates PFAS from a large volume of leachate on a small volume of the material through selective adsorption, and then degrade them in a small photo-reactor and through additional enhancement means. **Fig. 6-8** shows that in the presence of 0.5 M H_2O_2 during the photodegradation, ~30% of pre-adsorbed PFOA on Fe/TNTs@AC was photodegraded after 24 h. In other words, applying H_2O_2 during the photodegradation stage is not only more economical, but more effective. H_2O_2 can react with iron on the Fe/TNTs@AC surface to stimulate heterogeneous Fenton reactions, which may enhance the breakdown of DOM and facilitate the photocatalytic degradation of PFOA (Li et al., 2020b). It is noted that the slurry pH during the photodegradation was kept at the same pH (8.5) as that of the original leachate, which is unfavorable for Fenton reactions and the photodegradation (see **Section 6.3.2.3** below).

6.3.2.3. Effects of pH and H_2O_2 dosage on photodegradation of PFOA on Fe/TNTs@AC

To beef up the PFOA degradation, the solid-phase photodegradation of PFOA was carried out at three pH levels (5.0, 7.0 and 8.5) (pH for the adsorption step was kept at the original leachate pH of 8.5 in all cases). **Fig. 6-9a** shows that when the pH during the photodegradation was lowered to 7.0, the PFOA photodegradation was boosted to 77%. However, further degreasing the pH to 5.0 resulted in insignificant further improvement.

The addition of H_2O_2 and the resulting Fenton reactions can degrade adsorbed DOM, and thus suppress the inhibitive effect on the photocatalytic degradation of PFOA. It has been well

recognized that Fenton reactions are more favored under acidic conditions. In addition, pH can affect the adsorption mode and photocatalytic selectivity of Fe/TNTs@AC towards PFOA. Fe/TNTs@AC is composed of mixed AC and α-Fe_2O_3/TNTs phases (Li et al., 2020b). The α-Fe_2O_3/TNTs phases bind with PFOA through electrostatic interactions and complexation with the head carboxylate group, while the AC phase adsorbs PFOA through hydrophobic interaction with the tail and anion-π interactions (Xu et al., 2020b). The concurrent interactions not only enhance the adsorption selectivity for PFOA, but also result in a side-on adsorption mode, where PFOA is attached in parallel to the material surface. This adsorption mode is conducive to the hole-mediated decarboxylation of the head group and the subsequent stepwise chain-shortening defluorination reactions (Li et al., 2020b). However, at elevated pH, the binding of the head groups is weakened due to increased negative surface potential and competition of OH^- ions. As a result, the adsorption of PFOA is dominated by a tail-tethered orientation of PFOA on the AC surface, which is unfavorable for the head-group decarboxylation that is a prerequisite in the PFOA photodegradation. In addition, excessive HO^- could react with the photogenerated holes to produce excessive hydroxyl radicals, retarding the direct hole oxidation of PFOA (Li et al., 2020b).

To further explore the effect of H_2O_2, the photodegradation was carried out in the presence of various concentrations of H_2O_2. **Fig. 6-9b** shows that in the presence of 0.1, 0.5, 1.0, or 1.5 M of H_2O_2, the 24-h photodegradation of the Fe/TNTs@AC laden PFOA was 28%, 77%, 85%, and 74%, respectively. The lower H_2O_2 dosage was insufficient to suppress the DOM inhibition, while excessive H_2O_2 or H_2O_2/Fe^{2+} ratio can decrease the generation of hydroxyl radicals (Gulkaya et al., 2006). Taking into account both chemical cost and photodegradation efficiency, 0.5 M H_2O_2 was used in the subsequent tests.

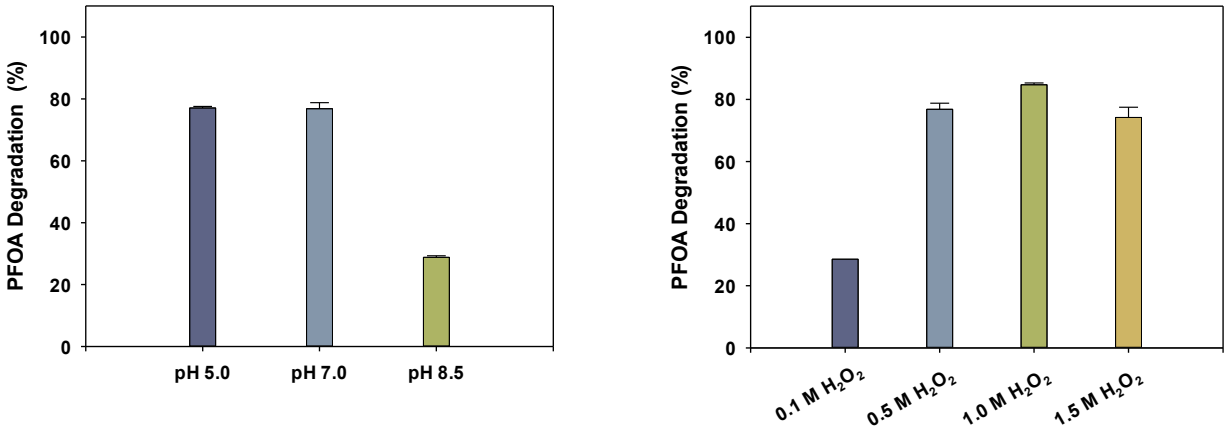

Fig. 6-9. Effects of pH (a) and H_2O_2 dosage (b) on the photodegradation of PFOA using Fe/TNTs@AC. PFOA was pre-sorbed on Fe/TNTs@AC under conditions: initial PFOA in leachate = 100 μg/L, Fe/TNTs@AC = 5 g/L, pH = 8.5, and contact time = 2 hours. Photodegradation conditions: [H_2O_2] = 0.5 M, UV (λ = 254 nm) intensity = 21 mW/cm^2, and irradiation time = 24 hours. Data are plotted as mean of duplicates, and errors refer to relative deviation from the mean.

6.3.2.4. Effects of temperature and solid-to-liquid ratio on photocatalytic degradation of PFOA on Fe/TNTs@AC

Fig. 6-10a shows that increasing the photodegradation temperature from 38 °C to 65 °C had negligible effect on the 24-h degradation of PFOA on Fe/TNTs@AC in the presence of 0.5 M H_2O_2, with ~77% PFOA degraded in both cases. Increasing temperature has been reported to enhance Fenton reactions in homogeneous systems as it may enhance the iron-catalyzed H_2O_2 decomposition into •OH^- radicals, though higher temperature may lead to thermal breakdown of H_2O_2 into O_2 and H_2O (Zazo et al., 2011). The negligible temperature effect in the Fe/TNTs@AC-

H_2O_2 system can be attributed to: 1) the relatively small temperature increase may not induce a notable boosting effect on the heterogeneous Fenton process, 2) the Fenton reactions cannot directly degrade PFOA, and 3) the solid-phase photocatalytic degradation of PFOA was not affected by the moderate temperature rise.

For comparison, we tested another commonly used oxidant, persulfate, in lieu of H_2O_2. **Fig. 6-10b** shows that in the presence of 0.2 M of persulfate, the Fe/TNTs@AC-UV system was able to degrade 65% and 87% of the pre-adsorbed PFOA at 38 °C and 65 °C, respectively. Compared to H_2O_2, the presence of persulfate in the Fe/TNTs@AC-UV system resulted in a 12% less PFOA degradation at 38 °C, but 10% higher at 65 °C. The results are in accord with the literature that persulfate may be activated by UV and/or elevated temperature and degrade PFAS (Li et al., 2020a; Wei et al., 2019). In our case, Fe/TNTs@AC, UV, persulfate, and temperature may work synergistically to lower the activation energy and facilitate radical generation towards both DOM and PFAS on the solid surface. Therefore, further studies are warranted using persulfate as a low-cost stimulating reagent in the photocatalysis system, especially when low-cost thermal energy is available.

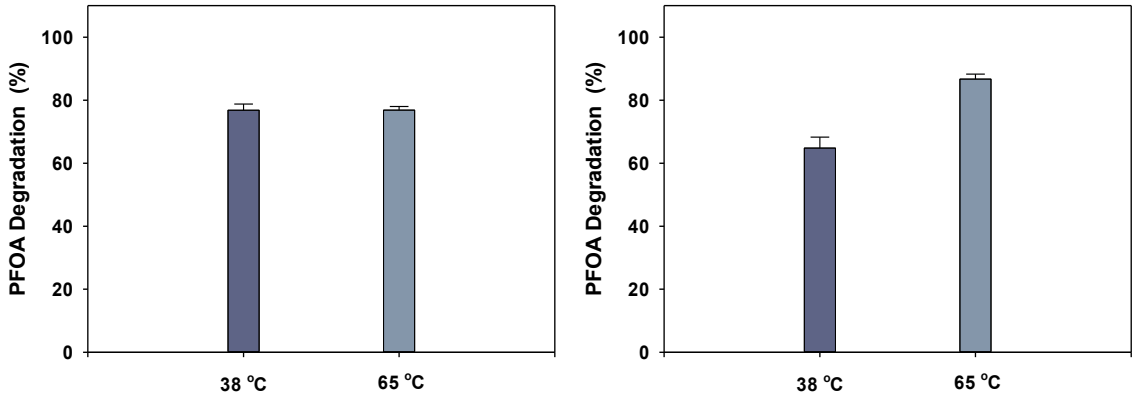

Fig. 6-10. Effect of temperature on photodegradation of PFOA pre-sorbed on Fe/TNTs@AC in the presence of hydrogen peroxide (a) and sodium persulfate (b). Adsorption conditions: initial PFOA spiked in leachate = 100 μg/L, Fe/TNTs@AC = 5 g/L, pH = 8.5, contact time = 2 hours. Photodegradation conditions: pH = 7.0, $[H_2O_2]$ = 0.5 M or $[Na_2S_2O_8]$ = 0.2 M, UV (λ = 254 nm) intensity = 21 mW/cm^2, and irradiation time = 24 hours.

The solution volume, or solid/liquid ratio, in the photo-reactor may affect the mixing and light exposure. **Fig. 6-11** shows that the 24-hr photodegradation efficiencies of PFOA in the Fe/TNTs@AC-UV-H_2O_2 system remained the same when the solid:liquid ratio was varied at 0.2:5, 0.2:10, and 0.2:15 g:mL. Consequently, the subsequent experiments were carried out at a solid/liquid ratio of 1/50.

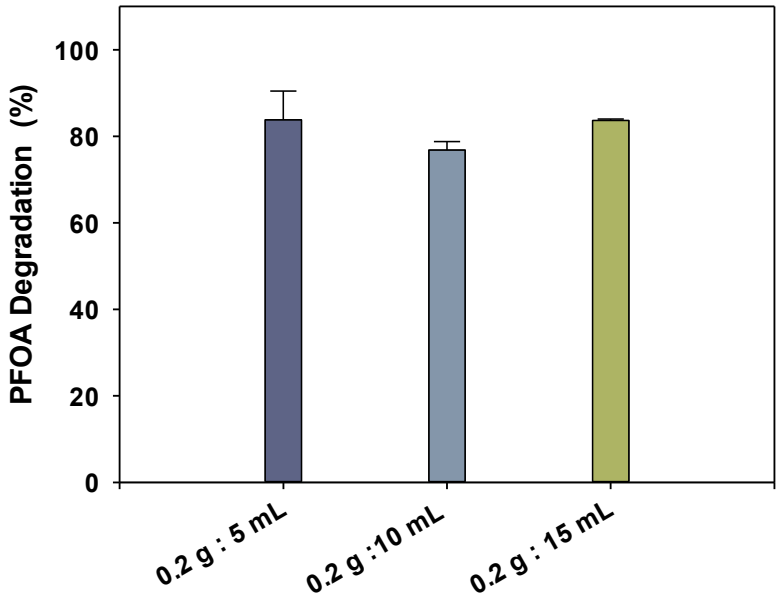

Fig. 6-11. Effect of solid-to-liquid ratio on photodegradation of PFOA pre-adsorbed on Fe/TNTs@AC. Adsorption conditions: initial PFOA spiked in leachate = 100 μg/L, Fe/TNTs@AC

= 5 g/L, pH = 8.5, contact time = 2 hours. Photodegradation conditions: pH = 7.0, [H_2O_2] = 0.5 M, UV (λ = 254 nm) intensity = 21 mW/cm^2, irradiation time = 24 hours.

6.3.2.5. Photocatalytic degradation kinetics of PFOA on Fe/TNTs@AC

Fig. 6-12 shows the H_2O_2-assisted photodegradation kinetics of PFOA, which was pre-concentrated on Fe/TNTs@AC from the PFOA-spiked leachate. Despite the strong matrix effect, the Fe/TNTs@AC-UV-H_2O_2 system showed a relatively fast heterogeneous photocatalytic degradation rate under the ambient environmental conditions. After 24 h of the UV irradiation, ~77% of the solid-bound PFOA was degraded and it appeared that the degradation would continue thereafter.

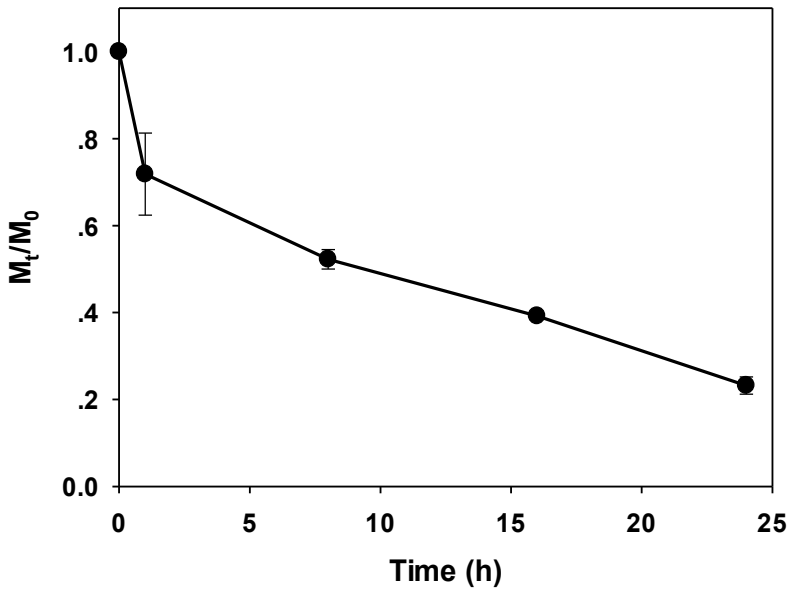

Fig. 6-12. Photodegradation kinetics of pre-sorbed PFOA by Fe/TNTs@AC. Adsorption conditions: Initial PFOA in leachate = 100 μg/L, Fe/TNTs@AC = 5 g/L, pH = 8.5, and contact time = 2 hours. Photodegradation conditions: pH = 7.0, [H_2O_2] = 0.5 M, and UV (λ = 254 nm)

intensity = 21 mW/cm^2. Data are plotted as mean of duplicates, and errors refer to relative deviation from the mean. M_0 and M_t refer to total mass of PFOA in the system at time 0 and t, respectively.

Little information is available in the open literature on the photocatalytic degradation rates of PFAS in landfill leachate to warrant a sound comparison of the results. Yet, we may postulate that the degradation rates can be further accelerated by improving both adsorption selectivity for PFAS and the photocatalytic activity of the composite material. Given that Fe/TNTs@AC was not optimized for treating landfill leachate, the adsorption and subsequent photodegradation efficiency can be further ameliorated by tailoring the material and optimizing the photocatalytic conditions. For instance, the adsorption selectivity for PFAS may be further enhanced by use of microporous AC that may exclude DOM through size exclusion, and the lower DOM uptake not only enhances the PFAS adsorption, but also enhances the subsequent photodegradation rates of PFAS.

6.3.2.6. Removal kinetics of multiple PFAS in landfill leachate by Fe/TNTs@AC

Based on the treatment protocol obtained from PFOA-spiked landfill leachate, the treatment effectiveness of Fe/TNTs@AC for removal of all the detectable PFAS at the field environmental concentrations was tested. **Fig. 6-13** shows the removal rates of 14 detected PFAS from the on-site pre-treated leachate. At a dosage 5 g/L, Fe/TNTs@AC was able to remove an average of 82% (26%-100%) of 13 PFAS after 8 hours (**Fig. 6-13a**), with the exception of PFPeA, which showed a negative removal. The poor removal rates of the short-chain PFAS, such as PFPeA, PFBA, and PFHxA, can be attributed to 1) the weaker adsorption affinity compared to the longer-chain PFAS associated with the weaker hydrophobic interactions of the former (Maimaiti et al., 2018), 2) transformation of precursors (e.g., longer-chain homologs and other fluorochemicals) into the short-chain products (Gonzalez et al., 2020), 3) breakdown from longer-chain PFAS homologues

(Singh et al., 2019), and/or 4) displacement from the adsorption sites by other PFAS of higher affinity (Maimaiti et al., 2018), For instance, generation of PFPeA and PFBA from various point or non-point precursors has been widely reported in the environment (Zhang et al., 2019). Apparently, in our case, such transformations may occur during the storage of the leachate storage and processing, and more likely, during the adsorption because of the high photocatalytic reactivity of the material.

Fig. 6-13b shows that when the material dosage was increased to 10 g/L, Fe/TNTs@AC was able to remove 14 PFAS by an average of 88% (12%-100%), 88% (7%-100%), and 89% (15%-100%) after 1, 4, and 8 hours, respectively. It is noteworthy that the removal of PFOS was relatively lower than other long-chain PFAS, which can be attributed to the precursor transformation in addition to the DOM inhibition. Previously, we observed that Fe/TNTs@AC at a dosage of 2 g/L was able to remove >99% of PFOS from an aqueous solution (Zhao, 2019). While other materials need more dosage to adsorb similar percentage of PFAS from leachate. For example, 53 g/L coal-based magnetic activated carbon (MAC) was able to remove 72.8-89.6% of PFHxA, PFHpA, PFOA, PFNA and PFDoA in leachate samples in 120 min. The initial concentrations of them are 1435 ng/L, 423 ng/L, 2683 ng/L, 221 ng/L, and 53 ng/L, respectively (Zhang et al., 2018).

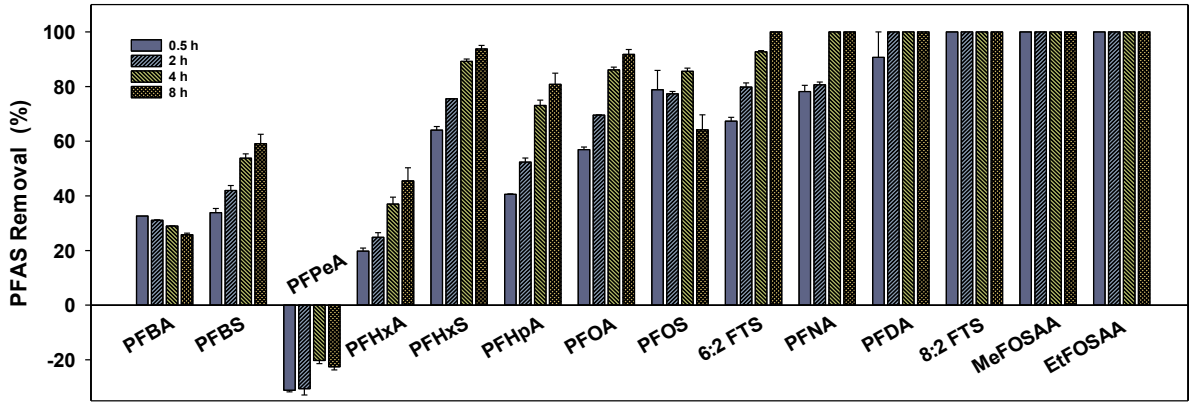

(a)

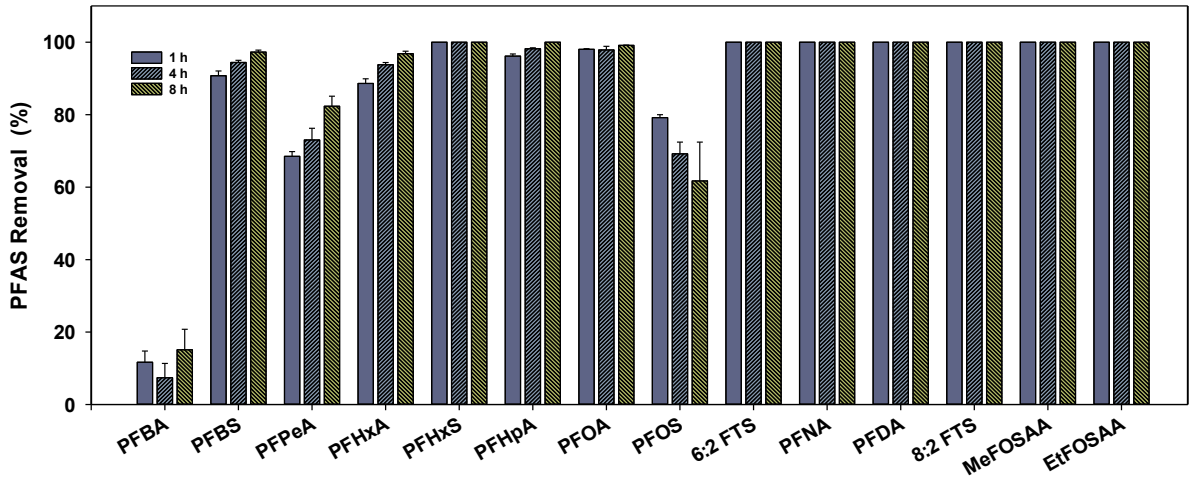

(b)

Fig. 6-13. Adsorption rates of 14 PFAS in a landfill leachate by Fe/TNTs@AC at a dosage of 5 g/L (a) and 10 g/L (b). Experimental conditions: pH = 8.5, leachate compositions are given in **Table 6-4**. Data are plotted as mean of duplicates and errors indicate relative deviation from the mean.

Despite the strong effect of the leachate matrix, the adsorption pre-concentrates PFAS from a large volume of leachate onto a small volume of Fe/TNTs@AC, leaving the majority of the

competing solutes, i.e., high concentrations of DOM and anions, in the solution phase. As such, the strong matrix effect was mitigated in the subsequent solid-phase photocatalytic degradation.

The reusability of Fe/TNTs@AC was tested by subjecting the same material to three consecutive runs of the adsorption-photodegradation tests. Following the 8-h adsorption, the PFAS-laden Fe/TNTs@AC was separated from leachate and then subjected to the UV light for 24 h, which not only degrades the PFAS, but also regenerates the material. **Fig. 6-14** shows that after the three adsorption-photodegradation runs, Fe/TNTs@AC remained effective for removing 10 of the 14 PFAS. At a dosage of 10 g/L, Fe/TNTs@AC removed an average of 95.2% (61.7%-100%) of 13 PFAS (except for PFBA) from the leachate in Round 1, 85.8% (18.8%-100%) in Round 2, and 73.6% (7.3%-100%) in Round 3. Again, the most drop in the removal occurred to PFBA and PFPeA in Rounds 2 and 3, where PFBA showed a negative removal. In addition to the conversion of the precursors and longer-chain homologues, the accumulation of these PFAS and their precursors from the previous adsorption cycle may also contributed to the decreased removal rates.

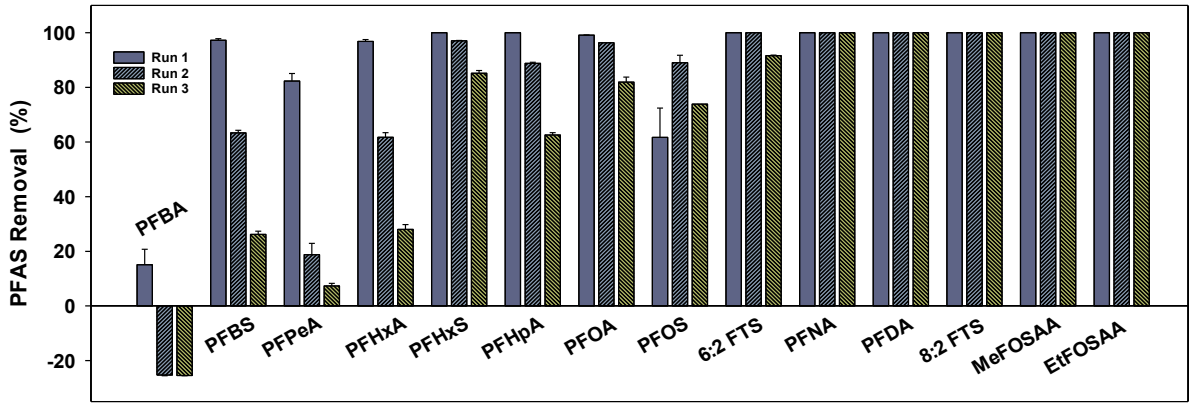

Fig. 6-14. Removal of multiple PFAS from landfill leachate by Fe/TNTs@AC in three consecutive runs of adsorption-photodegradation. Adsorption conditions: Fe/TNTs@AC = 10 g/L, pH = 8.5, and contact time = 8 hours. Photodegradation conditions: pH = 7.0, [H_2O_2] = 0.5 M, UV (λ= 254

nm) intensity = 21 mW/cm^2, and irradiation time = 24 hours. Data are plotted as mean of duplicates and errors indicate relative deviation from the mean.

Overall, the gradual decrease of the removal rates for shorter-chain PFAS in multiple runs can be attributed to 1) continued accumulation and conversion of their precursors in the solid phase, 2) accumulation of DOM and other competing constituents from the leachate on Fe/TNTs@AC, and 3) incomplete photocatalytic degradation of the PFAS, precursors, and DOM. These drawbacks may be beefed up in various ways. First, the material can be further tailored to increase both the adsorption selectivity for the target PFAS and the photocatalytic activity. Second, taking advantage of the "Concentrate-&-Destroy" concept, additional engineered means may be applied to the solid-phase photocatalytic degradation/regeneration stage by optimizing the reaction chemistry (pH and oxidants), temperature, and UV intensity.

6.3.3. Preliminary pilot-scale demonstration

Building upon the bench-scale experiments, preliminary pilot-scale tests were conducted in two-consecutive adsorption-photodegradation runs at the landfill site under the field leachate conditions. Pilot-scale tests are essential to confirm the bench-scale results and to guide further technology development. Unfortunately, due to an unexpected upset of the onsite treatment facilities, the content of total suspended solids in the leachate was unusually high (280 mg/L), representing an additional challenge to the treatment in addition to DOM. A total of 18 PFAS were detected in the leachate at the field. **Fig. 6-15a** shows that despite the added interferences, Fe/TNTs@AC demonstrated excellent adsorption for the PFAS in the first round, where more than 92% (9.0%-100%) of the 18 PFAS was removed from the field leachate after 8 h of the adsorption under the field leachate conditions. Following the photocatalytic regeneration, the same material

was able to remove >71% (3.3%-100%) of ∑PFAS in Round 2. Consistent with the bench-scale findings, the material was less effective for PFBA and PFPeA, but highly effective for the long-chain PFAS. The drop in the PFAS adsorption in Round 2 was higher than in the bench-scale experiments. This was largely due to the elevated TSS concentration, which not only fouled some of the adsorption sites, but also blocked the light accessibility and inhibited the photo-regeneration efficacy. After 72 hours of photodegradation following the first-round adsorption, Fe/TNTs@AC degraded an average of 84% (50%-100%) of 16 PFAS from the leachate based on the solid-phase extraction data (**Fig. 6-15b**). The concentrations of PFBA and PFBS in the solid phase remained high upon the photodegradation, which again indicated significant conversion of precursors/homologues under the photocatalytic conditions.

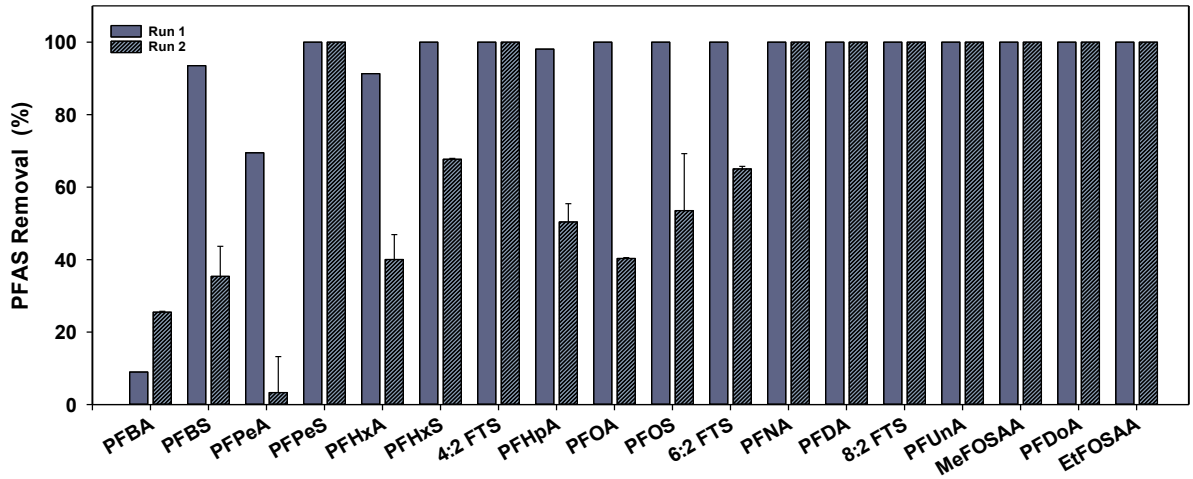

(a)

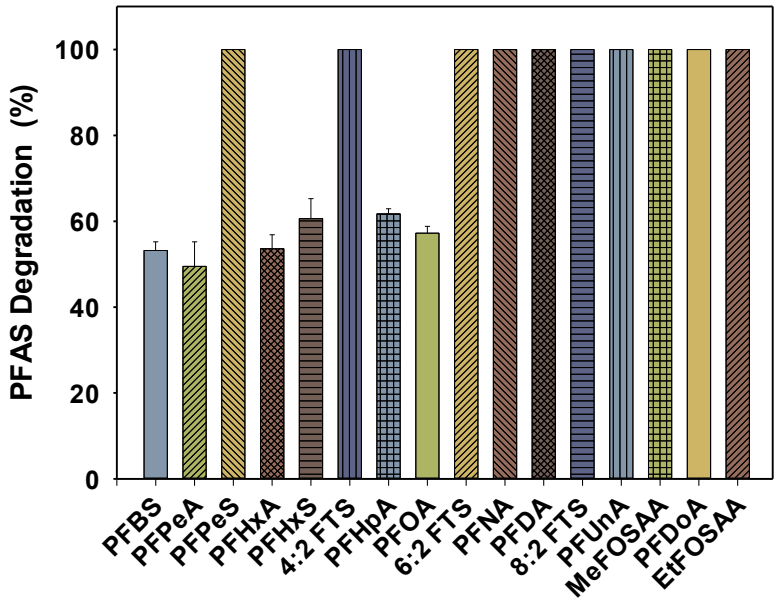

(b)

Fig. 6-15. Pilot-scale removal and degradation of multiple PFAS from landfill leachate in two consecutive cycles of adsorption-photodegradation at the field: (a) Adsorption and (b) photodegradation of PFAS pre-sorbed on Fe/TNTs@AC. Adsorption conditions: Fe/TNTs@AC = 10 g/L, pH = 6.5, and contact time = 8 hours. Photodegradation conditions: pH = 7.0, $[H_2O_2]$ = 0.5 M, UV (λ = 254 nm) intensity = 6.9 mW/cm^2, and irradiation time = 72 hours. Data are plotted as mean of duplicates and errors indicate relative deviation from the mean.

6.4. Summary and concluding remarks

For the first time, we tested a novel "Concentrate-&-Destroy" technology using a photo-regenerable adsorptive photocatalyst for enhanced removal of PFAS from a model landfill leachate. The key findings are summarized as follows:

1) Up to 18 different PFAS were detected in the landfill leachate, with the most predominant PFAS being PFHxA. In addition, the leachate contained high concentrations of DOM, chloride, sulfate, ammonia, and metals.

2) Bench-scale experiments using the leachate spiked with 100 μg/L PFOA indicated that Fe/TNTs@AC at a dosage of 5 or 10 g/L was able to remove >98% of the PFOA from leachate within 8 hours. The higher dosage was more conducive for the subsequent photo-regeneration of the material, facilitating repeated uses of the material. Fe/TNTs@AC showed much higher selectivity towards PFOA over DOM in the leachate.

3) The presence of low concentrations of H_2O_2 or $S_2O_8^{2-}$ during the photocatalytic degradation stage greatly enhanced the solid-phase destruction of the PFAS, and thus facilitated the efficient regeneration of the material. Conversely, pre-treating the bulk leachate using H_2O_2 before the adsorption was not only less economical, but showed minimal effect on the subsequent adsorption and photodegradation.

4) Despite the strong matrix effect, the Fe/TNTs@AC-UV-H_2O_2 system showed a relatively fast heterogeneous photocatalytic degradation rate under the leachate conditions. After 24 h of the UV irradiation, ~77% of the solid-bound PFOA was degraded.

5) Fe/TNTs@AC can effectively adsorb PFAS over a broad pH range (5.0-8.5) and photodegrade sorbed PFAS at neutral or acidic pH. Increasing the photodegradation temperature from 38 °C to 65 °C had negligible effect on the photo-degradation of PFOA in the Fe/TNTs@AC-H_2O_2-UV system, but increased the PFOA degradation from 65% to 87% in the Fe/TNTs@AC-Persulfate-UV system. The solid:liquid ratio during the photodegradation appeared to play a minor role.

6) The effective photodegradation of PFAS in the Fe/TNTs@AC-UV-H_2O_2 system also effectively regenerates the material, allowing for repeated uses. Fresh Fe/TNTs@AC at a dosage of 10 g/L removed >95% of 13 PFAS from the leachate, 86% after first regeneration, and 74% when reused three times. Fe/TNTs@AC was less effective for PFBA and PFPeA primarily due to transformation of precursors and/or homologues into these short-chain PFAS and the shorter-chain PFAS can be replaced by longer-chain PFAS.

7) Pilot-scale tests preliminarily confirmed the bench-scale results. Despite the strong interference from additional TSS, Fe/TNTs@AC exhibited good adsorption selectivity and removed >92% of 18 PFAS in 8 h under the field leachate conditions. The photocatalytic regeneration degraded an average of 84% of 16 PFAS in the solid phase. Following the photo-regeneration, the same material was able to remove >71% of ∑PFAS.

The "Concentrate-&-Destroy" strategy offers some unique advantages for treating trace concentrations of PFAS in high-strength landfill leachate, where the matrix concentrations are orders of magnitude higher. Upon further material polishing and process optimization, the technology appears promising for more cost-effective removal and degradation of PFAS in landfill leachate or PFAS-laden high-strength wastewaters.

Chapter 7. Overall Conclusions and Suggestions for Future Research

7.1. Overall Conclusions

The dissertation encompasses two parts. One is the sequestration of cadmium in contaminated water and soil using novel nanoparticles. The other is adsorption and photodegradation of per- and polyfluoroalkyl substances (PFAS) from water and landfill leachate.

For the first part, the research goal is improving the adsorption selectivity of Cd by adsorbents, overcoming the competing organic and inorganic ions, increasing the pH resistance, and then further lower the cost by modifying adsorbents. Sodium carboxymethyl cellulose (CMC) stabilized iron phosphate ($Fe_3(PO_4)_2$) nanoparticles were first proposed by modifying an aqueous precipitation approach and in the presence of CMC as a stabilizer. Fully stabilized $Fe_3(PO_4)_2$ (426 mg/L) nanoparticles were obtained using 0.1 wt.% CMC and can remove 87.6% of Cd (C_0 = 1 mg/L) within 11 h at pH 7.0, which was 11.6% higher than non-stabilized nanoparticles. The maximum Langmuir sorption capacity of Cd by CMC-$Fe_3(PO_4)_2$ was 36.1 mg/g at pH 7.0. pH could impact the Cd sorption obviously, while the effects of HA, $NaNO_3$, NaCl, and $NaHCO_3$ were slightly. Increasing pH from 4.0 to 8.0 enhanced the Cd removal rate from 55.1% to 96.3%. The predominant mechanism for Cd immobilization was surface complexation between Cd and $Fe_3(PO_4)_2$. CMC-stabilized $Fe_3(PO_4)_2$ nanoparticles offered considerable sorption capacity and reaction rate. The nanoparticles hold the potential to serve as an effective and environmentally friendly sorbent for *in situ* immobilization of Cd in contaminated water and soil

In order to further enhanced the Cd selectivity and immobilization by sorbents, ferrous sulfide (FeS) nanoparticles were prepared using CMC as a stabilizer. Fully stabilized FeS (100 mg/L) nanoparticles were obtained using 0.01 wt.% CMC and can rapidly remove 93% of 1 mg/L Cd

within 4 h at pH 7.0. The maximum Langmuir sorption capacity of Cd by CMC-FeS was 497.5 mg/g at pH 7.0, which was remarkably large compared to other researchers' work. The dominant immobilization mechanisms were chemical precipitation and surface complexation between Cd and FeS. pH was an important factor, which can enhance Cd removal rate from 73.0% to 98.8% as pH increased from 4.0 to 8.0, whereas the presence of molecular oxygen and HA had a negligible effect. Moreover, co-existing ions can impact the sorption behavior. CMC-stabilized FeS nanoparticles also showed the ability to facilitate long-term immobilization of cadmium in contaminated water.

CMC-FeS had a better performance than CMC-$Fe_3(PO_4)_2$. CMC-FeS nanoparticles were selected for Cd immobilization. Carboxymethyl starch (CMS) and starch were also studied to find another efficient, low-cost and environment friendly stabilizer. Fully stabilized FeS (100 mg/L) nanoparticles were prepared using 0.010 wt.% CMC, 0.025 wt.% CMS, or 0.065 wt.% starch. All stabilized FeS can rapidly remove >89% of Cd within 12 h (initial Cd = 1 mg/L and FeS dosage = 100 mg/L and pH = 7.0). pH still played an important role. When pH increased from 4.0 to 8.0, the removal of Cd increased 25.8%, 34.4%, and 18.3% for CMC-FeS, CMS-FeS, and starch-FeS, respectively. CMC-FeS and CMS-FeS can also be used for *in situ* Cd immobilization in soil. When the 58.3 mg/kg Cd-laden soil was treated by 100 mg/L of CMC-FeS and CMS-FeS, the equilibrium Cd leachability based on toxicity characteristic leaching procedure (TCLP) reduced by 88.4% and 68.0%, and the water-leachable Cd was reduced by 98.2% and 98.0%, respectively. The results further demonstrated that stabilized FeS was a promising material for Cd immobilization in contaminated water and soil.

For the second part, the research goal is to find or synthase sorbents or photocatalysts to efficiently treat PFAS in water and leachate. The behaviors of sorption and regeneration of

perfluorobutanoic acid (PFBA) by resins were first studied. Three commercial resins (IRA900, IRA958, and DOW 66) and one polymeric ligand exchanger (DOW 3N-Cu) can remove 93.8%, 70.7%, 94.3%, and 94.6% of PFBA after 120 h adsorption (initial PFBA = 100 mg/L, resin dosage = 1 g/L, and pH = 7.0). The sorption mechanism of PFBA by resins involved both ion exchange and adsolubilization via hydrophobic interactions between PFBA and the hydrophobic resin matrix. ~90% of the four resin sorption capacities can be recovered by the mixture of 1% NaCl and 40% CH_3OH solution. Of the resins studied, IRA900 showed the best PFBA removal rate and capacity and was able to perform well over a broad pH range. It can be applied to PFBA high concentrated industrial wastewater treatment.

Because there has been no cost-effective technology available for treating PFAS in leachate, a two-step "Concentrate-&-Destroy" technology for treating PFAS from a model landfill leachate through bench- and pilot-scale experiments was tested. The adsorptive photocatalyst (Fe/TNTs@AC) was able to selectively adsorb PFAS despite the strong matrix effect of the leachate. Moreover, the pre-concentrated PFAS on Fe/TNTs@AC were effectively degraded under UV, which also regenerates the material. The presence of 0.5 M H_2O_2 during the photocatalytic degradation enhanced the solid-phase destruction of the PFAS. Fe/TNTs@AC at a dosage of 10 g/L removed >95% of 13 PFAS from the leachate, 86% after first regeneration, and 74% when reused three times. Fe/TNTs@AC was less effective for short-chain PFAS removal. Both bench- and pilot-scale tests proved that the "Concentrate-&-Destroy" strategy were promising for more cost-effective removal and degradation of PFAS in landfill leachate or PFAS-laden high-strength wastewaters.

7.2. Future work

The follow-on studies are recommended in the future:

1) Further study the deliverability and transport behavior of CMC-stabilized FeS nanoparticles in sediment and soil towards *in situ* remediation of metals-contaminated soil. Beside the sandy clay loam soil, other types of soil should also be studied to better understand the performances of CMC-FeS on Cd immobilization towards future field application of the technology.
2) Investigate the long-term stability of the nanoparticle immobilized heavy metals under field conditions.
3) Develop a mechanism-based modeling approach to predict the long-term leaching characteristics of the immobilized metals under various water chemistry and geochemical conditions.
4) More selective sorbents for short-chain PFAS are needed, which may be developed by modifying IRA900 to offer greater sorption capacity and regenerability.
5) More oil dispersants may be tested to regenerate PFAS-laden ion exchange resins or activated carbons.
6) The carbon-based adsorptive photocatalysts may be further improved to enhance the adsorption selectivity and the photocatalytic activity for PFAS. Additional treatment means should be explored to enhance the photodegradation of the pre-sorbed by manipulating the treatment chemistry and by addition of some strong oxidizing reagents and/or photosensitizers.
7) Further studies are warranted using persulfate as a low-cost stimulating reagent in the photocatalysis system, especially when low-cost thermal energy is available.

References

Academy, K. Signal characteristics - intensity.

Ahangaran, F., Hassanzadeh, A. and Nouri, S., 2013. Surface modification of Fe_3O_4@SiO_2 microsphere by silane coupling agent. International Nano Letters 3(1), 1-5.

Ahmad, Z., Gao, B., Mosa, A., Yu, H., Yin, X., Bashir, A., Ghoveisi, H. and Wang, S., 2018. Removal of Cu (II), Cd (II) and Pb (II) ions from aqueous solutions by biochars derived from potassium-rich biomass. Journal of Cleaner Production 180, 437-449.

Ahrens, L. and Bundschuh, M., 2014. Fate and effects of poly‐and perfluoroalkyl substances in the aquatic environment: A review. Environmental toxicology and chemistry 33(9), 1921-1929.

Anirudhan, T., Divya, L. and Ramachandran, M., 2008. Mercury (II) removal from aqueous solutions and wastewaters using a novel cation exchanger derived from coconut coir pith and its recovery. Journal of Hazardous materials 157(2-3), 620-627.

ATSDR, 2008 Cadmium Toxicity.

ATSDR, 2012 Toxicological Profile for Cadmium.

Axe, L. and Anderson, P.R., 1995. Sr diffusion and reaction within Fe oxides: Evaluation of the rate-limiting mechanism for sorption. Journal of Colloid and Interface Science 175(1), 157-165.

Ayala, J., Blanco, F., Garcìa, P., Rodriguez, P. and Sancho, J., 1998. Asturian fly ash as a heavy metals removal material. Fuel 77(11), 1147-1154.

Bailey, S.E., Olin, T.J., Bricka, R.M. and Adrian, D.D., 1999. A review of potentially low-cost sorbents for heavy metals. Water Research 33(11), 2469-2479.

Boyer, T.H. and Singer, P.C., 2008. Stoichiometry of removal of natural organic matter by ion exchange. Environmental science & technology 42(2), 608-613.

Brown, D.W., Floyd, A.J. and Sainsbury, M., 1988. Organic spectroscopy, John Wiley & Sons Inc.

Buck, R.C., Franklin, J., Berger, U., Conder, J.M., Cousins, I.T., de Voogt, P., Jensen, A.A., Kannan, K., Mabury, S.A. and van Leeuwen, S.P., 2011. Perfluoroalkyl and polyfluoroalkyl substances in the environment: terminology, classification, and origins. Integr Environ Assess Manag 7(4), 513-541.

Cambié, D., Bottecchia, C., Straathof, N.J., Hessel, V. and Noel, T., 2016. Applications of continuous-flow photochemistry in organic synthesis, material science, and water treatment. Chemical reviews 116(17), 10276-10341.

Cao, S., Chen, Y., Wang, C., Lv, X. and Fu, W., 2015. Spectacular photocatalytic hydrogen evolution using metal-phosphide/CdS hybrid catalysts under sunlight irradiation. Chemical Communications 51(41), 8708-8711.

Chen, H., Yao, Y., Zhao, Z., Wang, Y., Wang, Q., Ren, C., Wang, B., Sun, H., Alder, A.C., Kannan, K.J.E.s. and technology, 2018. Multimedia Distribution and Transfer of Per-and Polyfluoroalkyl Substances (PFASs) Surrounding Two Fluorochemical Manufacturing Facilities in Fuxin, China. 52(15), 8263-8271.

Chen, X., Xia, X., Wang, X., Qiao, J. and Chen, H., 2011. A comparative study on sorption of perfluorooctane sulfonate (PFOS) by chars, ash and carbon nanotubes. Chemosphere 83(10), 1313-1319.

Clarke, D.B., Bailey, V., Routledge, A., Lloyd, A., Hird, S., Mortimer, D., Gem, M.J.F.A. and Contaminants, 2010. Dietary intake estimate for perfluorooctanesulphonic acid (PFOS) and

other perfluorocompounds (PFCs) in UK retail foods following determination using standard addition LC–MS/MS. 27(4), 530-545.

Deng, S., Yu, Q., Huang, J. and Yu, G., 2010. Removal of perfluorooctane sulfonate from wastewater by anion exchange resins: effects of resin properties and solution chemistry. Water Research 44(18), 5188-5195.

Deng, S., Zhang, Q., Nie, Y., Wei, H., Wang, B., Huang, J., Yu, G. and Xing, B., 2012. Sorption mechanisms of perfluorinated compounds on carbon nanotubes. Environmental Pollution 168, 138-144.

Domingo, J.L.J.E.i., 2012. Health risks of dietary exposure to perfluorinated compounds. 40, 187-195.

Dong, D., Nelson, Y.M., Lion, L.W., Shuler, M.L. and Ghiorse, W.C., 2000. Adsorption of Pb and Cd onto metal oxides and organic material in natural surface coatings as determined by selective extractions: new evidence for the importance of Mn and Fe oxides. Water Research 34(2), 427-436.

Du, Z., Deng, S., Bei, Y., Huang, Q., Wang, B., Huang, J. and Yu, G., 2014. Adsorption behavior and mechanism of perfluorinated compounds on various adsorbents—a review. Journal of hazardous materials 274, 443-454.

Du, Z., Deng, S., Chen, Y., Wang, B., Huang, J., Wang, Y. and Yu, G., 2015. Removal of perfluorinated carboxylates from washing wastewater of perfluorooctanesulfonyl fluoride using activated carbons and resins. Journal of hazardous materials 286, 136-143.

Dudley, L.-A., 2012. Removal of Perfluorinated Compounds by Powdered Activated Carbon, Superfine Powder Activated Carbon, and Anion Exchange Resin.

EGLE, 2018 General PFAS Sampling Guidance.

Emeje, M. and Blumenberg, M., 2020. Chemical Properties of Starch, BoD–Books on Demand.

EPA, 2009a Hazardous Waste Characteristics.

EPA, 2009b National Primary Drinking Water Regulations.

EPA, 2017 Drinking Water Health Advisories for PFOA and PFOS.

EPA, 2021 IRIS Toxicological Review of Perfluorobutanoic Acid (PFBA) and Related Salts.

Espana, V.A.A., Mallavarapu, M. and Naidu, R., 2015. Treatment technologies for aqueous perfluorooctanesulfonate (PFOS) and perfluorooctanoate (PFOA): A critical review with an emphasis on field testing. Environmental Technology & Innovation 4, 168-181.

Franke, V., McCleaf, P., Lindegren, K. and Ahrens, L., 2019. Efficient removal of per-and polyfluoroalkyl substances (PFASs) in drinking water treatment: nanofiltration combined with active carbon or anion exchange. Environmental Science: Water Research & Technology 5(11), 1836-1843.

Fu, J., Wang, L., Chen, H., Bo, L., Zhou, C. and Chen, J., 2010. A selective fluorescence probe for mercury ion based on the fluorescence quenching of terbium (III)-doped cadmium sulfide composite nanoparticles. Spectrochimica Acta Part A: Molecular and Biomolecular Spectroscopy 77(3), 625-629.

Ghasemi, E., Heydari, A. and Sillanpää, M., 2017. Superparamagnetic Fe_3O_4@ EDTA nanoparticles as an efficient adsorbent for simultaneous removal of Ag (I), Hg (II), Mn (II), Zn (II), Pb (II) and Cd (II) from water and soil environmental samples. Microchemical Journal 131, 51-56.

Ghisi, R., Vamerali, T. and Manzetti, S., 2019. Accumulation of perfluorinated alkyl substances (PFAS) in agricultural plants: a review. Environmental research 169, 326-341.

Gong, Y., Liu, Y., Xiong, Z., Kaback, D. and Zhao, D., 2012. Immobilization of mercury in field soil and sediment using carboxymethyl cellulose stabilized iron sulfide nanoparticles. Nanotechnology 23(29), 294007.

Gong, Y., Liu, Y., Xiong, Z. and Zhao, D., 2014. Immobilization of mercury by carboxymethyl cellulose stabilized iron sulfide nanoparticles: reaction mechanisms and effects of stabilizer and water chemistry. Environmental Science and Technology 48(7), 3986-3994.

Gong, Y., Wang, L., Liu, J., Tang, J. and Zhao, D., 2016. Removal of aqueous perfluorooctanoic acid (PFOA) using starch-stabilized magnetite nanoparticles. Science of the Total Environment 562, 191-200.

Gonzalez, D., Thompson, K., Quiñones, O., Dickenson, E. and Bott, C., 2020. Assessment of PFAS fate, transport, and treatment inhibition associated with a simulated AFFF release within a WASTEWATER treatment plant. Chemosphere 262, 127900.

Goss, K.-U., 2008. The pK_a values of PFOA and other highly fluorinated carboxylic acids. Environmental science & technology 42(2), 456-458.

Granados-Correa, F., Corral-Capulin, N., Olguín, M. and Acosta-León, C., 2011. Comparison of the Cd (II) adsorption processes between boehmite (γ-AlOOH) and goethite (α-FeOOH). Chemical Engineering Journal 171(3), 1027-1034.

Gu, B., Ku, Y.-K. and Brown, G.M., 2005. Sorption and desorption of perchlorate and U (VI) by strong-base anion-exchange resins. Environmental science & technology 39(3), 901-907.

Gulkaya, I., Surucu, G.A. and Dilek, F.B., 2006. Importance of H_2O_2/Fe^{2+} ratio in Fenton's treatment of a carpet dyeing wastewater. Journal of hazardous materials 136(3), 763-769.

He, F. and Zhao, D., 2007. Manipulating the size and dispersibility of zerovalent iron nanoparticles by use of carboxymethyl cellulose stabilizers. Environmental Science and Technology 41(17), 6216-6221.

He, F. and Zhao, D., 2008. Hydrodechlorination of trichloroethene using stabilized Fe-Pd nanoparticles: Reaction mechanism and effects of stabilizers, catalysts and reaction conditions. Applied Catalysis B: Environmental 84(3-4), 533-540.

He, F., Zhao, D., Liu, J. and Roberts, C.B., 2007. Stabilization of Fe−Pd Nanoparticles with Sodium Carboxymethyl Cellulose for Enhanced Transport and Dechlorination of Trichloroethylene in Soil and Groundwater. Industrial and Engineering Chemistry Research 46(1), 29-34.

Hilles, A.H., Amr, S.S.A., Hussein, R.A., El-Sebaie, O.D. and Arafa, A.I., 2016. Performance of combined sodium persulfate/H_2O_2 based advanced oxidation process in stabilized landfill leachate treatment. Journal of Environmental Management 166, 493-498.

Hori, H., Yamamoto, A., Hayakawa, E., Taniyasu, S., Yamashita, N., Kutsuna, S., Kiatagawa, H., Arakawa, R.J.E.S. and Technology, 2005. Efficient decomposition of environmentally persistent perfluorocarboxylic acids by use of persulfate as a photochemical oxidant. 39(7), 2383-2388.

Hu, X.C., Andrews, D.Q., Lindstrom, A.B., Bruton, T.A., Schaider, L.A., Grandjean, P., Lohmann, R., Carignan, C.C., Blum, A. and Balan, S.A., 2016. Detection of poly-and perfluoroalkyl substances (PFASs) in US drinking water linked to industrial sites, military fire training areas, and wastewater treatment plants. Environmental science & technology letters 3(10), 344-350.

Ito, D., Miura, K., Ichimura, T., Ihara, I. and Watanabe, T., 2004. Removal of As, Cd, Hg and Pb ions from solution by adsorption with bacterially-produced magnetic iron sulfide particles

using high gradient magnetic separation. IEEE Transactions on applied superconductivity 14(2), 1551-1553.

Jain, M., Yadav, M., Kohout, T., Lahtinen, M., Garg, V.K. and Sillanpää, M., 2018. Development of iron oxide/activated carbon nanoparticle composite for the removal of Cr (VI), Cu (II) and Cd (II) ions from aqueous solution. Water Resources and Industry 20, 54-74.

Jian, J.M., Chen, D., Han, F.J., Guo, Y., Zeng, L.X., Lu, X.W. and Wang, F., 2018. A short review on human exposure to and tissue distribution of per- and polyfluoroalkyl substances (PFASs). Science of the Total Environment 636, 1058-1069.

Kadirvelu, K. and Namasivayam, C., 2003. Activated carbon from coconut coirpith as metal adsorbent: adsorption of Cd (II) from aqueous solution. Advances in Environmental Research 7(2), 471-478.

Karim, M.R., Aijaz, M.O., Alharth, N.H., Alharbi, H.F., Al-Mubaddel, F.S. and Awual, M.R., 2019. Composite nanofibers membranes of poly (vinyl alcohol)/chitosan for selective lead (II) and cadmium (II) ions removal from wastewater. Ecotoxicology and environmental safety 169, 479-486.

Kecskes, L.J., Trevino, S.F., Klotz, B.R. and Gersten, B.L., 2003. Characterization of a nanosized iron powder by comparative methods. KONA Powder and Particle Journal 21, 143-150.

Khan, M.A., Khan, S., Khan, A. and Alam, M., 2017. Soil contamination with cadmium, consequences and remediation using organic amendments. Science of the Total Environment 601, 1591-1605.

Klik, B., Kulikowska, D., Gusiatin, Z.M. and Pasieczna-Patkowska, S., 2020. Washing agents from sewage sludge: Efficiency of Cd removal from highly contaminated soils and effect on soil organic balance. Journal of Soils and Sediments 20(1), 284-296.

Kramers, H.A., 1940. Brownian motion in a field of force and the diffusion model of chemical reactions. Physica 7(4), 284-304.

Kurniawan, T.A. and Lo, W.-h., 2009. Removal of refractory compounds from stabilized landfill leachate using an integrated H_2O_2 oxidation and granular activated carbon (GAC) adsorption treatment. Water Research 43(16), 4079-4091.

Land, M., De Wit, C.A., Bignert, A., Cousins, I.T., Herzke, D., Johansson, J.H. and Martin, J.W., 2018. What is the effect of phasing out long-chain per-and polyfluoroalkyl substances on the concentrations of perfluoroalkyl acids and their precursors in the environment? A systematic review. Environmental Evidence 7(1), 1-32.

Li, F., Duan, J., Tian, S., Ji, H., Zhu, Y., Wei, Z. and Zhao, D., 2020a. Short-chain per-and polyfluoroalkyl substances in aquatic systems: Occurrence, impacts and treatment. Chemical Engineering Journal 380, 122506.

Li, F., Wei, Z., He, K., Blaney, L., Cheng, X., Xu, T., Liu, W. and Zhao, D., 2020b. A concentrate-and-destroy technique for degradation of perfluorooctanoic acid in water using a new adsorptive photocatalyst. Water Research 185, 116219.

Li, P. and Sengupta, A.K., 2000. Intraparticle diffusion during selective sorption of trace contaminants: the effect of gel versus macroporous morphology. Environmental science & technology 34(24), 5193-5200.

Li, Y., Ding, J., Luan, Z., Di, Z., Zhu, Y., Xu, C., Wu, D. and Wei, B., 2003. Competitive adsorption of Pb^{2+}, Cu^{2+} and Cd^{2+} ions from aqueous solutions by multiwalled carbon nanotubes. Carbon 41(14), 2787-2792.

Li, Z., Zhang, P., Shao, T., Wang, J., Jin, L. and Li, X., 2013. Different nanostructured In_2O_3 for photocatalytic decomposition of perfluorooctanoic acid (PFOA). Journal of hazardous materials 260, 40-46.

Liu, J., Valsaraj, K.T., Devai, I. and DeLaune, R., 2008. Immobilization of aqueous Hg (II) by mackinawite (FeS). Journal of Hazardous materials 157(2-3), 432-440.

Liu, R. and Zhao, D., 2007a. *In situ* immobilization of Cu (II) in soils using a new class of iron phosphate nanoparticles. Chemosphere 68(10), 1867-1876.

Liu, R. and Zhao, D., 2007b. Reducing leachability and bioaccessibility of lead in soils using a new class of stabilized iron phosphate nanoparticles. Water Research 41(12), 2491-2502.

Liu, W., Cai, Z., Zhao, X., Wang, T., Li, F. and Zhao, D., 2016. High-capacity and photoregenerable composite material for efficient adsorption and degradation of phenanthrene in water. Environmental science & technology 50(20), 11174-11183.

Liu, Y., Xiao, T., Ning, Z., Li, H., Tang, J. and Zhou, G., 2013. High cadmium concentration in soil in the Three Gorges region: Geogenic source and potential bioavailability. Applied geochemistry 37, 149-156.

Mahmood-ul-Hassan, M., Suthor, V., Rafique, E. and Yasin, M., 2015. Removal of Cd, Cr, and Pb from aqueous solution by unmodified and modified agricultural wastes. Environmental monitoring and assessment 187(2), 19.

Maimaiti, A., Deng, S., Meng, P., Wang, W., Wang, B., Huang, J., Wang, Y. and Yu, G., 2018. Competitive adsorption of perfluoroalkyl substances on anion exchange resins in simulated AFFF-impacted groundwater. Chemical Engineering Journal 348, 494-502.

Maity, D. and Agrawal, D., 2007. Synthesis of iron oxide nanoparticles under oxidizing environment and their stabilization in aqueous and non-aqueous media. Journal of Magnetism and Magnetic Materials 308(1), 46-55.

Mindat Vivianite.

Mohamadiun, M., Dahrazma, B., Saghravani, S.F. and Darban, A.K., 2018. Removal of cadmium from contaminated soil using iron (III) oxide nanoparticles stabilized with polyacrylic acid. Journal of Environmental Engineering and Landscape Management 26(2), 98-106.

Moussout, H., Ahlafi, H., Aazza, M. and Maghat, H., 2018. Critical of linear and nonlinear equations of pseudo-first order and pseudo-second order kinetic models. Karbala International Journal of Modern Science 4(2), 244-254.

MWRA, 2019 Statewide Study on Landfill Leachate PFOA and PFOS Impact on Water Resource Recovery Facility Influent.

Naushad, M., Ahamad, T., Al-Ghanim, K.A., Ala'a, H., Eldesoky, G.E. and Khan, A.A., 2019. A highly porous nanocomposite (Fe_3O_4@ BFR) for the removal of toxic Cd (II) ions from aqueous environment: Adsorption modelling and regeneration study. Composites Part B: Engineering 172, 179-185.

Naushad, M., Ahamad, T., Alothman, Z.A., Shar, M.A., AlHokbany, N.S. and Alshehri, S.M., 2015. Synthesis, characterization and application of curcumin formaldehyde resin for the removal of Cd^{2+} from wastewater: kinetics, isotherms and thermodynamic studies. Journal of Industrial and Engineering Chemistry 29, 78-86.

Özverdi, A. and Erdem, M., 2006. Cu^{2+}, Cd^{2+} and Pb^{2+} adsorption from aqueous solutions by pyrite and synthetic iron sulphide. Journal of Hazardous materials 137(1), 626-632.

Pan, B., Zhang, Q., Du, W., Zhang, W., Pan, B., Zhang, Q., Xu, Z. and Zhang, Q., 2007. Selective heavy metals removal from waters by amorphous zirconium phosphate: Behavior and mechanism. Water Research 41(14), 3103-3111.

Pereira, H.C., Ullberg, M., Kleja, D.B., Gustafsson, J.P. and Ahrens, L.J.C., 2018. Sorption of perfluoroalkyl substances (PFASs) to an organic soil horizon–Effect of cation composition and pH. 207, 183-191.

Qiao, Y., Wu, J., Xu, Y., Fang, Z., Zheng, L., Cheng, W., Tsang, E.P., Fang, J. and Zhao, D., 2017. Remediation of cadmium in soil by biochar-supported iron phosphate nanoparticles. Ecological Engineering 106, 515-522.

Radha, A., Forbes, T.Z., Killian, C.E., Gilbert, P. and Navrotsky, A., 2010. Transformation and crystallization energetics of synthetic and biogenic amorphous calcium carbonate. Proceedings of the National Academy of Sciences.

Rahman, M.F., Peldszus, S. and Anderson, W.B., 2014. Behaviour and fate of perfluoroalkyl and polyfluoroalkyl substances (PFASs) in drinking water treatment: A review. Water research 50, 318-340.

Ross, I., McDonough, J., Miles, J., Storch, P., Thelakkat Kochunarayanan, P., Kalve, E., Hurst, J., S. Dasgupta, S. and Burdick, J.J.R.J., 2018. A review of emerging technologies for remediation of PFASs. 28(2), 101-126.

Sapsford, D., Barnes, A., Dey, M., Liang, L. and Williams, K., 2005. A novel method for passive treatment of mine water using a vertical flow accretion system. Proceedings 9th international mine water congressmine closure, 5-7.

Schneider, J., Matsuoka, M., Takeuchi, M., Zhang, J., Horiuchi, Y., Anpo, M. and Bahnemann, D.W., 2014. Understanding TiO_2 photocatalysis: mechanisms and materials. Chemical reviews 114(19), 9919-9986.

Senevirathna, S., Tanaka, S., Fujii, S., Kunacheva, C., Harada, H., Shivakoti, B.R. and Okamoto, R., 2010. A comparative study of adsorption of perfluorooctane sulfonate (PFOS) onto granular activated carbon, ion-exchange polymers and non-ion-exchange polymers. Chemosphere 80(6), 647-651.

Shi, F., Li, Y., Zhang, Q. and Wang, H., 2012. Synthesis of $Fe_3O_4/C/TiO_2$ magnetic photocatalyst via vapor phase hydrolysis. International Journal of Photoenergy 2012.

Singh, R.K., Fernando, S., Baygi, S.F., Multari, N., Thagard, S.M. and Holsen, T.M., 2019. Breakdown products from perfluorinated alkyl substances (PFAS) degradation in a plasma-based water treatment process. Environmental science & technology 53(5), 2731-2738.

Song, C., Chen, P., Wang, C. and Zhu, L., 2012. Photodegradation of perfluorooctanoic acid by synthesized TiO_2–MWCNT composites under 365 nm UV irradiation. Chemosphere 86(8), 853-859.

Su, Y., Adeleye, A.S., Keller, A.A., Huang, Y., Dai, C., Zhou, X. and Zhang, Y., 2015. Magnetic sulfide-modified nanoscale zerovalent iron (S-nZVI) for dissolved metal ion removal. Water Research 74, 47-57.

Sylvestre, J.P., Kabashin, A.V., Sacher, E., Meunier, M. and Luong, J.H., 2004. Stabilization and size control of gold nanoparticles during laser ablation in aqueous cyclodextrins. Journal of the American Chemical Society 126(23), 7176-7177.

Tan, Y. and Kilduff, J.E., 2007. Factors affecting selectivity during dissolved organic matter removal by anion-exchange resins. Water Research 41(18), 4211-4221.

Tian, S., Gong, Y., Ji, H., Duan, J. and Zhao, D., 2020. Efficient removal and long-term sequestration of cadmium from aqueous solution using ferrous sulfide nanoparticles: Performance, mechanisms, and long-term stability. Science of the Total Environment 704, 135402.

Tian, S., Xu, T., Fang, L., Zhu, Y., Li, F., Leary III, R.N., Zhang, M., Zhao, D., Soong, T.-Y. and Shi, H., 2021. A 'Concentrate-&-Destroy'technology for enhanced removal and destruction of per-and polyfluoroalkyl substances in municipal landfill leachate. Science of the Total Environment 791, 148124.

Vecitis, C.D., Park, H., Cheng, J., Mader, B.T. and Hoffmann, M.R., 2008. Kinetics and mechanism of the sonolytic conversion of the aqueous perfluorinated surfactants, perfluorooctanoate (PFOA), and perfluorooctane sulfonate (PFOS) into inorganic products. The Journal of Physical Chemistry A 112(18), 4261-4270.

Vecitis, C.D., Park, Hyunwoong, Cheng, Jie, Mader, Brian T, Hoffmann, Michael R, 2009. Treatment technologies for aqueous perfluorooctanesulfonate (PFOS) and perfluorooctanoate (PFOA). Frontiers of Environmental Science & Engineering in China 3(2), 129-151.

Wan, J., Zeng, G., Huang, D., Hu, L., Xu, P., Huang, C., Deng, R., Xue, W., Lai, C. and Zhou, C., 2018. Rhamnolipid stabilized nano-chlorapatite: synthesis and enhancement effect on Pb-and Cd-immobilization in polluted sediment. Journal of hazardous materials 343, 332-339.

Wang, F., Smith, D.W. and El-Din, M.G., 2003. Application of advanced oxidation methods for landfill leachate treatment–A review. Journal of Environmental Engineering and Science 2(6), 413-427.

Wang, S., Yang, Q., Chen, F., Sun, J., Luo, K., Yao, F., Wang, X., Wang, D., Li, X. and Zeng, G., 2017. Photocatalytic degradation of perfluorooctanoic acid and perfluorooctane sulfonate in water: A critical review. Chemical Engineering Journal 328, 927-942.

Weatherly, L.M., Shane, H.L., Lukomska, E., Baur, R. and Anderson, S.E., 2021. Systemic toxicity induced by topical application of heptafluorobutyric acid (PFBA) in a murine model. Food and Chemical Toxicology 156, 112528.

Wei, Z., Xu, T. and Zhao, D., 2019. Treatment of per-and polyfluoroalkyl substances in landfill leachate: status, chemistry and prospects. Environmental Science: Water Research & Technology 5(11), 1814-1835.

Wolthers, M., Van der Gaast, S.J. and Rickard, D., 2003. The structure of disordered mackinawite. American Mineralogist 88(11-12), 2007-2015.

Woodard, S., Berry, J. and Newman, B., 2017. Ion exchange resin for PFAS removal and pilot test comparison to GAC. Remediation Journal 27(3), 19-27.

Wu, D., Wang, Y., Li, Y., Wei, Q., Hu, L., Yan, T., Feng, R., Yan, L. and Du, B., 2019. Phosphorylated chitosan/$CoFe_2O_4$ composite for the efficient removal of Pb (II) and Cd (II) from aqueous solution: adsorption performance and mechanism studies. Journal of Molecular Liquids 277, 181-188.

Xiao, F., Davidsavor, K.J., Park, S., Nakayama, M. and Phillips, B.R., 2012. Batch and column study: sorption of perfluorinated surfactants from water and cosolvent systems by Amberlite XAD resins. Journal of colloid and interface science 368(1), 505-511.

Xiong, Z., He, F., Zhao, D. and Barnett, M.O., 2009. Immobilization of mercury in sediment using stabilized iron sulfide nanoparticles. Water research 43(20), 5171-5179.

Xu, J., Liu, Z., Zhao, D., Gao, N. and Fu, X., 2020a. Enhanced adsorption of perfluorooctanoic acid (PFOA) from water by granular activated carbon supported magnetite nanoparticles. Science of the Total Environment 723, 137757.

Xu, T., Ji, H., Gu, Y., Tong, T., Xia, Y., Zhang, L. and Zhao, D., 2020b. Enhanced adsorption and photocatalytic degradation of perfluorooctanoic acid in water using iron (hydr) oxides/carbon sphere composite. Chemical Engineering Journal 388, 124230.

Xue, W., Huang, D., Zeng, G., Wan, J., Cheng, M., Zhang, C., Hu, C. and Li, J., 2018a. Performance and toxicity assessment of nanoscale zero valent iron particles in the remediation of contaminated soil: a review. Chemosphere 210, 1145-1156.

Xue, W., Huang, D., Zeng, G., Wan, J., Zhang, C., Xu, R., Cheng, M. and Deng, R., 2018b. Nanoscale zero-valent iron coated with rhamnolipid as an effective stabilizer for immobilization of Cd and Pb in river sediments. Journal of hazardous materials 341, 381-389.

Xue, W., Peng, Z., Huang, D., Zeng, G., Wan, J., Xu, R., Cheng, M., Zhang, C., Jiang, D. and Hu, Z., 2018c. Nanoremediation of cadmium contaminated river sediments: microbial response and organic carbon changes. Journal of hazardous materials 359, 290-299.

Yates III, L.M. and von Wandruszka, R., 1999. Functional group analysis of Suwannee River fulvic acid with reactive fluorescent probes. Fresenius' journal of analytical chemistry 364(8), 746-748.

Yu, Q., Kaewsarn, P., Ma, W., Matheickal, J.T. and Yin, P., 2001. Removal of Heavy Metal Ions from Wastewater by Using Biosorbents from Marine Algae—A Cost Effective New Technology. Chinese Journal of Chemical Engineering.

Yu, Q., Zhang, R., Deng, S., Huang, J. and Yu, G., 2009. Sorption of perfluorooctane sulfonate and perfluorooctanoate on activated carbons and resin: kinetic and isotherm study. Water Research 43(4), 1150-1158.

Zaggia, A., Conte, L., Falletti, L., Fant, M. and Chiorboli, A., 2016. Use of strong anion exchange resins for the removal of perfluoroalkylated substances from contaminated drinking water in batch and continuous pilot plants. Water research 91, 137-146.

Zazo, J.A., Pliego, G., Blasco, S., Casas, J.A. and Rodriguez, J.J., 2011. Intensification of the Fenton process by increasing the temperature. Industrial & Engineering Chemistry Research 50(2), 866-870.

Zhang, C., Hopkins, Z.R., McCord, J., Strynar, M.J. and Knappe, D.R., 2019. Fate of per-and polyfluoroalkyl ether acids in the total oxidizable precursor assay and implications for the analysis of impacted water. Environmental science & technology letters 6(11), 662-668.

Zhang, C., Jiang, S., Tang, J., Zhang, Y., Cui, Y., Su, C., Qu, Y., Wei, L., Cao, H. and Quan, J., 2018. Adsorptive performance of coal based magnetic activated carbon for perfluorinated compounds from treated landfill leachate effluents. Process Safety and Environmental Protection 117, 383-389.

Zhang, X., Liu, H., Yang, J., Zhang, L., Cao, B., Liu, L. and Gong, W., 2021a. Removal of cadmium and lead from aqueous solutions using iron phosphate-modified pollen microspheres as adsorbents. Reviews on Advanced Materials Science 60(1), 365-376.

Zhang, Y., Zhang, Y., Akakuru, O.U., Xu, X. and Wu, A., 2021b. Research progress and mechanism of nanomaterials-mediated in-situ remediation of cadmium-contaminated soil: A critical review. Journal of Environmental Sciences 104, 351-364.

Zhao, D., 2019 Cost-effective destruction of per- and polyfluoroalkyl substances from DoD subsurface investigation-derived wastes using a new class of adsorptive photocatalysts, SERDP SEED Project ER18-1515.

Zhao, D. and Sengupta, A.K., 1998. Ultimate removal of phosphate from wastewater using a new class of polymeric ion exchangers. Water Research 32(5), 1613-1625.

Zhao, J., Niu, Y., Ren, B., Chen, H., Zhang, S., Jin, J. and Zhang, Y., 2018a. Synthesis of Schiff base functionalized superparamagnetic Fe3O4 composites for effective removal of Pb (II) and Cd (II) from aqueous solution. Chemical Engineering Journal 347, 574-584.

Zhao, X., Du, P., Cai, Z., Wang, T., Fu, J. and Liu, W., 2018b. Photocatalysis of bisphenol A by an easy-settling titania/titanate composite: Effects of water chemistry factors, degradation pathway and theoretical calculation. Environmental Pollution 232, 580-590.

Zhou, Z., Liang, Y., Shi, Y., Xu, L. and Cai, Y., 2013. Occurrence and transport of perfluoroalkyl acids (PFAAs), including short-chain PFAAs in Tangxun Lake, China. Environmental science & technology 47(16), 9249-9257.